Experimental study of novel control strategies for a 10 MW TetraSub floating wind turbine

Department of Wind Energy Master Report

Alex Gandia Santaya

DTU Wind Energy-M-0476

June 2021

DTU Wind Energy
Department of Wind Energy

Author: Alex Gandia Santay

Title: Experimental study of novel control strategies for a 10 MW TetraSub floating wind turbine

DTU Wind Energy-M-0476
June 2021

Project period:
January – June 2021

ECTS: 30

Education: Master of Science

Supervisor:

Antonio Pegalajar-Jurado
Henrik Bredmose
DTU Wind Energy

Remarks:
This report is submitted as partial fulfillment of the requirements for graduation in the above education at the Technical University of Denmark.

DTU Wind Energy is a department of the Technical University of Denmark with a unique integration of research, education, innovation and public/private sector consulting in the field of wind energy. Our activities develop new opportunities and technology for the global and Danish exploitation of wind energy. Research focuses on key technical-scientific fields, which are central for the development, innovation and use of wind energy and provides the basis for advanced education at the education.

Technical University of Denmark
Department of Wind Energy
Frederiksborgvej 399
4000 Roskilde
Denmark
www.vindenergi.dtu.dk

Abstract

This Master's Thesis presents an experimental study of novel control strategies for floating wind turbines. When applying conventional control strategies to floating wind turbines these can experience pitch instability above rated wind speed due to negative aerodynamic damping introduced by the floater pitch motion. In order to avoid this pitch instability an additional tower-velocity loop was implemented into the Basic DTU Wind Energy Controller.

This new control strategy was tested in a measurement campaign at the wave basin of Danish Hydraulic Institute. A 1:60 scale model of the DTU 10 MW Reference Wind Turbine was mounted on a lab-scale model of the TetraSub concept foundation, a semi-submersible floater designed and provided by Stiesdal Offshore Technologies. The floating wind turbine model was exposed to a series of different environmental conditions, including regular waves, irregular waves, focused waves and combined wind and wave conditions. The motion of the floater in all six degrees of freedom, accelerations and shear forces at the tower-top, mooring line tensions and the wind turbine operational data were measured and recorded. Two different controller strategies were applied in the measurement campaign, a slow detuned baseline controller and a faster controller containing the additional tower-top velocity loop.

The recorded data was analyzed in detail in both the time and frequency domain. The wave-only test results showed a high pitch motion of the floater. A harmonic decomposition highlighted significant influence of higher-order wave effects on the floater motion. The controller tests proved that the additional tower-top velocity loop was able to stabilize a previously unstable controller, thus allowing the application of a faster controller into a floating offshore wind turbine without triggering the pitch instability. The step wind simulations showed less overshoot in the rotational speed for the new controller, highlighting the benefit of the faster tower-top velocity loop controller over the slow baseline controller. The analysis of wind and wave tests under normal operational conditions showed that the new controller was performing on a similar level as the slower baseline controller, although showing slightly higher oscillations. Possible reasons for the higher structural response under the new controller were discussed and steps for future work were presented.

Acknowledgements

This Master's Thesis was carried out at the Wind Energy department at the Danish Technical University of Denmark by Alex G. Santaya. The project was carried out from January 2021 to June 2021, including a test campaign involving DTU Wind Energy, Stiesdal A/S and The Danish Hydraulic Institute (DHI). First of all I would like to dedicate a special thank you to the Danish Innovation Fond for funding the project and thereby making this master thesis possible. Likewise, I would like to thank DTU Wind Energy for the opportunity to participate in this fascinating project. Furthermore, I would like to express my gratitude to DHI for the possibility of using their state-of-the-art test facilities, as well as their amazing canteen. Last but not least, I would like to express my thanks to Stiesdal A/S for having provided the TetraSub concept foundation model.

During the experimental campaign many people from DTU Wind Energy, DHI and Stiesdal were involved. Without their continuous help and guidance the project would have never been possible. A big thanks goes to the DTU team of the FloatStep research project which apart from me consisted of MSc. Gustav T. Bak, Associate Professor Antonio M. P. Jurado, Associate Professor Fabio Pierella, Senior Researcher Fanzhong Meng, Senior Researcher Alan W. H. Lio and Professor Henrik Bredmose. I would like to express a special thanks to Antonio for his continuous support and clear guidance throughout the entire measurement campaign, without his ingenuity in finding solutions to the countless problem I encountered on the way, this entire project would have been impossible. Also Robert F. Mikkelsen deserves my gratitude for having designed the 1:60 scale DTU 10MW Reference Wind Turbine. I also would like to thank hydraulic engineers Bjarne Jensen, Dennis A. Hansen and Søren L. Sørensen and technician Poul Hansen for their support. Another big thanks to Freddy J. Madsen for his help during the experimental setup as well as his tips bearing in mind his expertise on the subject. Finally, I would like to acknowledge Michael Borg for having been in charge of the floater and mooring line system design.

Lastly, special thanks goes to my family and friends for their continuous support and love.

Alex G. Santaya
DTU, Kongens Lyngby, June 2021

Table of Contents

List of Figures

List of Tables

Abbreviations

BEM	Blade Element Momentum
BFOWT	Bottom Fixed Offshore Wind Turbine
CaPex	Capital Expenditure
DAQ	Data Acquisition
DHI	Danish Hydraulic Institute
DoF	Degree of Freedom
EC	Environmental Condition
FOWT	Floating Offshore Wind Turbine
IIR	Infinite Impulse Response
LCoE	Levelized Cost Of Energy
ML	Mooring Line
MWL	Mean Water Level
OPEX	Operational Expenditure
PRVS	Pitch-Regulated Variable Speed
PSD	Power Spectral Density
RWT	Reference Wind Turbine
SOT	Stiesdal Offshore Technology
SWL	Still Water Level
TLP	Tension Leg Platform
TRL	Technology Readiness Level
TSR	Tip Speed Ratio
uBEM	unsteady Blade Element Momentum
WG	Wave Gauge

CHAPTER 1

Introduction

1.1 Motivation

The Paris Agreement was accorded in 2015 to address the challenge of climate change and its negative impact on many aspects of society. The main goal of the deal is to keep the global temperature rise this century well below 2 °C above pre-industrial levels and pursuing efforts to limit the temperature increase to 1.5 °C [1]. Achieving such an ambitious goal requires to reach net-zero CO_2 emissions, in all the sectors of the economy, by 2050 [2]. In order to meet this target, the share of renewable energy sources (wind, solar, wave, tidal, hydro, geothermal, biomass) in the global electricity generation needs to increase drastically. Among these renewable sources, wind energy, especially offshore wind energy, is one of the most promising. In 2020, Europe added 2.9 GW net offshore capacity, corresponding to 356 new offshore wind turbines connected to the grid despite the COVID-19 pandemic, and had a total installed capacity of 25 GW. The development of the annually installed capacity as well as the cumulative installed capacity can be seen in Figure 1.1.

The vast majority of today's offshore wind farms consist of bottom fixed offshore wind turbines (BFOWTs), therefore restricted to water depths around 50 metres. Thus it is not a surprise that currently five countries - the UK, Germany, Denmark, Belgium and the Netherlands- represent 99 % of the total European offshore wind installed capacity, since these countries are surrounded by shallow waters such as the North, the Irish or the Baltic Sea [3]. In other countries such as Japan, the United States, Spain and others, the limited availability of shallow waters, the lower onshore wind attractiveness compared to offshore wind projects and the social pressure to keep the turbines out of sight raises the need for offshore wind farms in deep waters to become a reality.

Floating offshore wind turbines (FOWTs) eliminate the depth constraint imposed by bottom fixed wind turbines and could therefore unlock enough potential to meet the world's total electricity demand 11 times over in 2040 [4, 5]. The further away from the shore, the better are the wind resources as well as the possibility of using larger areas to mitigate wake effects, and hence yielding higher capacity factors. For instance, the Hywind Scotland pilot wind park achieved an average capacity factor of 56% in the first two years of operation [6]. Besides, offshore wind turbines are getting more powerful (see for example the Haliade-X 14 MW [7] or the SG14-222 DD [8]), thus allowing to bring down the costs due to economies of scale. Likewise, visual and

noise impacts are of less importance far-from-shore. All in all, there is large potential for floating offshore wind, especially in Europe, but also in the US and Asia [9].

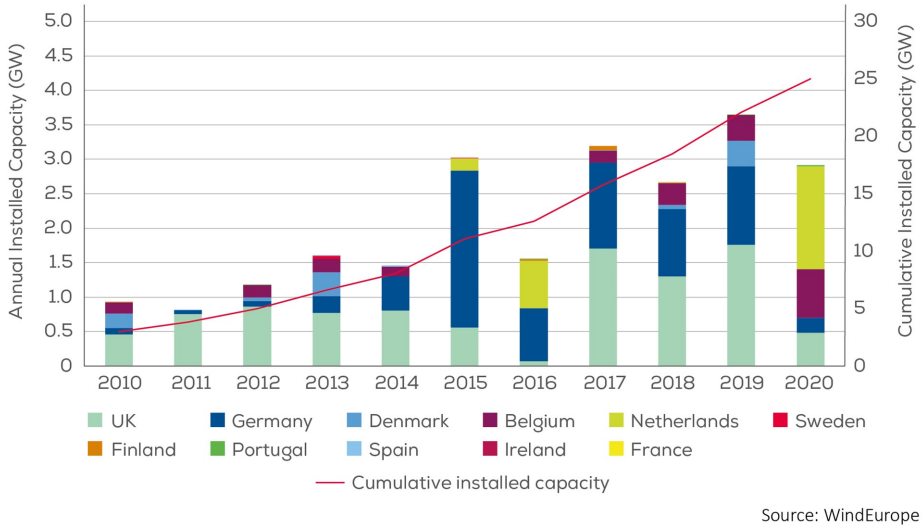

Figure 1.1: European annual offshore wind installations by country (left axis) and cumulative capacity (right axis) [3].

In recent years, there have been significant developments in pre-commercial and commercial-scale floating offshore wind projects such as Hywind Scotland (30 MW) [10] or Windfloat Atlantic Phase 1 (25.2 MW) [11]. However, even though the different floating offshore wind technologies have reached a high technology readiness level (TRL), their current levelized cost of energy (LCoE) can be 2 to 3 times higher than that of the BFOWTs [12]. At the same time, recent studies show that the LCoE of FOWTs could drop to 80-100 €/MWh by 2025, and further fall to 40-60 €/MWh by 2030, which is very close to the current LCoE of bottom-fixed offshore wind [13]. Floating offshore wind has significant opportunities of cost reduction in areas such as design optimization, assembly and installation, O&M and many other aspects.

A way of contributing to this cost reduction relies on effective wind turbine control systems, enabling higher energy production under harsh environments with better safety conditions. Furthermore, the Operational Expenditure (OPEX) can be reduced by health monitoring system resulting in fewer faulty events [14]. FOWT control systems are different from conventional control systems for BFOWT. Due to the motion of the floating substructure, the application of a conventional wind turbine controller in a FOWT can lead to severe dynamic instabilities. For the realization of a successful FOWT operation, the consideration of proper control technologies, specifically designed for the floating foundations, is imperative to achieve the best

performance and safety [15]. A well-functioning control system is also important to reduce the loads on the turbine and therefore reducing the costs of floating wind energy.

1.2 Project Outline

This Master's Thesis is part of the FloatStep research project, which is a joint project between DTU Wind Energy, Danish Hydraulic Institute (DHI), Siemens-Gamesa Renewable Energy, Stiesdal Offshore Technologies (SOT), Stromming IVS and University of Western Australia, mainly funded by the Danish Innovation Fund. The goal of the project is to develop methods and technologies for the optimisation of floating foundations and tower designs, improve current engineering tools and devise guidelines for de-risking the installation process. This involves numerical model developments, physical model tests and full-scale offshore testing [16].

As part of the FloatStep research project, a test campaign for the spring 2021 was conducted, in which novel control strategies for a 10 MW TetraSub floating wind turbine were tested. A lab-scale model of the TetraSub concept foundation connected to a 1:60 model of the DTU 10 MW Reference Wind Turbine (RWT) was tested at the test facilities of DHI. The purpose of the study is to investigate and test novel control strategies to avoid the well-known pitch instability experienced when applying conventional control strategies to floating wind turbines. The project included the preparation, planning and daily execution of the tests as well as the data analysis of the experiments.

The first section of this thesis provides a general introduction into FOWTs technology and the relevant theoretical background for dynamic load simulations of FOWTs. Afterwards, classical wind turbine control strategies, based on a PI pitch- and torque-controller, are explained. Furthermore, a novel control strategy for FOWTs is presented, which extends the classic PI-controller by an additional loop taking the tower velocity into account. After this theoretical introduction, the practical implementation of the new control strategy is discussed. The novel control strategy was implemented into the basic DTU Wind Energy controller [17] by Senior Researchers Fanzhong Meng and Alan W. H. Lio. In the next section of this thesis, the functionality of this new controller is validated on a numerical level by simulating a scaled version of the DTU 10 MW RWT in HAWC2 and comparing the performance of the basic DTU Wind Energy controller with and without the new tower velocity loop. In addition, some practical aspects of implementing the new control strategy into a physical model are discussed.

In the following section, the lab-scale physical model of the DTU 10 MW RWT and the TetraSub concept foundation are presented in detail. Then, the experimental setup at the DHI test facilities, the applied measurement equipment and the Data Acquisition (DAQ) system are presented. The execution of the test campaign itself is presented in the next chapter. First, the wind and wave conditions simulated at the test facilities are calibrated and compared to the target conditions. Afterwards,

the properties of the wind turbine and floater model are analyzed by carrying out a Rotor ID and decay tests. Finally, the procedure of tuning the parameters of two different controllers is presented. A conventional detuned controller was defined as the baseline controller and a faster controller, containing the new tower-top velocity loop, represented the novel FOWT controller.

In order to test the floater response and the performance of the different controllers, the combined floater-turbine model was exposed to a number of different environmental conditions including wave-only, wind-only and combined wind and wave conditions. The next section analyzes the results of these production tests in detail in both the time and frequency domain. First, the general floater response is studied by analyzing the wave-only and wind and wave tests using the detuned baseline controller. The last section presents a detailed comparison of the performance of the baseline controller and the new FOWT controller.

1.3 Related experimental work

Many industry players as well as academia are starting to turn their attention to floating wind energy. Therefore, several floater concepts have been tested, numerically and experimentally, to build a better understanding of the technology. The complex dynamics of a FOWT is determined by simultaneous wind and wave loads, which are modelled by coupling aeroelastic and hydrodynamic codes. For the purpose of validating these modelling tools, experimental tests play an important role. In this section, a summary of some major experiments conducted in recent years are presented.

In 2005, the Hywind concept was tested at Marintek, Norway, under simultaneous wind and wave conditions together with control strategies [18]. More recently, in 2012, the DeepCWind consortium lead by the University of Maine carried out model tests at MARIN, the Netherlands, with a 1:45 scale model of the NREL 5MW reference wind turbine mounted on several floaters: semi-submersible, tension leg platform (TLP) and spar concepts[19]. In 2015, results of tuned controllers for a spar-type FOWT were presented in a poster at EWEA Offshore 2015 [20]. Further work on control strategies for small-scale FOWTs took place in MARIN [21].

At DTU, a 1:200 scale model of the NREL 5MW RWT was tested in simultaneous wind and waves on a TLP floater in 2012 (Figure 1.2a). Initially downscaled to keep the output power at its maximum above rated conditions, the need of properly reproducing the small-scale thrust force was realized afterwards [22]. In 2015, a 1:60 scale model of the DTU 10MW RWT mounted on a TLP foundation (Figure 1.2b) was designed and tested under a large number of conditions with simultaneous exposure to wind and waves in the wave basin at DHI [23]. The rotor was redesigned to deliver the right Froude scale thrust at low Reynolds numbers [24], and operated at fixed speed and blade pitch. The tests were part of the INNWIND.EU project, and extended an earlier campaign for a semi-submersible configuration. In 2017, an experimental testing of a new 1:60 scale model TLP floater, mounted with the

DTU 10MW RWT (Figure 1.2c), was conducted to assess the performance of the model under different control configurations [25]. Also in 2017 the Triple Spar floater, which was a hybrid between a spar buoy and a semi submersible floater, was tested in the wave basin at DHI, with the 1:60 DTU 10 MW RWT attached to it [26]. In the TripleSpar campaign three different control strategies were investigated, an open-loop controller, a standard land-based controller and a slow detuned controller to avoid the pitch instability. The test campaign presented in this project builds on top of these previous campaigns, by testing both a new floater prototype and a novel control strategy specifically designed for floating wind turbines.

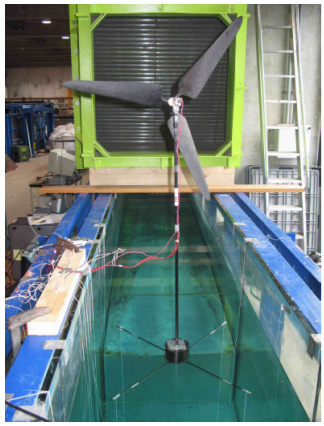

(a) The 1:200 TLP floating wind turbine model at DTU Wind Energy.

(b) The 1:60 TLP floating wind turbine model for the 2015 experimental campaign at DHI.

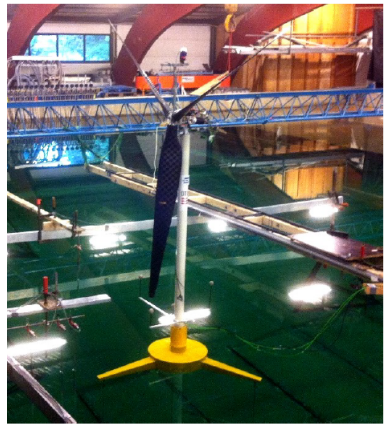

(c) The 1:60 TLP wind turbine model for the 2017 experimental campaign at DHI.

Figure 1.2: Lab-scale floating wind turbine models from previous experimental campaigns.

CHAPTER 2

Theoretical Background

In this chapter a summary of the current floating offshore wind technology situation is given together with its main variants. Then, a simplified way of modelling the structural response as well as the main loads (aerodynamic and hydrodynamic) and the mooring line systems are briefly explained. In addition, a brief introduction to control theory for wind turbines is given. First, the classical control strategy used in most conventional wind turbines is presented. Afterwards, an advanced control strategies, specifically designed for FOWTs, is presented.

2.1 Floating Offshore Wind Turbines

According to WindEurope, 80% of all the offshore wind resources in Europe are located in water depths deeper than 60 meters, where BFOWTs are not economically attractive [9]. Floating offshore wind energy can offer significant benefits for the wind industry in Europe:

- Higher capacity factors due to better wind resources far offshore.
- A lower audio-visual impact.
- Unlocking new renewable energy potential.
- The LCoE is less dependent on the location, as the mooring line system is less sensitive to the local soil conditions than bottom-fixed foundations.
- Higher flexibility in terms of O&M and decomissioning since the vast majority of the concepts can be assembled in the harbour and towed to the installation site.

However, it is important to highlight that FOWTs and BFOWTs are complementary, since the need of state-of-the-art designs and technological breakthroughs in the floating offshore wind industry will indeed bring the costs for BFOWTs down, and at the same time, as bottom-fixed is already an industrialized technology, floating

wind can also benefit from it in terms of research and technology development in its transition towards industrialization.

2.1.1 Types of floating substructures

A FOWT support structure is composed of the floater (for buoyancy and structural purposes), the mooring line and anchor systems (for station-keeping) and the dynamic power cable (for grid connection) [27]. In 2015, a total of 30 different floater support structures concepts had already been developed [28]. However, it is difficult to reach a high TRL for all of these developed technologies due to their diversity. While new concepts and technologies are coming up constantly, the existing designs can be divided into four main concepts (see Figure 2.2), reaching high TRLs [9]. Floating support structures can be classified according to the primary mechanism adopted to meet the static equilibrium requirements. There exist three main stabilising mechanisms:

- **Ballast stabilised**. Large floaters with a deep ballast at the bottom of the support structure leading to a centre of gravity position much lower compared to the centre of buoyancy, and hence creating a restoring pitch moment when the structure is tilted.

- **Waterplane stabilised**. The waterplane area is the main contributor to the restoring moment of the floater. Having a large second moment of area with respect to the rotational axis, either due to a large waterplane area or due to smaller cross-sectional areas at some distance from the system central axis, creates a restoring moment in case of rotational displacement. Furthermore, a shift in the center of buoyancy creates an additional restoring moment when the structure is tilted.

- **Mooring stabilised**. High tensioned mooring lines create the necessary restoring moment when the structure is tilted.

These three main stabilising mechanisms and its hybrid versions can be seen in Figure 2.1. Note how the three strategies make up the three cornerstones of floating support structures [29].

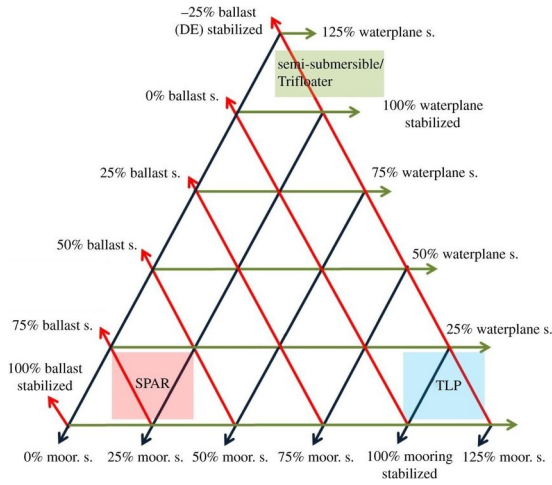

Figure 2.1: Stability triangle for floating structures. Figure taken from [29].

While there exist three types of stabilising mechanisms for FOWTs, the existing floater designs can be sorted into four main categories: spar, semi-submersible, barge and TLP concepts. Figure 2.2 shows an illustration of these four concepts.

- **Spar concepts**. The spar concept normally consists of a long cylindrical structure, ballasted at the bottom of the floater to obtain stability, and moored with three catenary lines, as can be seen in Figure 2.2. There could be other modifications to improve its performance, but this is the main trend.

  The most famous spar-buoyancy based commercial project is the Hywind Scotland off the coast of Scotland, which was the world's first floating offshore wind farm [10]. The next commercial project in the pipeline of the same developer is the Hywind Tampen project, which is an 88 MW floating wind power project intended to provide electricity to power offshore oil and gas platforms off the coast of Norway [30].

- **Semi-submersible concepts**. To obtain waterplane-based stability, this floater type is made out of usually three columns placed on the edges of a triangle. The wind turbine is either mounted on one of these columns or supported by a fourth one in the centre of the triangle. Braces interconnect the columns. In addition to the mooring line system attached to the geometric columns, heave plates can be added at the bottom of these columns in order to increase the natural period of the heave motion, resulting in reduced heave response at rated and extreme sea states [31].

  The WindFloat Atlantic Phase 1 project is an example of a semi-sub floater offshore wind farm, located off the coast of Portugal and commissioned in 2020 [11].

Examples of upcoming wind farms based on this concept are the Kincardine [32] or the EFGL [33] projects.

- **Barge concepts**. The barge concept is pretty similar to the semi-submersible concept since it is a waterplane stabilised technology. However, there are certain differences between these two technologies. While the semi-submersible has distributed buoyancy and consists of columns, the barge floater is typically flat without interspaces, allowing for the so-called damping pool. The sloshing of the water contained within the floater counteracts the movement of the floater caused by waves [34]. Operational projects such as the Floatgen project by the French Ideol [35] and other floating wind farms coming online in the following years such as EolMed [36] are examples of this technology.

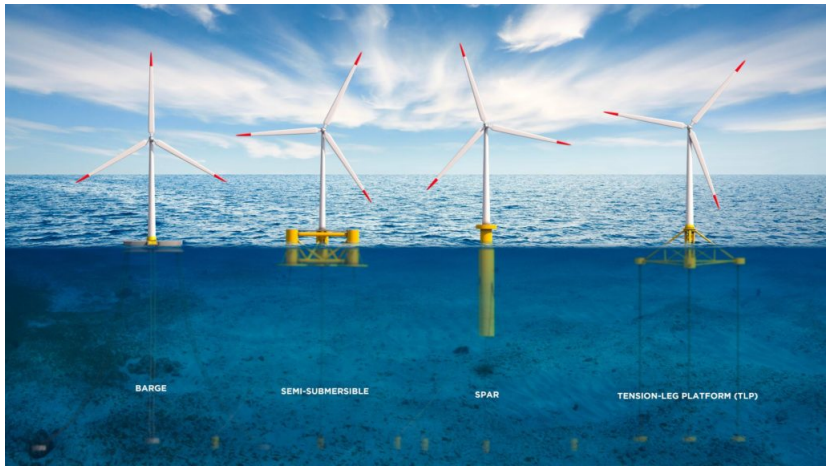

Figure 2.2: Four main types of FOWT support structures. Figure taken from [9].

- **TLP concepts**. The mooring stabilised tension-leg platform (TLP) concept has a central column to support the turbine. At the floater base three arms reach out where the tendons are connected. The displaced volume should be high enough to provide excess buoyancy to ensure that the mooring lines are always under tension. It is therefore heavily dependent on the chosen mooring line and anchoring system as well as the soil conditions. There exist some projects in the pipeline, specially in France, for instance Provence Grand Large or Eoliennes Flottantes de Groix.

- **Other concepts**. There exist hybrid concepts combining the different technologies in order to get the most out of each concept as seen in Figure 2.1. Another interesting idea is placing more than one turbine on top of a floater, thus bringing down the costs per turbine and increasing the stability. However, an appropriate design is needed in order to carry out such an idea in a feasible

way. Capturing not only the energy of the wind but also another energy source, such as wave, current, tidal, or solar energy is another potential way of increasing the power density. But, in the same way as in the multi-turbine floater, a thorough design is needed.

2.1.2 Maturity and challenges of Floating Wind

Europe's total floating offshore wind fleet stood at a total of 62 MW by the end of 2020, and over 7 GW are planned to be connected to the grid by the next decade [3], showing that the technology indeed has reached a commercialisation stage. As aforementioned, the four main types of floating substructures have already reached a TRL above 8 as can be seen in Figure 2.3.

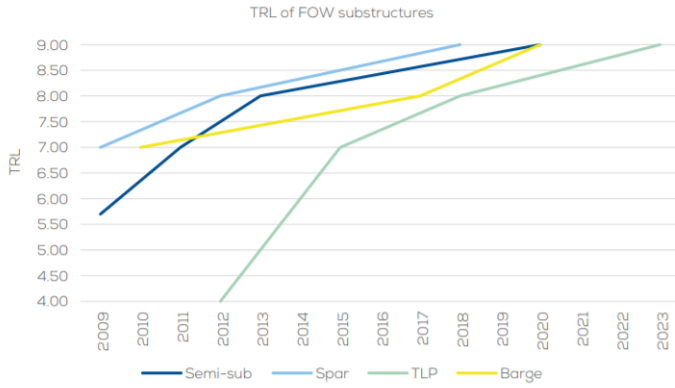

Figure 2.3: Technology Readiness Level of Floating Offshore Wind substructures. Figure taken from [9].

For those countries which cannot meet the energy demand by means of other renewable energy sources, floating wind energy represents an opportunity to cope with this deficit in an environmentally-friendly way. However, floating wind energy projects far from shore clearly lead to a higher Capital expenditure (CapEx) compared to fixed-bottom offshore wind energy projects (see Figure 2.4), and eventually leading to a higher LCoE. Consequently, governments should aim to integrate floating wind into its planning of energy infrastructure, adding financial security for floating wind projects, and industry and investors will thus be more likely to increase development commitments and investments.

Apart from the aforementioned economical and financial challenges, the deployment of floating wind energy projects also has some technical challenges. A list of the most important technical challenges of floating wind energy systems was given by the European Academy of Wind Energy (EAWE) in 2016 [38]. Some additional technical challenges are identified by the collaborative R&D initiative Floating Wind

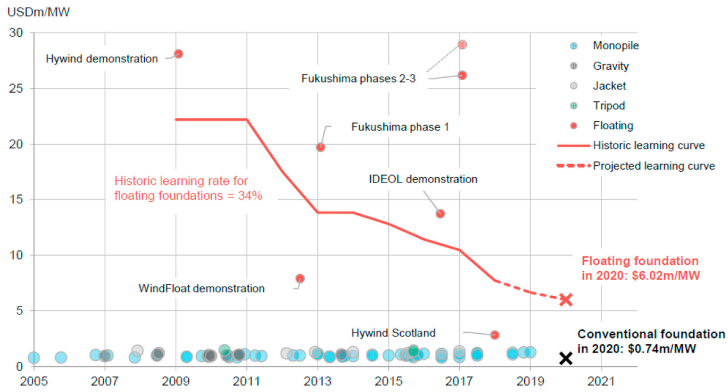

Figure 2.4: Cost comparison of fixed and floating foundation concepts. Figure taken from [37].

Joint Industry Project [39, 40]. These challenges involve some disciplines as electrical systems (dynamic power cables and floating substations), mooring systems (complex installation, designs for shallow water, reduction in fatigue), infrastructure and logistics (O&M and harbour strategies), turbine requirements (integrated design between floater designers and turbine suppliers) and monitoring (reducing mooring failure risk and inspection costs).

2.1.3 Structural Dynamics of Floating Wind Turbines

The structural dynamics of a FOWT differ from the dynamics of a BFOWT in the existence of the so-called rigid body modes. In these vibration modes, the entire turbine is moving as a rigid body, floating in the water. While other vibration modes exist for both floating and bottom-fixed turbines, the rigid body modes are unique to FOWTs. A careful analysis of the rigid body modes is crucial for the dynamic stability of a FOWT. Thus the rigid body dynamics will be explained in the following.

The FOWT is considered as one rigid body, with three translational and rotational degrees of freedom (DoFs). This is illustrated in Figure 2.5, together with the naming convention of the DoFs. The translational motion in the wind and wave direction is called Surge, the side-side motion Sway and the up-and-down motion is denoted as Heave. The rotational motions around the three axis are called Roll, Pitch and Yaw, respectively. These 6 DoFs are expressed in the 6x1 vector $\vec{\xi}$:

$$\vec{\xi} = \begin{bmatrix} \xi_1 \\ \xi_2 \\ \xi_3 \\ \xi_4 \\ \xi_5 \\ \xi_6 \end{bmatrix} = \begin{bmatrix} \text{Surge} \\ \text{Sway} \\ \text{Heave} \\ \text{Roll} \\ \text{Pitch} \\ \text{Yaw} \end{bmatrix} \tag{2.1}$$

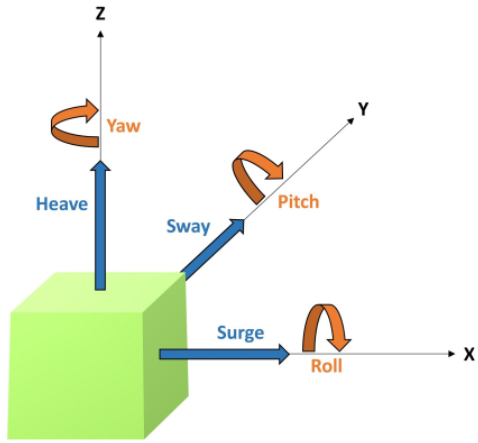

Figure 2.5: Motion of a floating turbine as a rigid body. Figure taken from [27].

A simple dynamic model, in the form of Newton's second law, to model the dynamic response of the FOWT is shown in Eq. 2.2. The external forces acting on the system can be summarised into four terms: the gravitational forces $\vec{F}_G$, the aerodynamic loads from the wind $\vec{F}_{Aero}$, the hydrodynamic loads from waves $\vec{F}_{Hydro}$ and the forces exerted by the mooring lines $\vec{F}_{Moor}$. All of these forces can be combined into a force vector, consisting of three translational forces and three moments.

$$(\mathbf{M} + \mathbf{A})\ddot{\vec{\xi}} + \mathbf{B}\dot{\vec{\xi}} + \mathbf{C}\vec{\xi} = \vec{F}_G + \vec{F}_{\text{Aero}} + \vec{F}_{\text{Hydro}} + \vec{F}_{\text{Moor}} \tag{2.2}$$

M is the mass matrix of the total system (floater and turbine). The added mass matrix **A** contains inertia terms derived from hydrodynamic load calculations. These inertial load terms represent forces due to the deceleration and acceleration of water around the body and are proportional to the acceleration of the floater itself. Therefore they can be transferred from the forcing right-hand-side of the equation to the system left-hand-side. **B** represents the damping matrix, which contains mainly hydrodynamic damping terms, which can be obtained by radiation-diffraction theory (see Appendix B). **C** is the restoring matrix, which contains hydrostatic forces.

Usually the mooring forces $\vec{F}_{Moor}$ are also added to the **C** matrix, as they are proportional to the displacement of the floater just like the hydrostatic forces. Depending on the stability mechanism used in the floater, different elements of the restoring **C** matrix are responsible for ensuring stability of the floater. All system matrices are 6x6 matrices and are often almost diagonal due to symmetry of the floater [41].

After obtaining the system matrices, the natural frequencies of the floater can be determined by carrying out an eigenvalue analysis. The knowledge of these frequencies is important to avoid resonance problems. Resonance issues can cause large oscillations and associated with that large fatigue loads, which deteriorate the lifetime of the turbine. The natural frequencies of a FOWT are usually significantly lower than the lowest natural frequencies of a bottom-fixed turbine, which is an important aspect to be taken into account in the design of a FOWT.

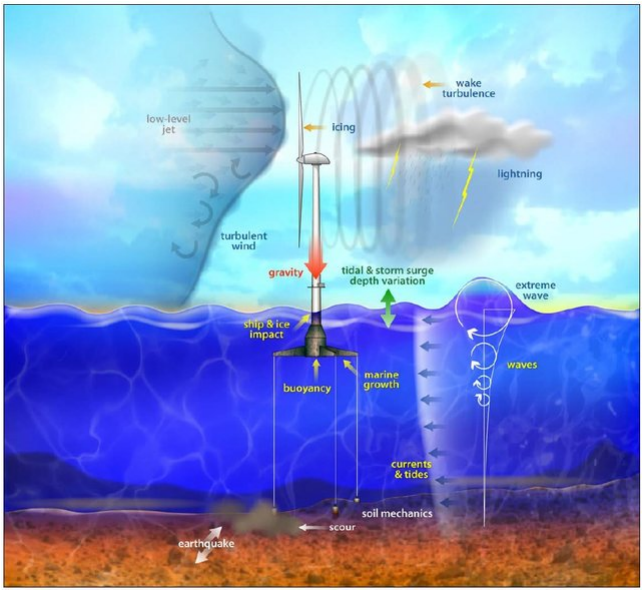

Figure 2.6: Loads on a floating offshore wind turbine. Figure taken from [42].

2.1.4 Loads on a floating wind turbine

FOWTs are mainly designed to be installed in deep waters far from shore under harsh environmental conditions. The dynamic response of a FOWT is governed by the environmental loads. The main loads acting on a FOWT are shown in Figure 2.6. The external loads are dominated by the aerodynamic and hydrodynamic loads. Other effects such as icing, earthquakes, lightnings or gravitational loads can also be modelled, if needed. FOWTs are large and flexible structures and the exciting load frequencies potentially match those of the structural frequencies, and hence aero-

hydro-elastic engineering models are needed for a proper dynamic design. The most important loads - aerodynamics, hydrodynamics, mooring system and its coupling with the structure - are presented below.

2.1.4.1 Aerodynamic loading

The classical Blade Element Momentum (BEM) method enables to calculate the steady-state aerodynamic loads as well as the thrust and power, given certain operational parameters (rotor speed, wind speed and blade pitch angle). The BEM method is used for computing a first estimation of a steady power curve, however the wind felt by a wind turbine rotor is unstable, stochastic and varying in time and space. It is therefore necessary to build a more sophisticated model, which can be achieved by means of the unsteady Blade Element Momentum (uBEM) method. By coupling the uBEM model with a structural model of the wind turbine, an aero-elastic code is developed, where the aerodynamic loads are based on the relative velocity seen by the blades, which is dependent on the structural velocity, which in turn is a consequence of the aerodynamic loading. This mutual interaction between aerodynamic, internal and inertia forces is denoted as aeroelasticity. There exist several industry-standard softwares for aeroelastic load simulations of wind turbines like HAWC2, FAST or Bladed. In this project HAWC2, developed and supported by DTU will be used.

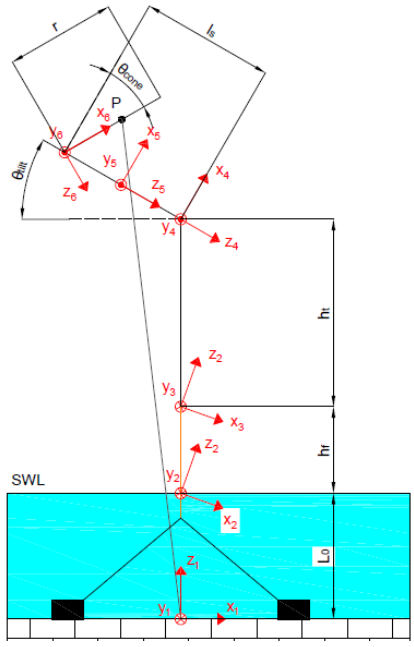

Figure 2.7: A floating wind turbine model described with six coordinate systems.

The uBEM method, commonly used in aeroelastic softwares, together with several coordinates systems to transform the different motions experienced by the system into an inertial coordinate system and vice versa, are presented in Appendix B. The coordinate system (Figure 2.7) definitions can be also found in the Appendix. Furthermore, the velocity triangle is explained, including the velocities resulting from the motion of the structure, becoming an iterative aeroelastic problem once these velocities are converted into aerodynamic forces. Empirical and engineering corrections for effects like dynamic wake, dynamic stall, tower shadow and wind shear, which increase the fidelity of the model, are also presented in Appendix B.

2.1.4.2 Hydrodynamic loading

Offshore wind turbines are not only exposed to aerodynamic forces but also to hydrodynamic forces. The inclusion of hydrodynamic effects extend aero-elastic models to aero-hydro-elastic simulations. Before hydrodynamic forces can be calculated, the wave kinematics must be obtained.

Wave kinematics

The most common method for modelling wave kinematics is Stokes 1^{st}-order wave theory, also called linear wave theory or Airy wave theory. This theory gives a linearized description of the propagation of gravity waves on the surface of a homogeneous fluid layer built on potential flow theory, and hence the flow is assumed to be incompressible, inviscid and irrotational. Furthermore, both the depth and the wave period are assumed to be constant. Because long and even wave crests are considered, the problem is described in two dimensions, as it is shown in Figure 2.8. Note that the theory is valid only for small wave heights H compared to their wavelength λ: $H/\lambda < 0.05$.

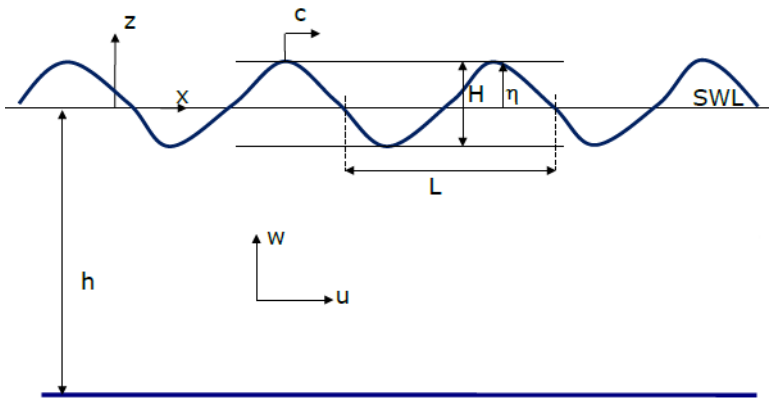

Figure 2.8: Parameters of linear wave theory for a progressive surface wave [43].

In the simplest form of linear wave theory a regular wave with constant period T and wavelength λ is considered. A regular wave is then described by its angular frequency ω and wave number k:

$$\omega = \frac{2\,\pi}{T} \tag{2.3}$$

$$k = \frac{2\,\pi}{\lambda} \tag{2.4}$$

The relationship between wave frequency and wave length is described by the so-called linear dispersion relation:

$$\omega^2 = gk\tanh(kh) \tag{2.5}$$

Based on the assumption of an incompressible, inviscid and irrotational flow, the following expressions can be obtained for the surface elevation η, the velocity potential ϕ, the horizontal particle velocity u and the vertical velocity w of a regular wave:

$$\eta(t,x) = \frac{H}{2}\cos(\omega t - kx) \tag{2.6}$$

$$\phi(t,x,z) = -\frac{\omega H}{2k}\frac{\cosh k(z+h)}{\sinh kh}\sin(\omega t - kx) \tag{2.7}$$

$$u(t,x,z) = \frac{\omega H}{2}\frac{\cosh k(z+h)}{\sinh kh}\cos(\omega t - kx) \tag{2.8}$$

$$w(t,x,z) = -\frac{\omega H}{2}\frac{\sinh k(z+h)}{\sinh kh}\sin(\omega t - kx) \tag{2.9}$$

where t denotes the time, x the horizontal and z the vertical coordinate. Appendix B shows the derivations of Eq. 2.5 - 2.9. It is important to remember that these expressions are only valid for small wave heights. For larger wave heights, the method of Wheeler stretching can be applied to "stretch" the velocity at the mean water level (MWL) $z = 0$ to the free surface elevation η.

Irregular Waves

A real sea state does not consist of only one regular wave with a single frequency, but of many different waves with different frequencies. Such an irregular sea state can be modeled by a superposition of regular waves. This approach is used to model time-series of irregular sea states and obtain more realistic representations of the wave kinematics. Irregular waves are defined as the sum of independent regular waves of different frequencies ω_j, amplitudes A_j, wave numbers k_j and random phases ϵ_j. A similar approach could be applied for the directionality of the waves, nevertheless, only unidirectional waves are considered in this project.

An irregular sea state can be analyzed by the use of a Fourier analysis. A Fourier analysis is based on the use of multiple frequencies contained in a particular signal.

Thus, it is possible to compute a wave spectrum, where the energy from the waves is distributed in a particular way among the frequencies. Similarly, a given irregular sea state can be analyzed in regards to its energy distribution across different frequencies. Some spectra are already defined by analytical expressions, and can easily be computed by defining the relevant parameters. A commonly used wave spectrum is the Pierson-Moskowitz spectrum, which is based on extensive field data in the North Atlantic Ocean and is usually used to describe fully developed sea states [44]. The spectrum depends on the significant wave height H_s and the peak period T_p (or peak frequency f_p) and is formulated as followed:

$$S_\eta(f) = \frac{5}{16}\frac{H_s^2 f_p^4}{f^5}\exp\left(-\frac{5}{4}\left(\frac{f_p}{f}\right)^{-4}\right) \tag{2.10}$$

An extension of the Pierson-Moskowitz spectrum is the JONSWAP (Joint North Sea Wave Project) spectrum, which is based on extensive measurements in the North Sea [44]. Its formulation is similar to the Pierson-Moskowitz spectrum, with the addition of a peak enhancement factor γ. Figure 2.9 shows an example of the Pierson-Moskowitz and the JONSWAP spectrum for $H_s = 3$ m, $T_p = 6$ s and $\gamma = 3.3$. For $\gamma = 1$ the JONSWAP spectrum converges to the Pierson-Moskowitz spectrum.

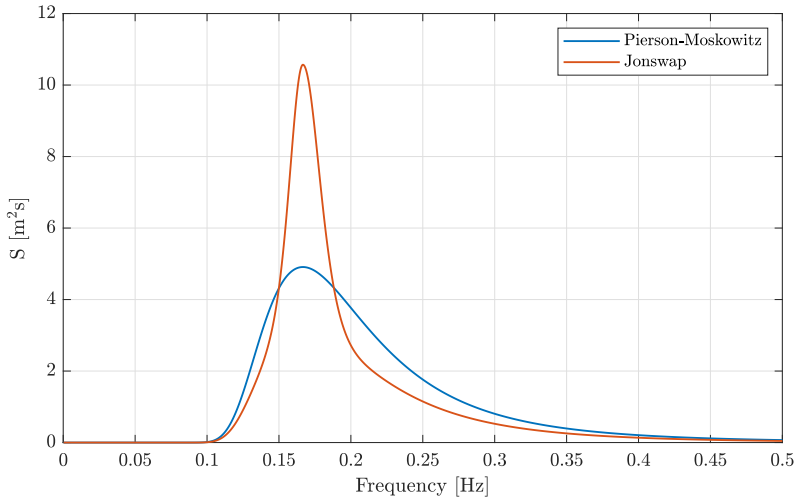

Figure 2.9: Pierson-Moskowitz and JONSWAP spectrum for $H_s = 3$ m, $T_p = 6$ s and $\gamma = 3.3$.

H_s is originally defined as the average height of the highest third of the waves, but is practically computed based on the standard deviation of the surface elevation σ_η:

$$H_s = 4\sigma_\eta = 4\sqrt{\sigma_\eta^2} \tag{2.11}$$

The variance σ_η^2 is equivalent to the area under the spectrum, or in other words, the total energy of the waves:

$$\sigma_\eta^2 = \int_0^\infty S_\eta(f)df = \sum_j S_\eta(f_j)\Delta f \tag{2.12}$$

Once the wave spectrum has been computed and properly rescaled, it is possible to get the Fourier coefficients or amplitudes, used to model the irregular waves, as followed:

$$A_j = \sqrt{2S_\eta\left(f_j\right)\Delta f} \tag{2.13}$$

Where the frequency step Δf is computed as the smallest possible frequency, i.e. the inverse of the simulation time. Then, to be able to compute the free surface elevation, the wave number k_j is computed for each discrete frequency, by solving the dispersion relation. Then, by using a superposition of the linear waves, the wave elevation of an irregular sea state can be computed as:

$$\eta(t,x) = \sum_{j=1}^{N} A_j \cos\left(\omega_j t - k_j x + \epsilon_j\right) \tag{2.14}$$

The velocity potential and particle velocities will likewise be a sum of the individual frequency components:

$$\phi(t,x,z) = \sum_{j=1}^{N} -A_j \frac{\omega_j}{k_j} \frac{\cosh k_j(z+h)}{\sinh k_j h} \sin\left(\omega_j t - k_j x + \epsilon_j\right) \tag{2.15}$$

$$u(t,x,z) = \sum_{j=1}^{N} A_j \omega_j \frac{\cosh k_j(z+h)}{\sinh k_j h} \cos\left(\omega_j t - k_j x + \epsilon_j\right) \tag{2.16}$$

$$w(t,x,z) = \sum_{j=1}^{N} -A_j \omega_j \frac{\sinh k_j(z+h)}{\sinh k_j h} \sin\left(\omega_j t - k_j x + \epsilon_j\right) \tag{2.17}$$

Focused Waves

A method for simulating extreme waves is the so called New Wave Theory. The idea is to adjust the phases between the regular linear waves in such a way that at a chosen time t_p they superimpose to an extreme wave, which is much higher than the neighbouring waves. Assuming a discrete wave spectrum $S_\eta(\omega_j)$ the time-series of such a focused wave with wave amplitude α can be expressed as followed [44]:

$$\eta(x,t) = \frac{\alpha}{\sigma_\eta^2} \sum_{j=1}^{N} S_\eta(f_j)\,\Delta f\,\cos\left(k_j\,x - \omega_j\,\tau\right) \tag{2.18}$$

$$\tau = t - t_p \tag{2.19}$$

Figure 2.10 shows an extreme wave with an amplitude $\alpha = 8$ m at $t_p = 300$ s created with the described model.

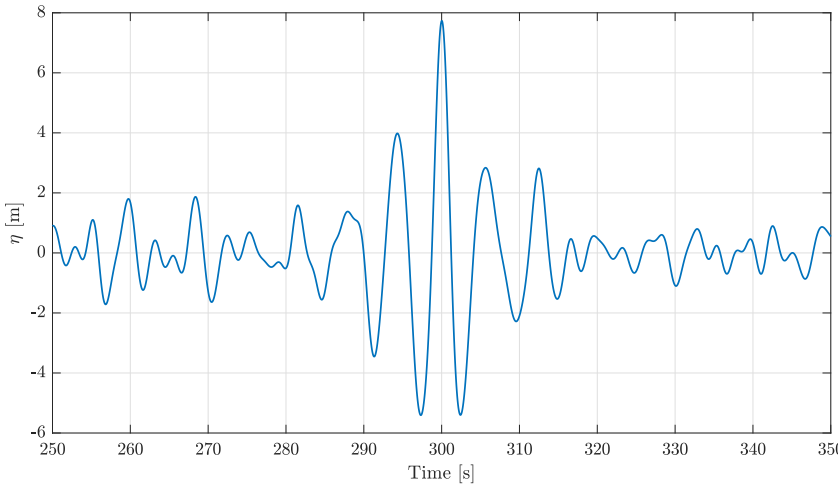

Figure 2.10: Focused wave created with New Wave Theory.

Hydrodynamic forces

Based on the wave kinematics, hydrodynamic forces are acting on offshore structures like floating wind turbines. There are several models of different fidelity for describing these external forces. One commonly used formula is the Morison equation, which can be used to compute the hydrodynamic forces acting on a slender submerged body like a monopile. It consists of contributions due to drag forces, which depend on the fluid velocity, and inertia forces, which depend on the acceleration. However, the Morison equation is only applicable for slender structures. For more complex geometries like most floating substructures, more advanced methods like radiation-diffraction theory must be applied. Linear radiation-diffraction theory divides the wave load calculation into two separate problems: a radiation and a diffraction problem. The radiation part refers to a body oscillating with a certain frequency ω in otherwise still water, hereby radiating waves. The diffraction part describes a fixed body being exposed to incoming waves with frequency ω. The total solution is then the sum of both individual parts. Both the Morison equation and the radiation-diffraction theory are described and discussed in more detail in Appendix B.

2.1.4.3 Mooring Dynamics

The main purpose of the mooring system for a floating wind turbine is station keeping, which is used to restrain the position of the structure as well as prevent large motions around the equilibrium point. In the simplest case, the mooring system can be modelled as a linear system, neglecting the dynamic effects, such as inertial and hydrodynamic loads. The force-displacement linear model can be written using Hooke's law:

$$\vec{F} = -\mathbf{C}\vec{\xi} \tag{2.20}$$

where $\vec{F}$ is a 6x1 vector of mooring forces and moments, $\mathbf{C}$ is the 6x6 mooring restoring matrix and $\vec{\xi}$ has been presented in Section 2.1.3. This linear approximation is more appropriate for taut mooring systems, where the restoring force is due to axial strain. However, for other mooring systems such as catenaries, the restoring force is related to the amount of line that rests on the seabed. In this case, the force-displacement presents a non-linear relationship that can be modelled by means of the inelastic catenary equations.

Even though quasi-static mooring equations (inelastic catenary equations) capture nonlinear restoring effects, some dynamic effects such as the inertial or hydrodynamic forces are not captured by these models. For a better reproduction of the reality, the dynamic effects can be included at the expense of a higher computational cost by means of a multibody or FEM approach [45].

Other components to bear in mind when designing an appropriate mooring system can be the type of anchor (dead weight, pile, suction anchor, etc) used to attach the system to the seabed, the possibility of adding a clump weight (reduce vertical forces on anchor and mooring line vibrations, add extra restoring force) or buoys (clearing seabed objects) [45].

2.2 Wind Turbine Control Theory

A well functioning control system is essential for the safe and stable operation of wind turbines. The control system contains many different components and serves several purposes like maximizing the power production, reducing the loads, keeping power and rotational speed within operational limits, enabling start-up and shutdown of the turbine, as well as providing safety systems like the ability for an emergency shutdown. The main elements of the control system are the pitch control, torque control and yaw control. The yaw system, which aligns the rotor with the incoming wind speed, is not the focus of this thesis and will therefore not be discussed further.

2.2.1 Classical wind turbine control strategies

In the past, wind turbines were often controlled by a passive stall-regulated system with constant rotational speed and no blade pitch. All modern state-of-the-art tur-

bines however use a pitch-regulated variable speed (PRVS) control system, which is the system presented hereafter. A wind turbine with a PRVS system can adjust both the rotational speed ω and the pitch angle θ. The pitch angle refers to a rotation of the blades around their longitudinal axes, which allows to adjust the angle of attack and therefore the aerodynamic forces. The blades can either be pitched collectively or each blade individually.

The control strategy is divided into several regions, with the two main regions being the partial load region below rated power and the full load region. Between these main regions, several transition regions exist. Figure 2.11 shows the different control regions of the DTU 10 MW RWT and the respective pitch angle, rotational speed and mechanical power as a function of the wind speed. The values are obtained by steady state calculations in HAWC2S and the basic DTU Wind Energy controller [17]. The partial load region is referred to as Region 1 and the full load region as Region 2. The exact details of the control strategies in the different regions can differ between turbines, but the main concept will be explained in the following by the example of Figure 2.11.

2.2.1.1 Partial Load Region

The objective of the partial load region is to maximize the power production and therefore the aerodynamic efficiency of the turbine. The efficiency of a wind turbine is described by the power coefficient C_P, which is defined as the ratio between the extracted power and the total available power of the wind:

$$C_P = \frac{P_{mech}}{\frac{1}{2}\,\rho\,A\,V_0^3} \tag{2.21}$$

where P_{mech} is the mechanical power, ρ the air density, A the rotor area and V_0 the free wind speed. It can be shown that the power coefficient of a wind turbine is in general a function of the tip speed ratio λ and the pitch angle θ [46]. The control objective of Region 1 is to ensure that the turbine is operating at those optimal conditions, this is also referred to as optimal C_P-tracking. The pitch angle is set to θ_{opt} (often 0°) and the rotational speed is adjusted, such that the turbine is operating at λ_{opt}. The rotational speed is regulated through the torque balance between the aerodynamic and the generator torque:

$$Q_{aero} - \frac{1}{\eta} Q_{gen} = I_{rotor}\,\frac{d\omega}{dt} \tag{2.22}$$

where I_{rotor} is the total inertia of the rotor and η is the generator efficiency. If $Q_{aero} > Q_{gen}$ then the rotor is accelerated and if $Q_{aero} < Q_{gen}$ it is decelerated. Thus, by controlling the generator torque the rotational speed of the turbine can be regulated. The necessary generator torque to maintain the torque equilibrium can be expressed as a quadratic function of the rotational speed [47]:

$$Q_{gen} = K\,\omega^2 \tag{2.23}$$

$$K = \frac{\eta\,\rho\,A\,R^3\,C_P(\theta_{opt}, \lambda_{opt})}{2\,n_g\,\lambda_{opt}^3} \tag{2.24}$$

where η is the generator efficiency, n_g the gearbox ratio and R the rotor radius. The derivation of expression 2.24 is shown in Appendix A.1.

Often a wind turbine has a minimum rotor speed ω_{min}, in order to prevent the 3P excitation getting in resonance with the first tower vibration mode. This is also the case for the DTU 10 MW RWT, as it can be seen in Figure 2.11 in the transition Region 0.5. At low wind speeds, the rotational speed is kept at ω_{min}, therefore λ_{opt} cannot be maintained for these wind speeds. The pitch angle for this region is calculated by a PI controller, before it reaches its optimal value in Region 1.

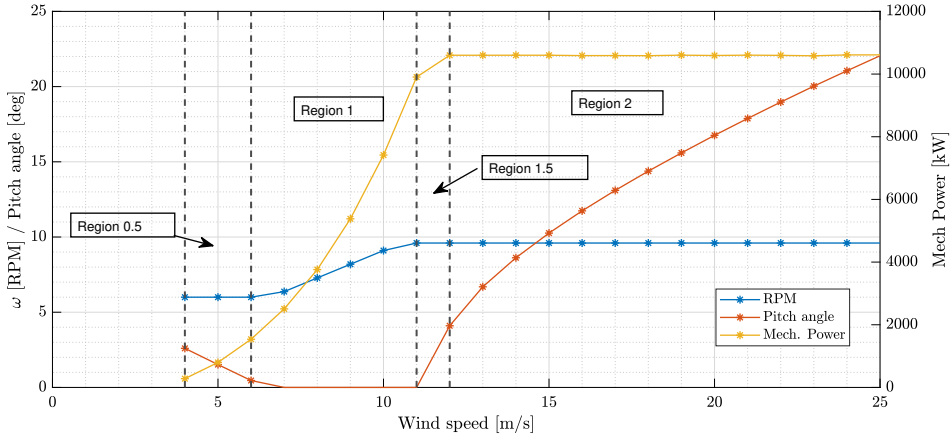

Figure 2.11: Control regions for the DTU 10 MW RWT with the DTU Wind Energy controller, calculated by HAWC2S.

Between Region 1 and 2 there is another transition region, denoted as Region 1.5. In this region, ω has reached its maximum value ω_{rated}, but rated power P_{rated} has not been reached yet. It should be noted that depending on the turbine, ω_{rated} can also be reached after P_{rated}. The control objective in Region 1.5 is to limit the rotational speed to ω_{rated}, while still increasing the power. This can be achieved by controlling the torque with a PI-controller and keeping θ constant or by controlling both torque and θ with a PI-controller [47]. The functionality of a PI-controller will be explained hereinafter.

2.2.1.2 Full Load Region

The control objective of the full load region is to limit both the power and the rotational speed to their rated values. This objective is achieved by controlling θ with a PI-controller. The basic idea of a PI controller is to adjust the output variable, in this case the pitch angle θ, based on the error between the input variable (the rotational speed ω) and a reference value (the rated rotational speed ω_{rated}). The change in pitch angle is calculated based on a term proportional to the error in ω and a term proportional to the integral of the error [47]:

$$\Delta\theta = k_P\,(\omega - \omega_{rated}) + k_I \int_0^t (\omega - \omega_{rated})\,dt \tag{2.25}$$

$$\Delta\theta = k_P\,\dot{\phi} + k_I\,\phi \tag{2.26}$$

Hereby k_P [rad/(rad/s)] and k_I [rad/rad] are the proportional and integral gains of the controller and ϕ is the angular displacement of the drivetrain. The change in θ is then given as an input to the wind turbine and the resulting new rotational speed is fed back as the new input to the controller. This kind of system is called a closed-loop controller. The equation of motion of this closed-loop system can be expressed in general terms as followed [47]:

$$I_{rotor}\,\ddot{\phi} = Q_{aero}(V,\omega,\theta) - \frac{1}{\eta}\,Q_{gen}(\omega) \tag{2.27}$$

Because the turbine is no longer operating at optimal C_P, the aerodynamic torque Q_{aero} is a non-linear function of wind speed V, rotational speed ω and the pitch angle θ. Therefore no explicit expression for the torque like in Eq. 2.24 can be derived. In general there exist two different variations of full load control strategy, constant torque and constant power. Depending on the strategy the generator torque is defined as followed [48]:

$$Q_{gen}(\omega) = \begin{cases} \frac{P_{rated}}{\omega_{rated}} & \text{for constant torque control} \\ \\ \frac{P_{rated}}{\omega} & \text{for constant power control} \end{cases} \tag{2.28}$$

In order to derive expressions for the gains k_P and k_I, the non-linear Eq. 2.27 is linearized around an operational point. By applying the derivations shown in Appendix A.2 the following simplified linear closed-loop equation for the drivetrain motion can be obtained [47]:

$$\underbrace{I_{rotor}}_{\text{"mass" m}}\ddot{\phi} + \underbrace{\left(\frac{1}{\eta}\frac{\partial Q_{gen}}{\partial\omega}\Big|_0 - \frac{\partial Q_{aero}}{\partial\omega}\Big|_0 - \frac{\partial Q_{aero}}{\partial\theta}\Big|_0 k_P\right)}_{\text{"damping" c}}\dot{\phi} - \underbrace{\frac{\partial Q_{aero}}{\partial\theta}\Big|_0 k_I}_{\text{"stiffness" k}}\phi = 0 \tag{2.29}$$

Hereby the shorthand notation $\frac{\partial Q_{aero}}{\partial \theta}\big|_0 = \frac{\partial Q_{aero}}{\partial \theta}\big|_{(\omega_{rated}, V_{op}, \theta_{op}=0)}$ refers to the partial derivative of the torque with respect to θ, evaluated at the operational point, which is also the point of linearization. Note that the term $\frac{\partial Q_{aero}}{\partial \omega}\big|_0$ is often neglected as it is relatively small compared to $\frac{\partial Q_{aero}}{\partial \theta}\big|_0$ [47]. Eq. 2.29 has the form of a linear second order differential equation with a mass, damping and stiffness term, which is well known from oscillating mechanical systems. For this kind of system a natural frequency ω_n and damping ratio ζ can be defined:

$$\omega_n = \sqrt{\frac{k}{m}} \tag{2.30}$$

$$\zeta = \frac{c}{2\sqrt{km}} \tag{2.31}$$

By using ω_n and ζ, Eq. 2.29 can be expressed in the canonical form of a single degree of freedom oscillator:

$$\ddot{\phi} + 2\,\zeta\,\omega_n\,\dot{\phi} + \omega_n^2\,\phi = 0 \tag{2.32}$$

By combining Eqs. 2.29, 2.30 and 2.31 the proportional and integral gain of the PI-controller can be expressed as a function of ω_n and ζ [47]:

$$k_P = \frac{2\,\zeta\,\omega_n\,I_{rotor} - \frac{1}{\eta}\,\frac{\partial Q_{gen}}{\partial \omega}\Big|_0}{-\frac{\partial Q_{aero}}{\partial \theta}\Big|_0} \tag{2.33}$$

$$k_I = \frac{\omega_n^2\,I_{rotor}}{-\frac{\partial Q_{aero}}{\partial \theta}\Big|_0} \tag{2.34}$$

Thus by choosing the natural frequency (which is also referred to as the closed-loop controller frequency) and damping ratio of the closed-loop control system, the proportional and integral gains can be calculated. The process of determining k_P and k_I is referred to as controller tuning. The natural frequency and damping ratio define the dynamic behaviour of the control system. As a general rule of thumb a higher natural frequency results in a faster response and a higher damping ratio in less overshot [48]. This behavior is illustrated in Figure 2.12, which shows the step response of a controller for different values of ω_n and ζ.

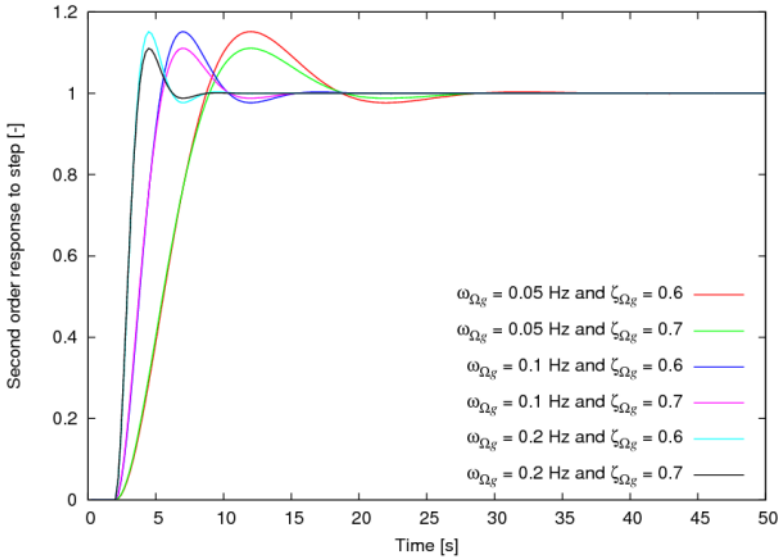

Figure 2.12: Response of a second order closed-loop controller to a step input for different natural frequencies and damping ratios. Figure taken from [48].

2.2.1.3 Gain Scheduling

Expressions (2.35) and (2.36) for the proportional and integral gain are only valid at the operational point, at which the drivetrain equation is linearized. In order to be able to use the PI-controller for the entire full load region, the expressions for k_P and k_I must be generalized as a function of the pitch angle [48]:

$$k_P(\theta) = \frac{2\,\zeta\,\omega_n\,I_{rotor} - \frac{1}{\eta}\,\frac{\partial Q_{gen}}{\partial \omega}\Big|_{\omega_{rated}}}{-\frac{\partial Q_{aero}}{\partial \theta}} \tag{2.35}$$

$$k_I(\theta) = \frac{\omega_n^2\,I_{rotor}}{-\frac{\partial Q_{aero}}{\partial \theta}} \tag{2.36}$$

The partial derivative of the generator torque with respect to the rotational speed is a constant, which can be determined based on the chosen control strategy [48]:

$$\frac{\partial Q_{gen}}{\partial \omega}\Big|_{\omega_{rated}} = \begin{cases} 0 & \text{for constant torque control} \\ -\frac{P_{rated}}{\omega_{rated}^2} & \text{for constant power control} \end{cases} \tag{2.37}$$

The partial derivative of the aerodynamic torque with respect to the pitch angle, which is also called the pitch sensitivity or aerodynamic gain [48], changes for different pitch angles. It must therefore be expressed as a function of θ. This can be done empirically by applying a change in θ for different initial values of θ and then determining the resulting change in aerodynamic torque. This procedure is illustrated in Figure 2.13 on the example of the Tjaereborg turbine [48]. It can be seen that for a change in pitch angle a certain change in power and therefore change in aerodynamic torque occurs. It should be noted that for determining the change in Q_{aero} the frozen wake assumption is used, which means that the initial change in Q_{aero} is used and not the final change after the inflow has reached its new state of equilibrium.

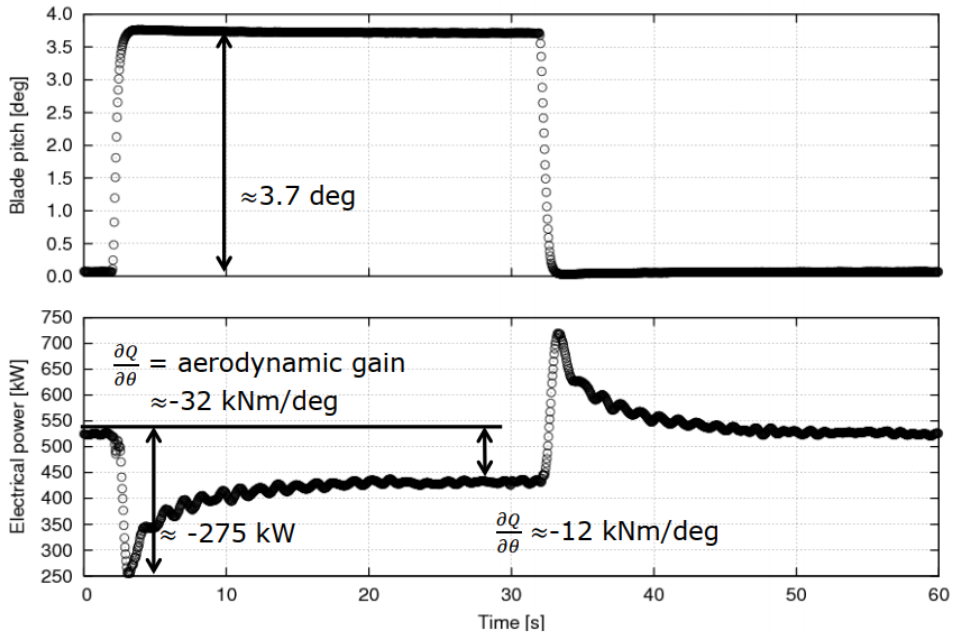

Figure 2.13: Change in aerodynamic torque caused by change in pitch angle for the Tjaereborg turbine by Øye. Figure taken from [48].

By repeating this procedure for a range of different θ and fitting a curve to the resulting data points, the desired relation between pitch sensitivity and pitch angle can be obtained. Either a linear or quadratic fit can be used. Based on the obtained curve fit, a gain factor function can be formulated [17]:

$$\eta_K(\theta) = \frac{1}{1 + \frac{\theta}{K_1} + \frac{\theta^2}{K_2}} \tag{2.38}$$

Hereby K_1 describes the coefficient of the linear term and K_2 the coefficient of the quadratic term obtained in the curve fitting. The proportional and integral gains of the PI-controller are then expressed as a function of θ as followed [17]:

$$k_P(\theta) = k_P \, \eta_K(\theta) \tag{2.39}$$

$$k_I(\theta) = k_I \, \eta_K(\theta) \tag{2.40}$$

It should be noted that the here presented theory describes only the basic principle of classical wind turbine control strategy. In the practical implementation of a wind turbine controller many additional aspects must be considered like the application of various signal filters, turbine start-up and shut-down and transition between different control regions. For more details refer to [17].

2.2.2 New control strategies for floating wind turbines

When applying the described classical control strategy directly to a FOWT, a phenomenon called pitch instability can occur. Due to the motion of the floating substructure, in particular due to the pitch motion, a FOWT experiences very large motion, compared to a bottom-fixed turbine. This motion also changes the relative wind speed seen by the rotor. Above rated wind speed this effect can lead to the aforementioned pitch instability. When the turbine is moving into the wind, the relative wind speed increases, which leads to a decrease in thrust force. This is indicated qualitatively in Figure 2.14, which displays the thrust curve of the DTU 10 MW RWT. The decrease in thrust force amplifies the motion in upwind direction. When the turbine is moving in downwind direction, the relative wind decreases and the thrust force increases, which again amplifies the turbine's motion. Above rated wind speed the turbine therefore experiences negative aerodynamic damping, which can lead to unstable operational conditions. The effect is the highest directly above rated wind speed, as here the negative gradient of the thrust force is the highest.

A possible solution to prevent this pitch instability is the application of a slower controller. This means the use of a standard wind energy controller, as it was described in the previous section, but tuned for a frequency below the natural pitch frequency of the FOWT. If the natural frequency of the controller is sufficiently far below the natural pitch frequency, this can prevent pitch instability from occurring. However, as the natural pitch frequency of a FOWT is usually very low, this also results in a very slow controller, which cannot properly respond to very fast changes of the wind speed, leading to some potential overshoots in the rotor speed, eventually damaging the generator or even resulting in frequent shutdowns. This can be problematic for example in the case of a large wind gust, not only damaging the generator, but also exposing the wind turbine to extreme loads.

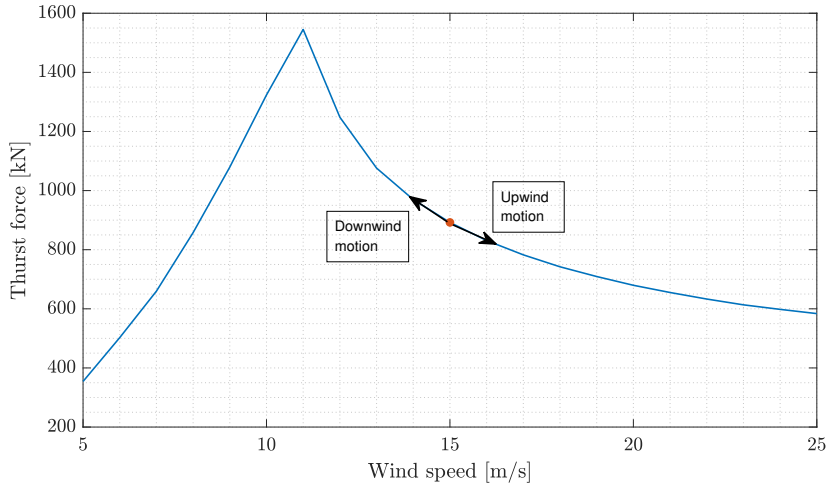

Figure 2.14: Change of thrust force of DTU 10 MW RWT due to fore-aft motion of turbine.

One solution to deal with this overshoot in the rotor speed could be reducing the rated generator speed. By doing this, larger deviations of generator speed could be tolerated without shutdown, however leading to a reduced output power and an increase in its standard deviation, becoming an unfeasible solution.

There have been several approaches to solve this problem by accounting for the tower fore-aft motion. A method proposed by van der Veen et al. (2012) [49] and Fischer (2013) [50] is the inclusion of an additional tower velocity loop into a conventional PI controller. A simple gain is multiplied by the tower-top fore-aft velocity in order to achieve the so-called *"parallel compensation"* action. With the inclusion of this new gain, the new change in pitch angle is calculated as previously seen in Eqs. 2.25 and 2.26 with the addition of a new term proportional to the tower-top fore-aft velocity:

$$\Delta\theta = k_P\,(\omega - \omega_{rated}) + K_{tt}\,v_{tt} + k_I \int_0^t (\omega - \omega_{rated})\,dt \tag{2.41}$$

$$\Delta\theta = k_P\,\dot{\phi} + K_{tt}\,v_{tt} + k_I\,\phi \tag{2.42}$$

Hereby K_{tt} [rad/(m/s)] and v_{tt} stand for the tower-top loop gain and the tower-top fore-aft velocity, respectively. Note that this is still an active solution consisting of using collective blade pitch actuators as the control input. It is important to note that this additional loop should only be active above rated wind speed, therefore a switching logic between the different control regions must be implemented. Another aspect to consider is that the readily available signal in a wind turbine is usually

the tower acceleration and not the tower velocity. Signal filtering and other practical aspects in implementing the *"parallel compensation"* technique are further discussed in Fischer (2013) and van der Veen et al. (2012). The challenge of obtaining the velocity signal into the controller will be addressed in the following section.

CHAPTER 3

Pre-simulation of the new controller

The *"parallel compensation"* control strategy presented in the previous chapter requires the tower velocity as an input to the controller. While this is relatively easy to implement in an aero-elastic software in which the tower velocity is calculated anyway, it poses a challenge for a physical model in which the tower velocity is not measured directly. In this chapter two different ways to obtain the tower-top velocity are presented. An example where the velocity is inferred from the differentiation of the floater motion after applying different filters to the signals is shown. The same is done for the other approach, integrating the signal coming from an accelerometer attached to the tower-top. Then, in order to make a first assessment of the new controller strategy, different controllers are numerically simulated in HAWC2. Lastly, the performance of the different controllers and control strategies are compared to each other.

3.1 Tower-top velocity calculation

The real-time tower-top fore-aft velocity can be obtained either by using the information from the floater motion or by integrating the tower-top fore-aft acceleration signal coming from an accelerometer. Note that the main purpose of this section was to develop a real-time code in C with the two alternatives that could be implemented in the real lab controller and to assess the preliminary simulations run in HAWC2.

3.1.1 Differentiation of the floater motion

The displacement of a point at the tower-top z_{tt} can be estimated by the linear superposition of the reference point displacement (surge ξ_1) and the displacement due to a rotation (pitch ξ_5). In the case of the lab-scale floating wind turbine model, the tower-top fore-aft displacement x_{tt} can be defined as:

$$x_{tt} = \xi_1 + \sin(\xi_5)\, z_{hub} \tag{3.1}$$

Then, by doing the real-time derivative of the signal x_{tt}, the tower-top fore-aft velocity v_{tt} can be obtained. However, since the real-time surge and pitch motion of the floater signals come from an instrumentation system, a real-time digital filtering of these signals is required before the differentiation, in order to remove high frequency noise or some signal drift in the measured data. After having done some research, three different filters were tried out (see Table 3.1). The canonical filters were extracted from [51] and the continuous filter was extracted from [17]. For comparison purposes, a zero-phase Butterworth digital filter was computed with both the *butter* and *filtfilt* MATLAB functions.

Table 3.1: Different kind of tested filters for the differentiation approach.

Type	**Order**	**Frequency domain**	ζ **[-]**	**Cut-off frequency [Hz]**
Zero-phase Butterworth	3^{rd}	Low-pass	-	2
Canonical form	1^{st}	Low-pass	$\frac{1}{\sqrt{2}}$	2
Continuous form	2^{nd}	Low-pass	$\frac{1}{\sqrt{2}}$	2
Canonical form	2^{nd}	Low-pass	$\frac{1}{\sqrt{2}}$	2

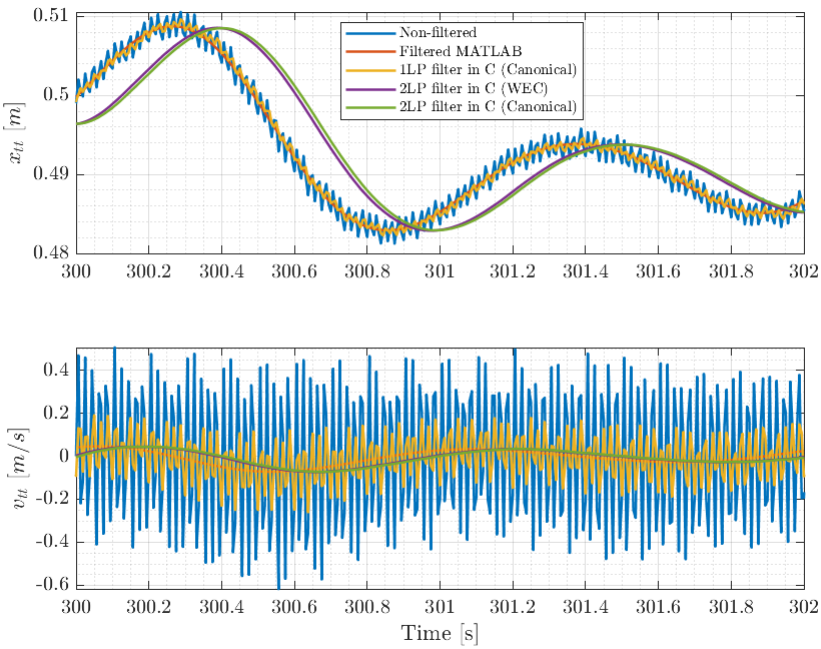

Figure 3.1: Filtered tower-top fore-aft displacement and velocity for different kinds of filters.

The performance of the filters was tested by analyzing some data from the previous 2017 TetraSpar experimental campaign [52, 53]. The real-time filtering and differentiation of the signals was computed in C language for all the different filters, except for the MATLAB non real-time filter. The results for a given data set and time window are shown in Figure 3.1.

Analyzing the results, the non-filtered tower-top fore-aft displacement is the result of applying Eq. 3.1 to the experimental data set. The MATLAB filtered signal seems to be the best fit to the raw signal, however this signal processing cannot be carried out in real time, as it requires the whole data set. The real-time 1^{st} order low-pass filter seems to match the MATLAB reference signal quite good, but it still contains some high frequency noise, which is critical when applying the numerical differentiation to obtain the nacelle fore-aft velocity. The two real-time 2^{nd} order low-pass filters seem to match the raw signal quite good despite of the fact that there is a phase shift of roughly 0.1 seconds as a result of applying such a filter. Note that after having done a frequency spectrum analysis of the signals by means of a PSD analysis, all of the signals were quite similar to each other.

3.1.2 Integration of the fore-aft nacelle acceleration

If an accelerometer is attached to the tower-top of the model to capture the tower-top fore-aft acceleration, the tower-top fore-aft velocity can be easily computed by integrating the signal over time. In the same way as explained in the previous section, the acceleration signal has to be filtered out in order to remove high frequency noise, frequency drift and a certain offset. Similar filters were used for this approach (see Table 3.2).

Table 3.2: Different kind of tested filters for the integration approach.

Type	**Order**	**Frequency domain**	ζ **[-]**	**Cut-off frequency [Hz]**
Zero-phase Butterworth	3^{rd}	Band-pass	-	[0.05 2]
Canonical form	1^{st}	Low-pass	$\frac{1}{\sqrt{2}}$	2
Continuous form	2^{nd}	Low-pass	$\frac{1}{\sqrt{2}}$	2
Canonical form	2^{nd}	Band-pass	$\frac{1}{\sqrt{2}}$	[0.1 2]

The results for the same given data set and the same time window are shown in Figure 3.2. For the numerical integration, a trapezoidal method was implemented as:

$$v[n] = v[n-1] + \frac{a[n]+a[n-1]}{2}\Delta t \tag{3.2}$$

Where $v[n]$ is the velocity for time step n, which depends on the velocity in the previous time step $v[n-1]$ and the accelerations for both the current and previous time step $a[n]$ and $a[n-1]$. Unlike the differentiation approach, the results seem to have an important offset even though all of them follow the trend quite well. This

could be related to the real-time numerical integration method used because the MATLAB filtered signal does not present such an offset.

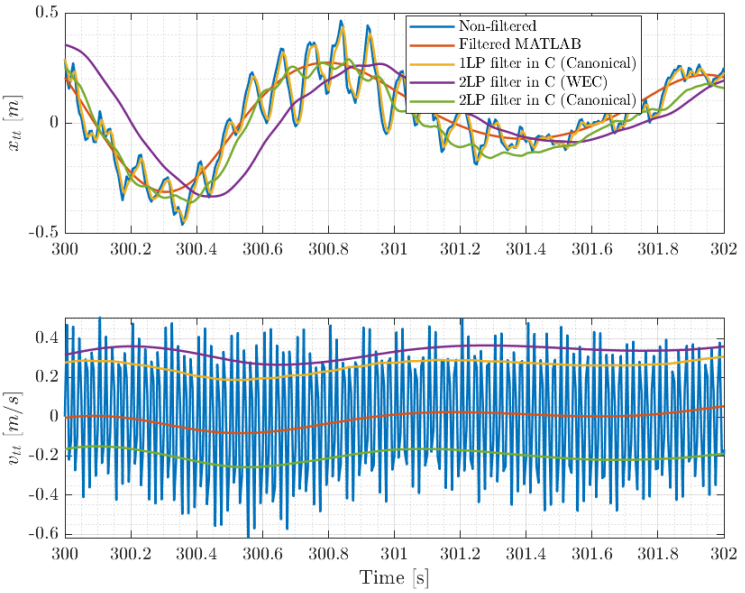

Figure 3.2: Filtered tower-top fore-aft acceleration and velocity for different kinds of filters.

3.2 Numerical controller simulations

In order to make a first assessment of the new controller strategy, the controller is simulated numerically in HAWC2. A baseline controller without the new tower-top velocity loop and 2 different versions of the basic DTU Wind Energy controller with the new tower-top velocity loop included are simulated in HAWC2 and their performance compared to each other. The purpose of the simulation presented in this section is not to carry out an exact tuning of the controller parameters, but to validate the functionality of the controller on a numerical level. Because the numerical model of the new TetraSub concept foundation was not available yet, the simulations were carried out using the HAWC2 model of the 1:60 scaled TetraSpar floater with the 1:60 DTU 10 MW RWT mounted on it. The TetraSpar floater was designed by SOT and the scaled model was used in a test campaign at DHI in 2017 [52, 53]. The natural pitch frequency of this floater is 0.24 Hz.

The baseline controller is a slow detuned controller with the new tower-top velocity gain K_{tt} set to zero. This controller is expected to be stable because it was tuned for a low closed-loop controller frequency of 0.12 Hz, which is half the natural pitch frequency of the floater. The second controller is a partially detuned controller, which has a higher dynamic response than the baseline controller, but is not unstable. The last controller is a fast land-based controller, which is inherently unstable without the tower-top velocity loop, denoted in the following as onshore controller. The K_p and K_i values for all controllers are obtained based on the pole-placement method in HAWCStab2. After defining a natural controller frequency and damping ratio, HAWCStab2 calculates the gains of both the torque controller for partial load and the pitch controller for full load. All controllers use constant torque strategy above rated power. The new controller includes also a low-pass tower-top velocity filter. After a quick preliminary assessment of the controller performance, the filter frequency was set to 0.5 Hz, which is above all natural floater frequencies, but below the 1P frequency.

It should be pointed out that the HAWCStab2 model is based on an onshore turbine model. It can therefore be expected that the defined natural controller frequency does not correspond exactly to the resulting controller frequency of the floating wind turbine. Table 3.3 shows an overview of the parameters of all applied controllers.

Table 3.3: Parameters of simulated controllers, obtained by controller tuning in HAWCStab2.

	Baseline detuned	**Partially detuned**	**Onshore**
Tuning frequency [Hz]	0.12	0.75	1
Torque K_p [Nm/(rad/s)]	0.23065	1.44158	1.92211
Torque K_i [Nm/rad]	0.12242	4.85235	8.62640
Pitch K_p [rad/(rad/s)]	0.010622	0.06664	0.088853
Pitch K_i [rad/rad]	0.005742	0.22431	0.39877

The controllers are simulated under turbulent wind and irregular wave conditions. Two environmental conditions (ECs) from the 2017 TetraSpar campaign are chosen: EC 5 at rated wind (11.4 m/s at full scale) speed and EC 6 above rated wind speed (17 m/s at full-scale). Table 4.8 shows an overview of the ECs, which will also be used in the test campaign. The measured surface elevation from the 2017 TetraSpar campaign is used directly as input to HAWC2. The turbulent wind field is created in HAWC2 with a defined turbulence intensity of 3.5%, which corresponds to the measured turbulence intensity of the wind generator at the DHI test facilities.

As a first step, a 300 s time simulation is carried out for each controller, in which the new tower-top velocity loop is activated at T = 150 s. Based on preliminary simulations, the value of K_{tt} for the onshore and the partially detuned controller is chosen as 0.8 rad/(m/s). Figure 3.3 shows the resulting blade pitch angle, the rotational speed, the floater pitch angle and the aerodynamic thrust time-series for both EC 5 and EC 6. In the case of the fast onshore controller, the stabilizing effect of the new tower-top velocity loop can be clearly seen. All quantities show very large oscillations before T = 150 s. After the tower-top velocity loop is activated, the controller manages to stabilize the turbine, even though in case of EC 6 the oscillations still seem to be slightly higher than the detuned baseline controller.

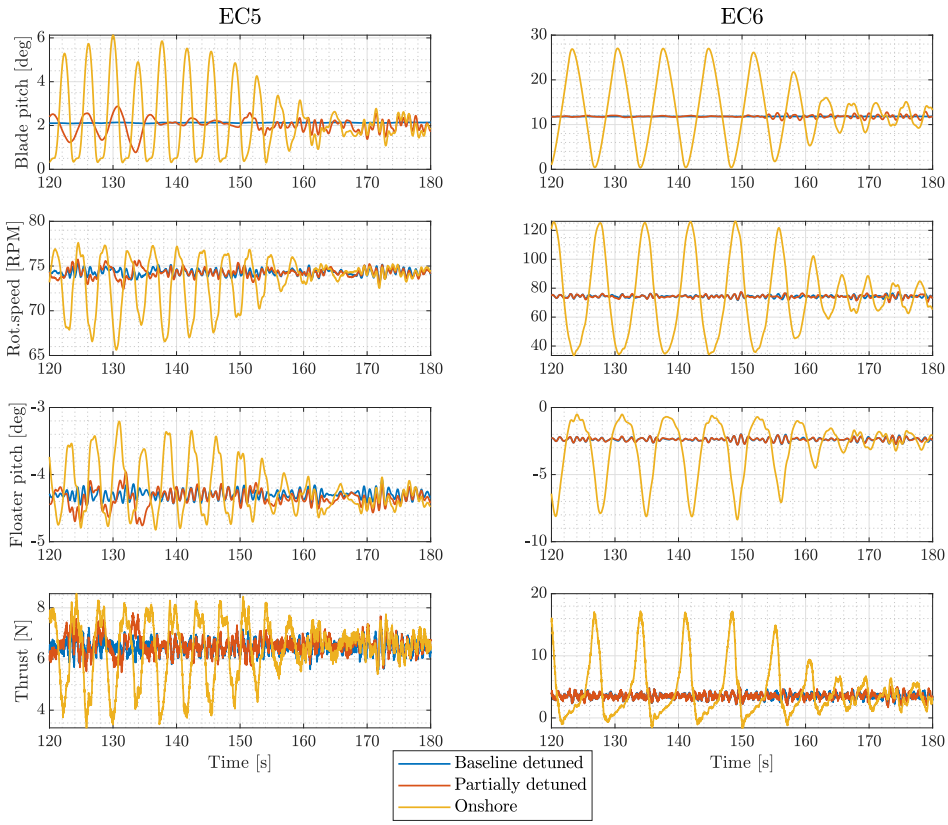

Figure 3.3: Comparison of different controllers under turbulent wind + irregular waves at rated wind speed (EC 5) and above rated wind speed (EC 6). The new tower-top velocity loop is activated at T = 150 s.

The partially detuned controller is already quite close to the behavior of the baseline controller. However, in the case of EC 5 the activation of the new tower

velocity loop seems to slightly reduce the oscillations of rotational speed and floater pitch angle. In the case of EC 6 barely any difference can be seen between the partially detuned controller and the baseline controller, probably because the gradient of the thrust is lower for this wind speed, and hence the triggered instability has a minor effect. Regarding the blade pitch angle, the activation of the tower-top loop seems to slightly increase the pitch motion.

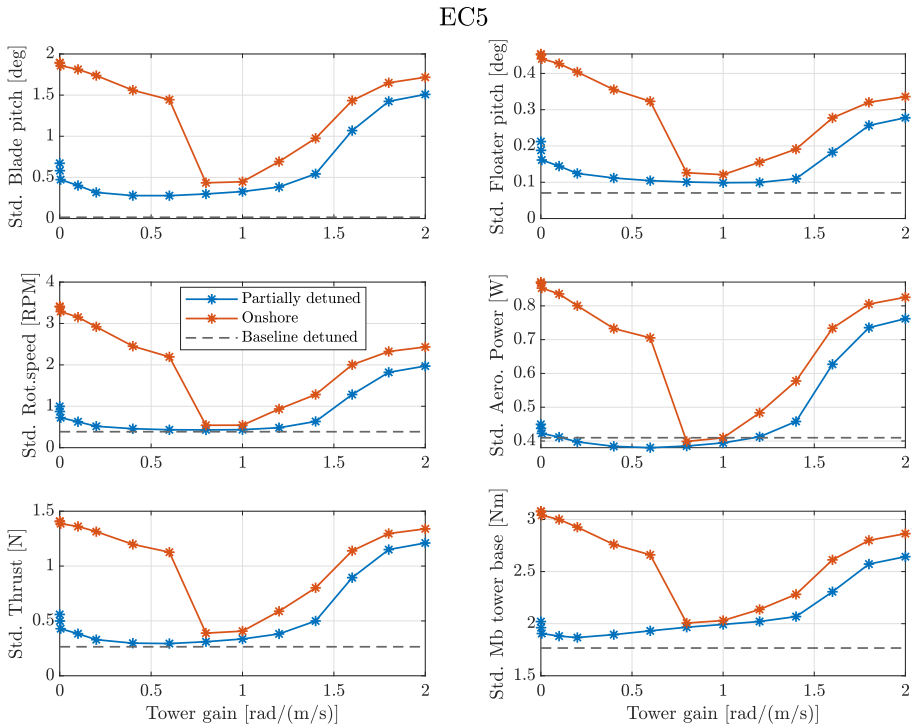

Figure 3.4: Standard deviations for a 10 min turbulent wind + wave simulation under EC 5, using different controllers and tower-top velocity gain values.

In order to evaluate the influence of different K_{tt} values, the above described 10 minutes turbulent wind and irregular waves simulation is repeated for a range of different K_{tt} values between 0 and 2 rad/(m/s), for both the partially detuned and the onshore controller. For each simulation the standard deviation of the blade pitch angle, the floater pitch angle, the rotational speed, the aerodynamic thrust, the aerodynamic power and the bending moment in the fore-aft direction at the tower base is determined. Figure 3.4 shows the standard deviations as a function of K_{tt} for the EC 5 simulations and Figure 3.5 for the EC 6 simulations. The standard deviations obtained with the slow baseline controller without the tower velocity loop are shown as a reference in black dashed lines.

Looking at the results of EC 5, starting from $K_{tt} = 0$, increasing K_{tt} leads to smaller standard deviation of all quantities and therefore a lower dynamic response of the turbine. The optimum K_{tt} for the fast onshore controller seems to be reached around 0.8 rad/(m/s). Increasing the tower velocity gain further, results in higher standard deviations, as the increased pitch activity due to the high K_{tt} value increases the dynamic response of the turbine. In the case of the partially detuned controller, the optimal K_{tt} seems to be reached at lower values. The lowest standard deviation of the bending moment is obtained for $K_{tt} = 0.2$ rad/(m/s), while the other quantities have the lowest standard deviation for $K_{tt} \approx 0.5$ rad/(m/s). Both the fast onshore and the partially detuned controller get close to the results of the baseline controller for the respective optimal K_{tt}, with the partially detuned controller having slightly lower standard deviations.

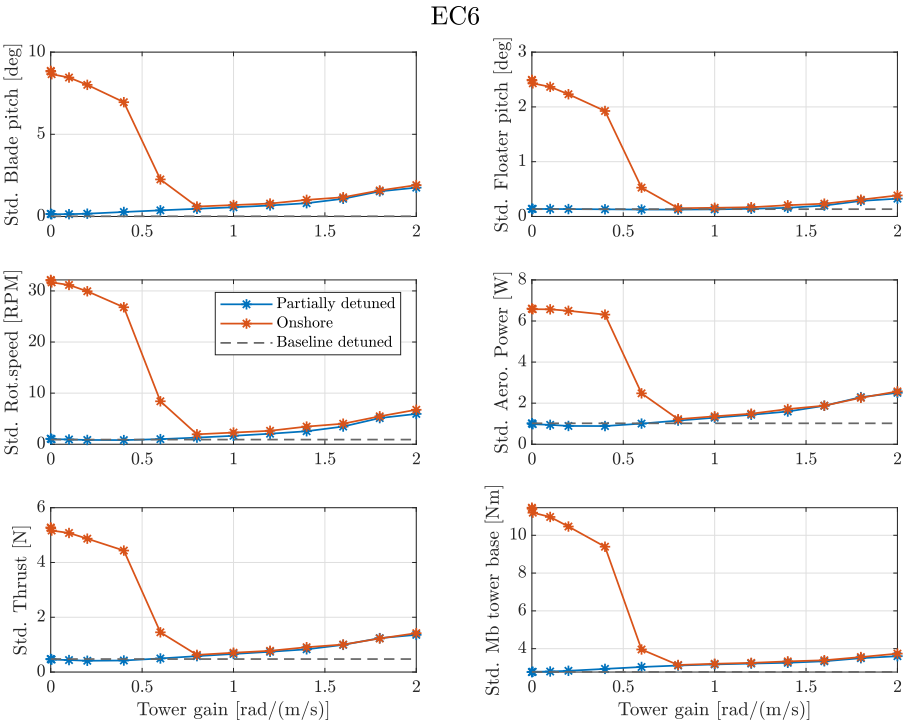

Figure 3.5: Standard deviations for a 10 min wind + wave simulation under EC 6, using different controllers and tower-top velocity gain values.

For the case of EC 6, the onshore controller is clearly unstable for low K_{tt} values. Increasing K_{tt} quickly reduces the dynamic response, again reaching the optimal K_{tt} value at 0.8 rad/(m/s). For higher tower-top velocity gains, the dynamic response increases again, but less than in the case of EC 5. Looking at the results of the par-

tially detuned controller, the results for very low tower-top velocity gains seem to be already at the same level as the baseline controller. Increasing K_{tt} results in slightly increasing standard deviations. For tower-top velocity gains above 1 rad/(m/s) the results for the partially detuned controller and the onshore controller are almost identical.

The above presented simulations do not have the intention to serve as exact tuning of the controller parameters. The model used in the simulations is not the floater used in the measurement campaign. Furthermore, preliminary simulation showed that there is a high correlation of the optimal K_{tt} value to the chosen tower velocity filter frequency and the natural controller frequency. The exact parameters of the applied controllers must therefore be tuned experimentally during the measurement campaign. The presented simulation results however show clearly the functionality of the new controller at a numerical level. When activated, the new tower velocity loop is capable of stabilizing a previously unstable controller. Choosing an appropriate K_{tt} value reduces the dynamic response of the faster controllers and leads to results at a similar level as the slower baseline controller.

CHAPTER 4
Experimental Setup

In this chapter the design process and underlying design criteria of the 1:60 scale DTU 10MW RWT model are explained. Afterwards, the 1:60 TetraSub concept foundation model, designed and provided by SOT, is presented. Likewise, the mooring line system used for the experiments is briefly discussed. Then, the experimental setup of the campaign is presented. First, the wave basin at which the experimental tests were conducted is described. The wind maker together with the wave maker used for creating the model scale wind-wave climates are presented, as well as the environmental conditions deployed in the test campaign. Finally, the DAQ system as well as all the measuring equipment used during the campaign are explained.

4.1 The DTU-TetraSub Wind Turbine Model

The small-scale floating wind turbine model deployed in the measurement campaign consists of the 1:60 scaled DTU 10MW reference wind turbine [54] mounted on the TetraSub concept foundation model designed and provided by SOT. The combined TetraSub floating wind turbine model assembled in the wave basin together with the mooring line system can be seen in Figure 4.1. Table 4.1 shows an overview of the general dimensions of the wind turbine model.

Table 4.1: General dimension of the lab-scale DTU10 MW RWT.

Dimension	**Model scale value**
Rotor diameter	2972 mm
Blade length	1440 mm
Hub height o. MWL	2005 mm
Tower diameter	800 mm
Tower height	1682 mm
Tower thickness	3 mm

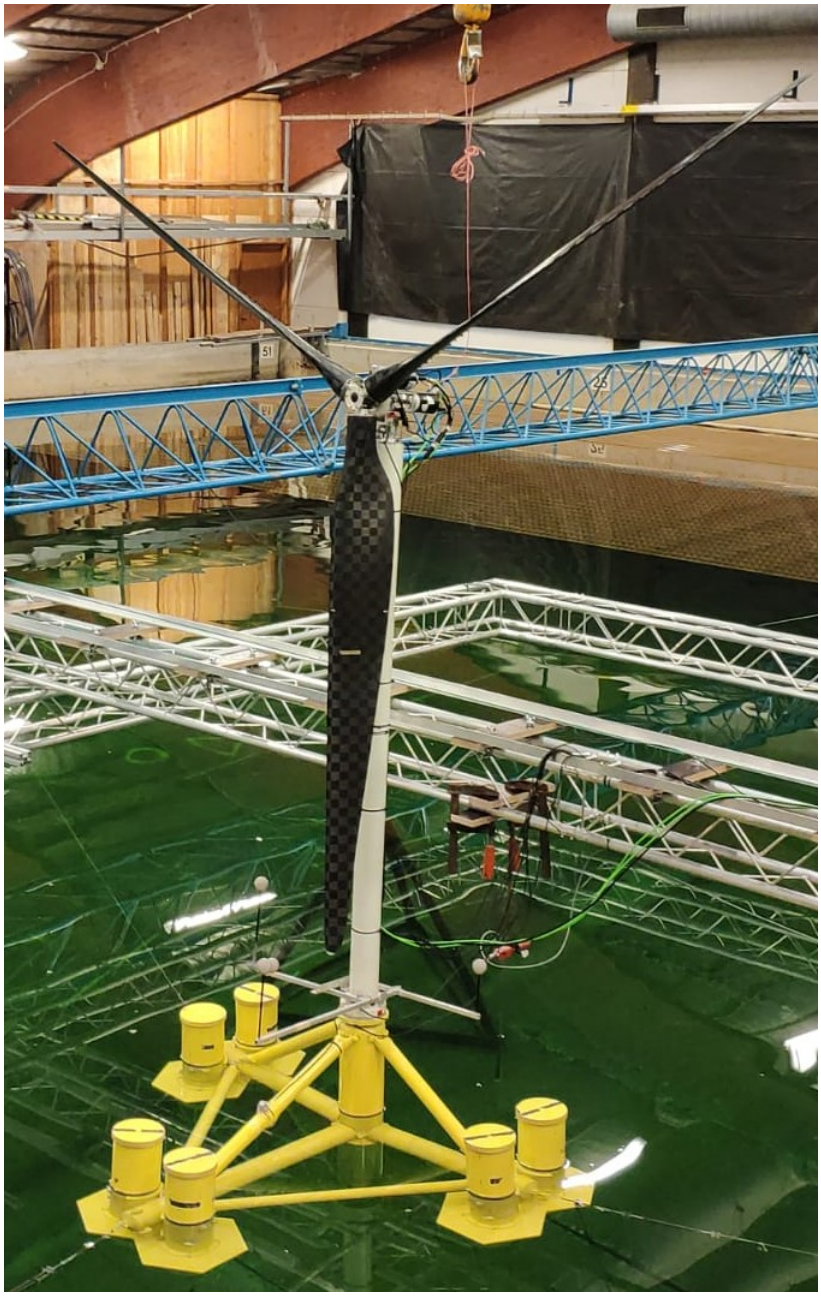

Figure 4.1: The small-scale DTU-TetraSub floating wind turbine model assembled in the wave basin.

4.1.1 Wind Turbine Design

A small-scale 1:60 model of the DTU 10MW RWT has been used in the previous years for several experimental campaigns [25, 55]. The key parameters of the DTU 10MW RWT prototype are shown in Table 4.3.

Table 4.2: Key parameters of the full-scale DTU 10MW RWT. Values taken from [54].

Wind Regime	IEC Class 1A
Cut-in Wind Speed	4 m/s
Cut-out Wind Speed	25 m/s
Rated Wind Speed	11.4 m/s
Rated Power	10 MW
Number of Blades	3
Rotor Diameter	178.3 m
Hub Diameter	5.6 m
Hub Height	119.0 m
Minimum Rotor Speed	6.0 rpm
Maximum Rotor Speed	9.6 rpm
Maximum Tip Speed	90 m/s
Hub Overhang	7.1 m
Shaft Tilt Angle	5.0 deg
Rotor Precone Angle	2.5 deg
Blade Prebend	3.332 m
Rotor Mass	227,962 kg
Nacelle Mass	446,036 kg
Tower Mass	628,442 kg

The main objective of this test campaign is to assess the performance of different control systems on the structural dynamics of the model under different environmental conditions, and hence it is important to get a close dynamic and elastic similarity between the model and its original prototype. The small-scale experimental tests are challenging, because of contrasting physical scaling laws for aerodynamic and hydrodynamic loads. Inertial forces, gravitational forces and viscous forces are dominating the structural response of a body. In order to reproduce the full-scale response as faithfully as possible, the ratio of these forces needs to be preserved in the lab environment.

The ratio of the different types of forces is described by a number of dimensionless parameters. The Froude number, Fr, describes different flow regimes of open channel flow. It is defined as the ratio between inertial and gravitational forces as:

$$Fr = \frac{\text{Inertial forces}}{\text{Gravitational forces}} = \frac{u}{\sqrt{gL}} \tag{4.1}$$

The Reynolds number, Re, accounts for the ratio of inertial forces to viscous forces within a fluid which is subjected to relative internal movement due to different fluid velocities, defined as:

$$Re = \frac{\text{Inertial force}}{\text{Viscous force}} = \frac{uL}{\nu} \tag{4.2}$$

Where L is a characteristic dimension, g is the acceleration of gravity, u is a characteristic velocity and ν is the kinematic viscosity of the fluid. In general, it is not possible to match both the Fr number for gravity waves and the Re number for viscous effects and boundary layer separation effects. If the Re and Fr numbers need to be kept constant, then the ratio between these numbers should also be preserved as:

$$\frac{Re}{Fr} = \frac{\sqrt{gL^3}}{\nu} \tag{4.3}$$

However, meeting the requirement of a constant ratio of these physical magnitudes would imply either being able to change the gravitational acceleration or the kinematic viscosity of the fluid, i.e. performing the experiments with a fluid different to water, but neither are considered feasible for model tests [56]. Since wave propagation is mainly dominated by the Fr number, it has become common to run offshore industry and floating bodies experiments by preserving this number [57]. So, for the 1:60 DTU 10MW RWT model, a geometric scaling ratio λ=l_p/l_m=60 was chosen, where the subscripts m and p stand for full-scale *prototype* and small-scale *model*, respectively. A summary of the selected scaling factors developed in [58] are shown in Table 4.3.

Table 4.3: Scaling factors for the 1:60 DTU 10MW RWT model.

Description	full-scale dimension	Scaled model dimension
Length	l_p	$\lambda^{-1} l_p$
Mass	m_p	$\lambda^{-3} m_p \frac{\rho_m}{\rho_p}$
Time	t_p	$\lambda^{-1/2} t_p$
Frequency	f_p	$\lambda^{1/2} f_p$
Velocity	u_p	$\lambda^{-1/2} u_p$
Acceleration	a_p	a_p
Angle	ϕ_p	ϕ_p
Angular velocity	ω_p	$\lambda^{1/2} \omega_p$
Angular acceleration	α_p	$\lambda \alpha_p$
Forces	F_p	$\lambda^{-3} F_p \frac{\rho_m}{\rho_p}$
Moments	M_p	$\lambda^{-4} M_p \frac{\rho_m}{\rho_p}$
Bending stiffness	EI_p	$\lambda^{-5} EI_p \frac{\rho_m}{\rho_p}$

The rotor aerodynamics are heavily influenced by the Re number. As aforementioned, it is not possible to keep Re constant, which for the small-scale model is

indeed very low and a geometrical scaling would affect the aerodynamic performance of the blades. This would result in a lower aerodynamic thrust, and eventually a different mechanical power, where especially the first is of great importance to the overall dynamics of the structure. A redesign of the model-scale blades in order to match the scaled thrust-curve was therefore needed. The design work was conducted by Robert Mikkelsen based on aero-servo-elastic computations in FLEX 5. In [24] the overall criteria for the design are listed: matching both the axial blade loading and the thrust coefficient, preserving the design TSR, designing for a full-scale wind speed of 10 m/s and preserving the chord distribution. The rotor design employs a selection of special low-Reynolds-number airfoils from blade tip to root. The design preserves the tip-speed ratio (TSR) and results in a chord length increase of 75% relative to pure geometric scaling, in order to obtain the right scaled thrust [59]. Figure 4.2 shows the result of the manufactured blades for the small-scale DTU 10MW RWT model.

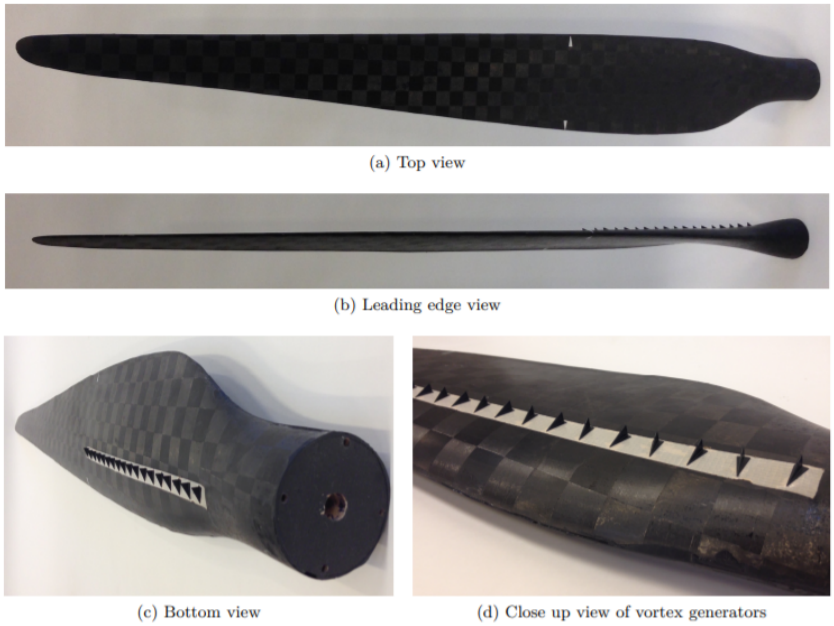

(a) Top view

(b) Leading edge view

(c) Bottom view

(d) Close up view of vortex generators

Figure 4.2: Manufactured blades for the small-scale DTU 10 MW RWT model. Figure taken from [58].

The nacelle was designed in a simplified way compared to a full-scale nacelle, even though the purpose remained the same: containing the generator and the pitch actuator, for torque and blade pitch control. This simplification was chosen in order to avoid inducing a bigger drag on the nacelle due to a streamlined nacelle design and matching the weight of the model nacelle with the scaled weight. The hub and

nacelle system can be seen in Figure 4.3. The pitch control mechanism is based on a rotatory motion converted into a translatory motion, eventually leading to an angular displacement of the blades. The introduced gear system provides the system with flexibility since the pitch actuator can be axially aligned with the hub. Two servomotors are used in order to implement the generator torque control and the blade pitch control. More details about the nacelle and hub system are described in [58]. Table 4.4 lists key parameters of the applied Servomotor. It should be noted that the maximum allowed torque is relatively low. The peak torque is listed as 0.32 NM, however the servomotor is only capable of handling this value for a very short duration. If the torque exceeds values of 0.13 - 0.14 NM for a longer period of time, the servomotor is likely to shut down. This can cause some issues with matching the rated rotor thrust, which will be discussed in Section 5.2 below.

Figure 4.3: Nacelle and hub system of the small-scale DTU 10 MW RWT model.

Table 4.4: JVL Servomotor MAC050 key parameters [58].

Mass	0.6 kg
Power	46 W
Rated torque	0.11NM
Peak torque	0.32NM

4.1.2 Support substructure

The support structure deployed in this measurement campaign is the TetraSub concept foundation, designed by SOT. Figure 4.4 shows a picture of the 1:60 scale model provided by SOT. Because the design of the floating substructure is not part of this thesis, only a general description of the model is given and some practical consideration of its application in the measurement campaign are discussed.

The TetraSub concept foundation is a semi-submersible platform for floating wind turbines. It consists of three pairs of circular buoyancy tanks, forming the tips of a triangular and one central column on which the turbine is mounted. The turbine column is not in the centre of the floater, but offset downwind between the two back sets of buoyancy tanks. This design allows an easier installation at full-scale level, as the tower has to be lifted less far outside during a harbour installation. The buoyancy tanks and central column are linked by a number of brace columns. The three fairlead points on which the mooring lines are attached are placed between each pair of buoyancy tanks at the tips of the floater. Hexagonal shaped heave plates are added at the bottom of each buoyancy tank to add additional damping. Due to the offset of the central column, the floater has an asymmetric design. From a mathematical point of view this will result in many off-diagonal elements in the system matrices of the floater and therefore a strong coupling between the different DoFs can be expected.

Figure 4.4: The lab-scale TetraSub floater designed and manufactured by SOT.

Ballasting of the Floater

In Figure 4.4, green markers can be seen on the floater, which indicate the line of flotation for the desired draft. In order to achieve this draft, the buoyancy tanks had to be ballasted. Initially water was used as ballast. Each tank was filled gradually with water until both the desired draft was achieved and pitch and roll angles were approximately equal to zero. However, during preliminary tests of the pitch stability, it was discovered that the floater reaches a new static equilibrium when pitching backwards, meaning that a new static position was reached with a pitch angle above zero. The same phenomena did not occur for negative pitch angles with the floater returning to zero pitch in this case. Initially, it was suspected that water had leaked into one of the horizontal columns, causing a shift in the center of gravity when pitching backwards. However disassembling turbine and floater showed that no water had leaked into the columns. It is therefore suspected that the water in the buoyancy tanks alone caused the shift in the center of gravity, resulting in a new static equilibrium when pitching backwards. It was therefore decided to use solid instead of liquid ballast material. In the second ballasting attempt small lead pellets were added into plastic bags in each column until the desired draft and zero inclination was achieved. Tests of the pitch stability proved that the floater returned to its original position of zero pitch. It can therefore be assumed that the water in the tanks indeed caused a shift in the center of gravity and therefore a new point of equilibrium. After finishing the ballasting, the weight of the pellet bags in each tank was documented as shown in Table 4.5. It can be seen that the ballast in the front tanks is significantly higher than in the back tanks. It should be noted that the ballasting was carried out with the first mooring line setup (see Section 4.1.3). After the change in the mooring line setup, approximately 1/6 of the ballast was removed from each tank.

Table 4.5: Ballast in each buoyancy tank.

Position	**Ballast [kg]**
Front position - left tank	2.08
Front position - right tank	2.07
Left position - front tank	0.83
Left position - back tank	0.84
Right position - front tank	0.64
Right position - back tank	0.67

It is noteworthy that the floater is very sensitive to changes in the ballasting, especially in the front tanks. Placing the lead pellets bags at different places within the tanks resulted in changes in pitch angle of up to 1°.

4.1.3 Mooring line systems

The design of the mooring line system was carried out by SOT. A first draft of the mooring line design for the model scale is shown in Figure 4.5. The reference point is located at the midpoint of the wave maker and at the bottom of the wave basin. In this way, according to the aforementioned scheme, the different anchors should be placed in the coordinates shown in Table 4.6, with the x-direction pointing away from the wave-maker, the y-direction along the wave maker and z-direction vertically upwards.

Table 4.6: First draft of the anchor coordinates (x,y,z).

Anchor 1	(-5.34, 0, 1.1)
Anchor 2	(9.67, 8.69, 1.1)
Anchor 3	(9.67, -8.69, 1.1)

For the purpose of reproducing an anchor, which is not laying on the bottom of the wave basin, as faithfully as possible, three tripods made out of aluminum with an eye on top of each other are attached to the mooring lines. Once the tripods were installed in the correct locations, these were ballasted by means of heavy stones (see Figure 4.6a). However, due to both spatial restrictions in the wave basin and the interaction between the wave paddles and the tripod itself, ML1 had to be readjusted. Limitation of offshore basin dimensions is a great challenge for model tests of deep-water mooring system. The mooring system cannot be modeled entirely in the basin with a reasonable model scale. A classical solution is based on hybrid model tests for the truncated mooring system [60]. In this case a simple geometrical truncation was applied (Figure 4.6b).

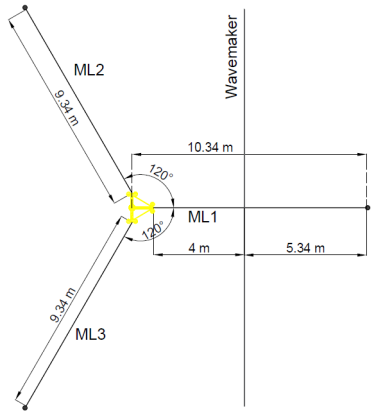

Figure 4.5: Plan view of the baseline mooring system designed by SOT.

By the time of setting up the mooring line system in the wave basin, some design considerations had to be taken into account. The three mooring lines were supposed to be identical from the fair lead to the anchor point, which was not the case for the front mooring line. There should exist a 120° spread between each mooring line, which consisted of tension springs attached to a Dyneema stiff line as seen in Figure 4.14. The mooring lines had to be pretensioned up to 11.6 N for each line and the location of the springs would depend on the pretensioning method applied.

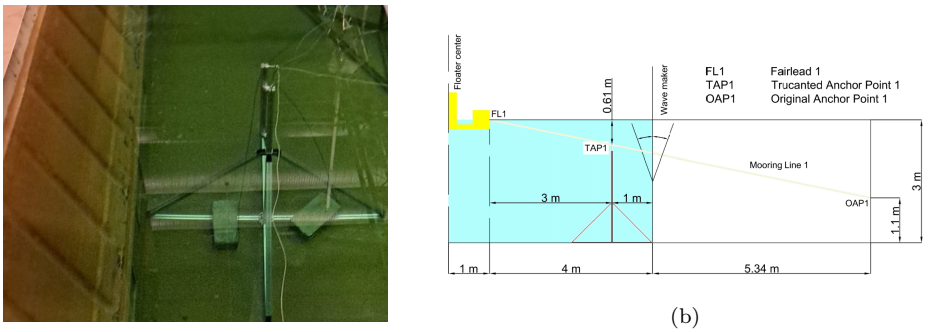

(a) (b)

Figure 4.6: Left: Installed tripod for the front mooring line (ML1) with its corresponding ballasting. Right: Elevation view of the truncated front mooring line (ML1).

According to the provided design, the spring stiffness should be 38 N/m. This spring stiffness could be reached by two different approaches. One single spring per line or two springs in parallel per line. The design characteristics of the two available type of springs can be seen in Table 4.7.

Table 4.7: Main design parameters for the two different springs.

Parameter	Stiff spring	Soft spring
Wire diameter [mm]	1.91	1.24
External diameter [mm]	25.4	12.70
Unloaded length [mm]	88.90	127.00
Max. loaded length [mm]	228.35	334.01
Maximum travel [mm]	139.45	207.01
Maximum load [N]	58.18	43.37
Initial force [N]	5.19	3.91
Spring constant [N/mm]	0.38	0.19

The provided springs had to be calibrated by hanging some weights on the springs and measuring the displacement, which allows to determine the different spring constants. Note that this was done for one single stiff spring and two soft springs in

parallel. Even though the springs were supposed to be linear, a non-linear behaviour can be observed for the two configurations above a certain force (see Figure 4.7). This might be due to either measurement errors or just a deviation in the manufacturing process.

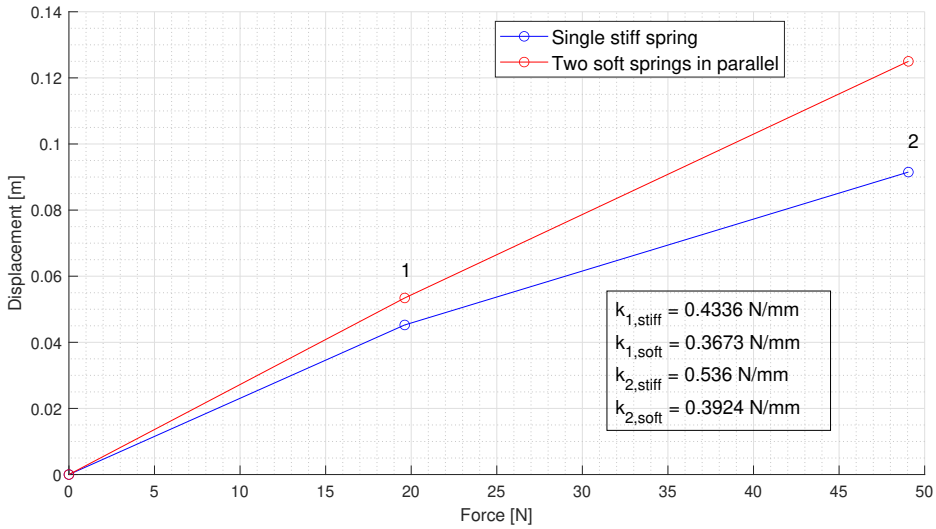

Figure 4.7: Calibration of the two springs.

In the beginning, the two soft springs in parallel was the chosen configuration (see Figure 4.14) because the maximum load of this configuration was higher than a single stiff spring per line. However, when performing the decay tests of the model, the natural frequencies of both surge and heave were significantly higher than the expected design values from SOT. As a result of this deviation, these natural frequencies coincided with the peak of some of the extreme sea states, triggering resonance, which could be confirmed after having run some wave-only tests. As the natural frequency of the surge motion of the floater is directly related to the stiffness of the mooring line system, the aim was to reduce the stiffness of the mooring line to decrease the natural surge frequency. Therefore it was decided to change the mooring line configuration by attaching two stiff springs in series to the lines. In a similar way, a single soft spring per line was discarded because the maximum load for this configuration was lower, trying to minimize the risk of leaving the elastic behaviour of the springs at some point.

During post-processing some of the first wave-only tests with the previous mooring line configuration, occasional slack events were observed in the mooring lines. After having analyzed the data, it was decided to choose a pretension of roughly 20 N for the new mooring line configuration in order to avoid null tensions events. This new higher pretension resulted in the target line of flotation being below the still water level. Therefore some ballast was taken out from the columns to readjust the line of

flotation as aforementioned.

4.2 Wave basin

The test facility at DHI contains a deep-water wave basin of dimensions 30 m x 20 m x 3 m. Regular and irregular sea states, as well as focused waves can be created by a wave generator consisting of 60 wave paddles of 0.5 m length each, which are placed on one side of the wave basin. On the other side of the basin a parabolic, porous wave absorber is installed to minimize reflections of waves back into the basin. A sketch of the wave basin is shown in Figure 4.8. The wave generator can generate multidirectional short-crested 3D waves as well as long-crested unidirectional 2D waves. The direction of the long-crested waves can also be adjusted, which allows tests of different wave inclination angles and wind-wave misalignment.

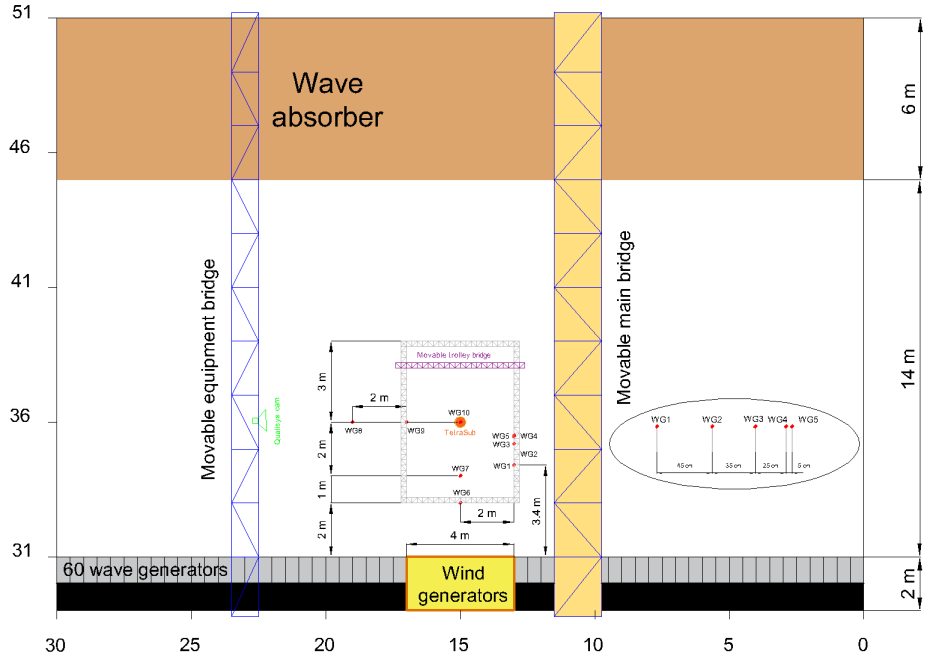

Figure 4.8: Plan view of the deep water offshore wave basin at DHI.

4.3 Wind generator

The wind generator was designed in a previous experimental campaign [23, 58]. Since DHI owned six AVL-710 fans and there existed a weight lifting limitation with the

crane at DHI, it was decided that the generator system would consist of six identical units with outlets of 2.00 m x 1.33 m each (Figure 4.9a), instead of one big wind generator. The whole wind generator system (Figure 4.9b) has an outlet of 4 m x 4 m, to cover the rotor area of the model-scale floating wind turbine, which is located a certain distance away from the wind generator itself, as the uniform wind profile decreases within distance.

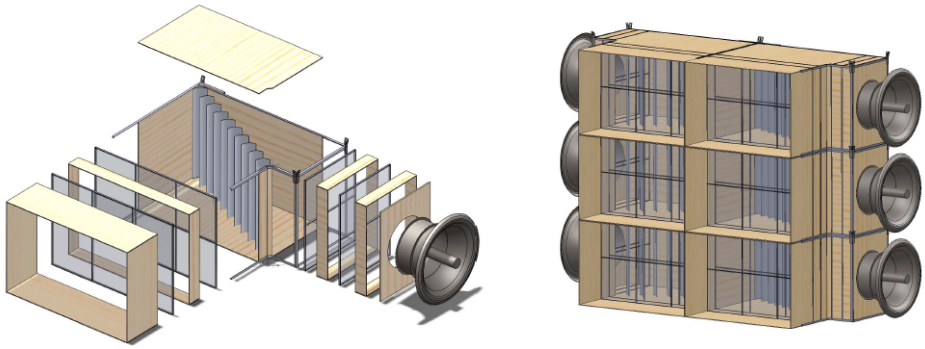

(a) (b)

Figure 4.9: Left: Exploded view of a single wind generator. Right: Sketch of the complete wind generator system. Figures taken from [58].

Each wind generator unit consisted of an AVL-710 fan, four screens aiming at decreasing the turbulence and ten guide vanes with the purpose of turning the flow 90°, without significant energy loss. In latter experimental campaigns, the motors of the fans were upgraded to provide the system with higher maximum wind speeds to avoid some issues with the automatic control of the blade pitch angle [61]. Six ABB 4kW 400V frequency converters were used to control the six fans individually.

As a result of the wave paddles being 64 cm above MWL, the wind generator support structure was constructed in a way that the wind generator system was not able to cover the entire rotor area as can be seen in the contour plots of Figure 5.3.

4.4 Environmental Conditions

The marine environment simulation is based on several techniques taking the stochastic nature of both the wind and the water waves into account. In the wave basin, a combination of significant wave height H_s, wave peak period T_p and a certain mean wind speed $\bar{V}_{mean}$ can be reproduced allowing for a large variety of combinations with these three parameters. In this campaign, two different sets of ECs are used. The first set consists of the same ECs used in the previous test campaigns at DHI, like the 2017 TetraSpar [26] or the 2017 TLP campaign [62]. Four different sea states

are selected from this set: EC 3, EC 5, EC 6 and EC 11, which correspond to wind speeds below rated, at rated, above rated and a 50 year extreme climate. However, due to limitations of the wind generator at DHI, the maximum wind speed that can be achieved is 2.2 m/s, which corresponds to a wind speed of 17 m/s at full-scale. The wind speed of EC 6 and EC 11 is therefore set to this value. Table 4.8 summarizes the parameters of the first set of ECs. The indicated simulation duration T_{dur} refers to a realization with one random seed. To represent three different seeds, the simulation duration is multiplied by 3, with each third of the simulation representing one random seed.

Table 4.8: Environmental conditions for the 2017 TetraSpar and TLP test campaigns.

Environmental condition		**EC 3**	**EC 5**	**EC 6**	**EC 11**
H_s[m]	full-scale	3.30	4.16	6.18	10.5
	Model scale	0.055	0.069	0.103	0.175
T_p [s]	full-scale	6.5	7.3	8.9	14.2
	Model scale	0.839	0.942	1.149	1.833
V_{hub} [m/s]	full-scale	8.5	11.4	17.0	17.0
	Model scale	1.1	1.47	2.2	2.2
T_{dur} [min]	full-scale	60	60	60	60
	Model scale	8	8	8	8

The second set of ECs used in this test campaign comprises five different sea states: one sea state corresponding to conditions below rated, at rated and above rated wind speed each and two sea states corresponding to extreme wind conditions. Once again, due to limitations of the wind generator, the wind speed of the three highest sea states is set to 2.2 m/s. Table 4.9 summarizes the parameters of these ECs. From this set, EC B, EC C and EC D will be additionally applied with a 30° misalignment between wind and waves. Again, the simulation duration will be increased by a factor of 3 in order to reproduce three different realizations with three different seeds.

Table 4.9: Environmental conditions for 2021 TetraSub test campaign.

Environmental condition		**EC A**	**EC B**	**EC C**	**EC D**	**EC E**
H_s[m]	full-scale	1.36	2.22	5.04	11.74	13.34
	Model scale	0.0227	0.037	0.084	0.1957	0.2223
T_p [s]	full-scale	5.69	6.52	8.99	16.88	16.27
	Model scale	0.73	0.84	1.16	2.18	2.10
V_{hub} [m/s]	full-scale	8.1	11.2	17.0	17.0	17.0
	Model scale	1.05	1.45	2.2	2.2	2.2
T_{dur} [min]	full-scale	60	60	60	180	180
	Model scale	8	8	8	24	24

Additionally to the listed irregular sea states, several regular wave conditions will be tested. A full list of these wave conditions is given in Appendix C.

4.5 Instrumentation and Data acquisition

To fully understand the performance and behaviour of the model as well as being able to fine-tune the engineering models, it is necessary to capture information by means of data. Several sensors were used along the campaign depending on the tests that were needed, for instance: calibrating the waves, measuring the wind field, carrying out the rotor ID of the clamped wind turbine, decay tests and production tests. A list of the several sensors used for the aforementioned purposes can be seen in Table 4.10.

Table 4.10: Summary of the measurements taken and the sensors used for this purpose.

Measurement	**Sensors**
Wave height	10 x wave gauge
Fore-aft shear force	Full Wheatstone bridge
Side-side shear force	Full Wheatstone bridge
Mid-tower accelerations	2 x analog 1 DoF accelerometer
Tower-top accelerations	2 x analog 1 DoF accelerometer
Floater brace acceleration	1 x analog 1 DoF accelerometer
Wind speed	5 x wind probe
Tension in each mooring line	3 x Force gauges
Floater accelerations	1 x digital 6 DoFs accelerometer
Floater surge	Qualisys: 2 cameras + 6 tracking balls
Floater sway	Qualisys: 2 cameras + 6 tracking balls
Floater heave	Qualisys: 2 cameras + 6 tracking balls
Floater roll	Qualisys: 2 cameras + 6 tracking balls
Floater pitch	Qualisys: 2 cameras + 6 tracking balls
Floater yaw	Qualisys: 2 cameras + 6 tracking balls

The DHI system consisted of three standard cabinets, two filter cabinets and one transmitting cabinet. Each standard cabinet consisted of eight slots receiving the signals coming from the sensors, allowing for a manual change of the gains and the offsets. However, the sensor parameters were managed from the DHI logging software 'Wave Synthesizer', which was also used to control the waves. From the standard cabinets, the signals were fed into the filtering cabinets after which they were logged into the 'Wave Synthesizer'. All of the signals but the ones coming from the Qualisys and the digital accelerometer were logged to the DHI system with a 160 Hz sampling frequency by means of these cabinets. A laptop especially used for the Qualisys was connected to the DHI system to log the signals related to the floater motion with a

100 Hz sampling frequency. Lastly, the digital accelerometer was directly logged into the DHI system by means of a USB connector with a 100 Hz sampling frequency.

Regarding the wind turbine DAQ, the signals coming from the generator and blade pitch motors located at hub height were digital signals being fed into a laptop brought by DTU. This laptop was connected to both a USB-6218 DAQ units from National Instruments and a MyRIO real-time embedded evaluation board made by National Instruments. A LabVIEW program run from the laptop allowed for the control of the wind turbine model. The signals coming from the two motors could be logged with a 50 Hz sampling frequency in the DTU laptop. A schematic of the wind turbine DAQ hardware setup can be seen in Figure 4.10. Note that in the scheme two DAQ units are shown, while only one DAQ unit was used in this experimental campaign.

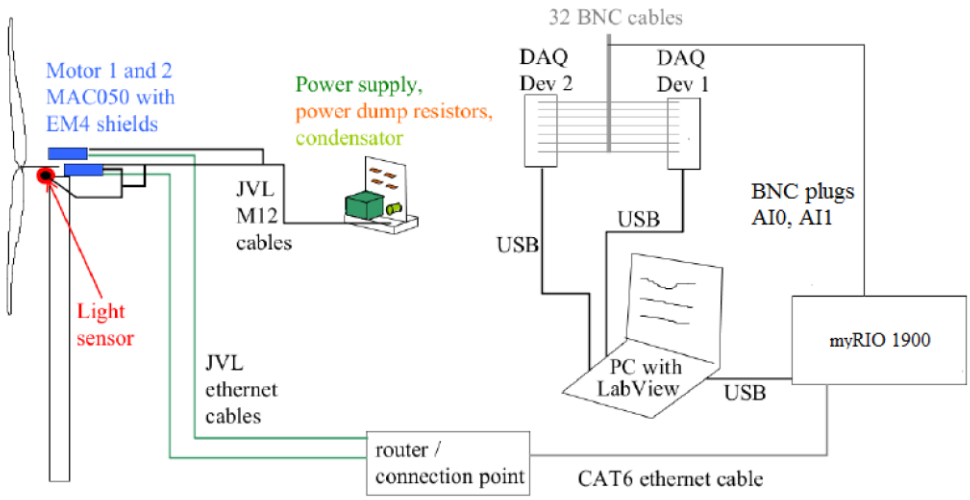

Figure 4.10: Schematic of the wind turbine data acquisition hardware setup. Figure taken from [63].

Wave Gauges

Ten wave gauges, as the ones seen in Figure 4.11, located at different locations of the wave basin were used during the experimental campaign to capture the generated wave time-series. In order to minimise uncertainty of measurements and to ensure both precision and consistency, a calibration procedure was undertaken at the beginning of each experimental day. The standard way of calibrating the different wave gauges is performed individually. However, for the purpose of saving time and setting up the tests faster, a simultaneous method for calibrating all the wave gauges at once was implemented. Since the used wave gauges are linear, only two points are needed

to determine both the slope and an offset to convert the voltage values provided by the sensors to wave height. These two points consist of the level of the wave basin when the wave paddles are either moved all the way backward or all the way forward. Once these points have been saved, the straight line is recorded and therefore all the wave gauges are calibrated simultaneously in a matter of seconds.

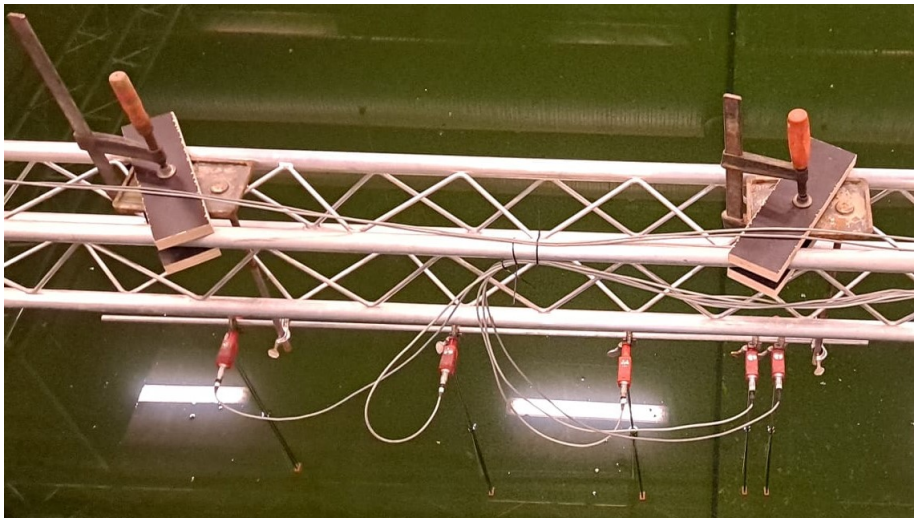

Figure 4.11: Installed wave gauges in the wave basin.

Strain Gauges

For the purpose of measuring the fore-aft and side-side shear forces experienced by the wind turbine, a two component gauge connected to a full Wheatstone bridge circuit installed in a transition piece, made out of four beams, between the tower-top and the nacelle (see Figure 4.12) is logged in the system. The two component strain gauge was calibrated once by hanging known weights of 0.1 to 2 kgs.

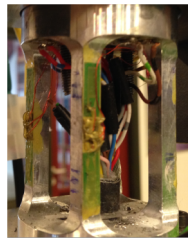

Figure 4.12: Picture of the strain gauges glued onto the four beam link between the tower-top and the nacelle.

Wind Probe

The wind field was measured by air velocity transducers, more specifically the TSI 8455 model (Figure 4.13a), suitable for low wind speed measurements in research and development labs, such as the DHI deep offshore wave basin. Model 8455 contains on-board electronics and calibration curves that provide a linear signal output. This linear signal is sent out as a voltage (V) signal, producing an analog output signal compatible with the DAQ system. It consists of a protected probe with a rugged ceramic sensor allowing for unidirectional 2D flow pass the sensor to be measured. The wind probes are calibrated once a year externally, and therefore no calibration was needed. There were five wind probes available that were mounted on a pole (see Figure 4.13b) in different configurations to reproduce the wind field in the rotor area.

(a)

(b)

Figure 4.13: Left: Air Velocity Transducer, model TSI 8455. Right: Pole used for adjusting the different wind probes at different heights.

Mooring Gauges

As aforementioned in Section 4.1.2, the floater is a semi-submersible with three spokes, thus three mooring lines are attached to the respective fair leads. Mooring line 1 was pointing upwind and the remaining mooring lines are placed in the back. Consequently, three force gauges are attached to both the corresponding fair leads and springs for each line as seen in Figure 4.14. The calibration was carried out once in a

similar way to the strain gauges by hanging some known weights to the force gauge and hence finding the relationship between the loading and the voltage output.

Figure 4.14: Force mooring gauge with the previous mooring line system.

Qualisys

The motion of the rigid floater was captured by means of a motion tracking system named Qualisys. A total of 5 reflective tracking markers were mounted on an aluminum frame fastened to the bottom of the tower together with another marker attached to a higher position of the tower, creating a three dimensional volume similar to a tetrahedron as seen in Figure 4.1. The 6 DoFs motion of the floater was recorded by two infrared cameras with a 100 Hz sampling frequency, which converted real-time analog voltage signals into the floater surge, sway, heave, roll, pitch and yaw signals. The original digital signal coming from the two cameras could be seen in a laptop enabled for the purpose of managing the whole Qualisys setup. The cameras were properly installed and fine-tuned to ensure that the wind turbine volume of motion was captured perfectly. In addition, the Qualisys system was calibrated once before the experiments to determine the exact location of both cameras with respect to the origin of the coordinate system, which coincided with the center of the floater (see Figure 4.8). Lastly, note that the accuracy of the translation motion was within 1 mm, and hence the rotational motion accuracy was roughly 0.1 °.

Accelerometers

As shown in Table 4.10, a total of 5 analog accelerometers and a digital one were used to capture different acceleration motions of the model. Two analog accelerometers were fastened perpendicularly to the transition frame between the tower-top and the nacelle to capture the tower-top fore-aft and side-to-side acceleration. In the same way, two analog accelerometers were fastened to the mid-tower position. Lastly, another analog accelerometer was mounted on the front brace of the floater to analyze possible deflections of the floater (see Figure 4.15). All of the analog accelerometers were calibrated once by placing them on a levelled horizontal plate, and hence corresponding the voltage output to the acceleration of gravity.

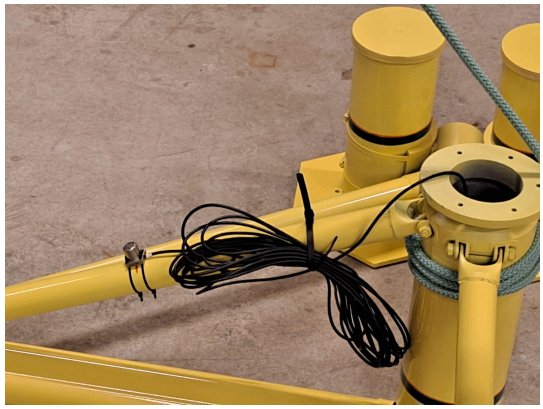

Figure 4.15: Analog accelerometer mounted on the front brace of the floater.

Then, a digital 6 DoFs accelerometer was mounted on the central column of the floater to capture both the translational and rotational accelerations of the floater. The digital signal coming from the sensor was logged in the DHI data acquisition system with a 100 Hz sampling frequency, and subsequently, converted into analog acceleration signals.

Wave paddle

The signal coming from one of the wave paddles (number 31) was logged in the DHI system for the purpose of further numerical reproduction. In addition, the stroke length of the piston was measured. If the middle position was taken as zero, the distance to the rear position was -31 cm while the distance to the front position was 28 cm [62].

CHAPTER 5

Measurement Campaign

This chapter describes the execution of the Measurement Campaign. In the first step the environmental conditions were calibrated and compared to the target conditions. Next, the Rotor ID was determined describing the characteristics of the scaled wind turbine. Then, the natural frequencies of the floater were determined by carrying out the corresponding decay tests. Finally, the controller tuning procedure for obtaining the parameters for both the detuned baseline and the new tower-top loop controller is explained.

5.1 Calibration of environmental conditions

In this section the ECs simulated at the DHI test facilities are validated and compared to the target climates. First, the wind field is measured and documented. Afterwards, the sea states, both regular and irregular, are calibrated and the results are compared to the target wave climates.

5.1.1 Wind Calibration

In order to measure the wind field at the position where the turbine was placed, a bridge with a movable trolley was used. The bridge was placed at a 5 m distance from the wind generator in transversal direction. A pole was placed on the trolley, to which several wind probes at different heights were attached. By moving the trolley across the bridge, the wind field in the rotor area could be measured at different heights and positions. In total, five wind probes were available. One wind probe was placed 2 m in front of the wind generator at hub height and remained at this position for the entire measurement campaign. Another wind probe was mounted on the pole at the hub height of 2.05 m. The three remaining wind probes were mounted on the pole in two different configurations, which are displayed in Figure 5.1. Each configuration was swept across the rotor area and measurements were taken at five different positions along the rail: 0 m, +/- 0.9 m and +/-1.8 m from the turbine position at the center of

the wind generator. The measurement positions are indicated as P1 to P5 in Figure 5.1, as well as the position of the wind probe in front of the wind generator WP1. By sweeping the pole in both configurations across the rotor plane, the wind speed was measured at seven different heights above the SWL centered around hub height: [0.25, 0.85, 1.45, 2.05, 2.65, 3.25, 3.85] m.

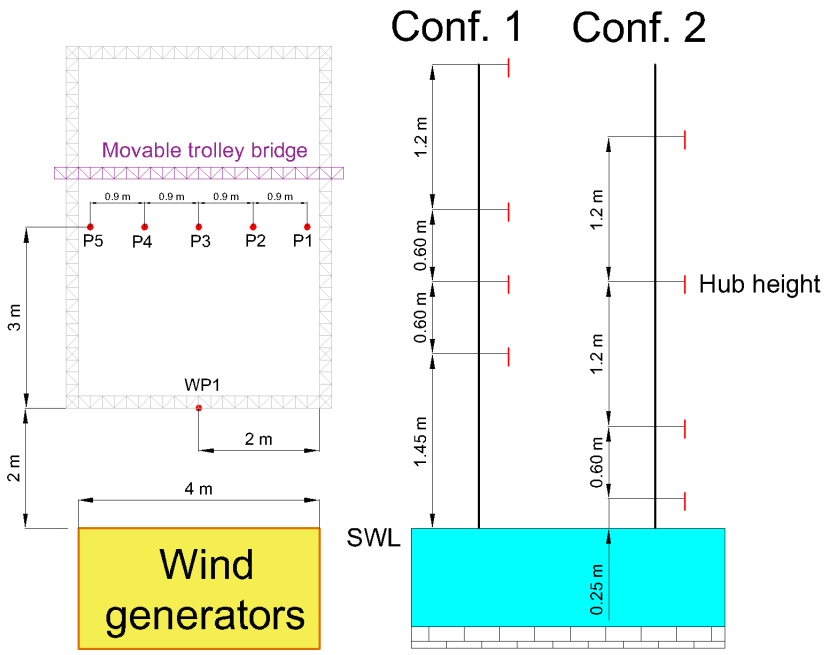

Figure 5.1: Schematic of the different wind probe configurations.

Before the wind field was measured, the relationship between wind speed and fan RPM of the wind generator must be established. The wind generator speed was set to values from 100 RPM to the maximum value of 1800 RPM and the corresponding 1-minute average wind speed at hub height in the rotor plane was recorded. Figure 5.2 shows the measured data points and the resulting linear fit describing the relationship between the wind generator fan RPM ω_{gen} and the wind speed at hub height V_{hub} (see Eq. 5.1). Table 5.1 lists the required fan RPM for all ECs.

$$V_{hub} = 0.0012\,\omega_{Gen} - 0.0319\,\frac{m}{s} \tag{5.1}$$

Table 5.1: Required wind generator fan RPM for different environmental conditions.

	2021			**2017**		
EC	A	B	C, D, E	3	5	6, 11
$\omega_{\mathbf{gen}}$ **[RPM]**	902	1235	1800	943	1277	1800

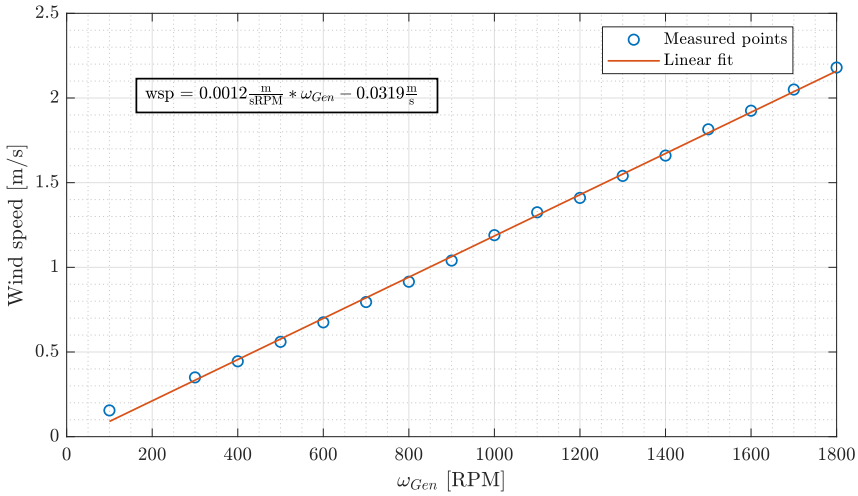

Figure 5.2: Calibration curve for wind generator.

After obtaining the fan RPM - wind speed relationship, the wind field was measured for four different mean wind speeds: 1.03 m/s, 1.47 m/s, 1.94 m/s and 2.2 m/s. These values correspond to wind speeds below rated, at rated, above rated and the maximum wind speed. The corresponding fan RPM values were obtained using Eq. 5.1. The pole with the wind probes was swept across the rotor plane in both configurations for each RPM setting. At each position, the wind speed was measured for 4 min. Based on the mean wind speed $\bar{V}$, the turbulence intensity TI is calculated as followed:

$$TI = \frac{\sigma}{\bar{V}} \tag{5.2}$$

where σ is the standard deviation of the wind speed.

Figure 5.3 displays the measured mean wind speed and turbulence intensity for the entire covered rotor plane for each target wind speed. The left pane shows the mean wind speed and the right pane the turbulence intensity. The plot is looking downwind and the black circle indicates the swept rotor area of the turbine. The wind speed values in the subplot titles indicate the target mean wind speed at hub height, which was used to set the fan RPM.

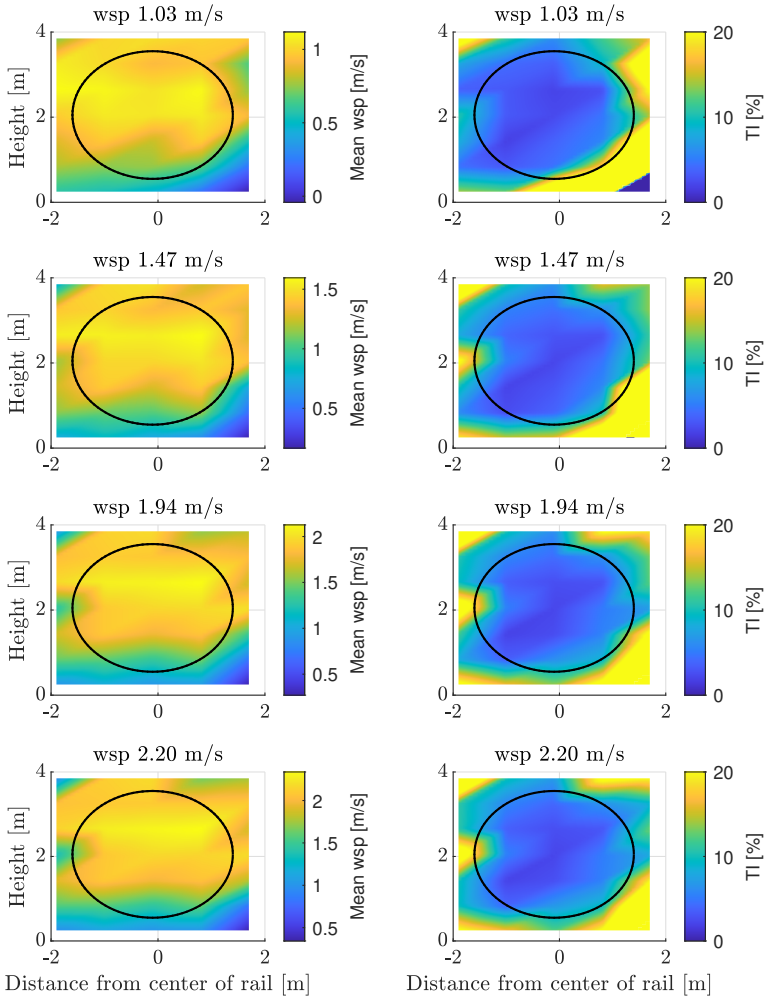

Figure 5.3: Mean wind speed and turbulence intensity in the rotor area for different mean winds at hub height. Plot is looking downwind, rotor area is indicated by black circle.

The mean wind speed is close to the target values for most of the measured area. Only in the lower part is the wind speed significantly lower than the target value at hub height. This is due to the wind generator ending at a height of 64 cm above MWL, meaning that the lower parts of the area are not covered by the wind generator. Additionally, the trolley bridge at a height of approximately 1 m also influences the wind flow due to a shadow effect. For higher wind speeds, there also seems to be a small area with reduced wind speed on the left edge of the measured area.

The turbulence intensity is at low values of around 3% for most parts of the rotor plane. Only the bottom right corner shows a significantly higher turbulence intensity, probably due to the influence of the main bridge from which the wind generator, wave maker and wind turbine are operated (see Figure 4.8). This area, however, does not include the swept rotor area and should therefore not affect the experiments. Within the limitations of the wind generator, the obtained wind field results are considered satisfactory.

5.1.2 Wave Calibration

In this section the wave climates are validated and compared to the target climates. Both irregular and regular sea states are discussed.

Irregular Waves

First, the 2021 experimental campaign irregular sea states were calibrated. In a first run, each sea state was created using the wave paddle in the wave basin and the surface elevation was measured by the various wave gauges. Afterwards, the wave data was analyzed and the significant wave height and peak period of the wave spectrum were obtained. By using the series of the five gauges WG1 to WG5 the incoming and reflected wave spectrum were obtained, as well as the reflection coefficient K_r. The incoming and reflected wave fiels, as well as the reflection coefficient K_r, were calculated by using a MATLAB function that was kindly provided by the hydraulic engineer Bjarne Jensen from DHI. The function is based on a method proposed in [64], which divides a one-dimensional wave field into left and right-travelling components using an arbitrary number of wave gauges. Based on the measured incoming significant wave height $H_{s,meas}$ and the target wave height $H_{s,tar}$, an amplification factor A was calculated as followed:

$$A = \frac{H_{s,tar} - H_{s,meas}}{H_{s,tar}} + 1 \tag{5.3}$$

The obtained amplification factor was then applied in a second run and the sea state was again documented in regards to significant wave height, peak period and reflection coefficient. The amplification factor applied in this second run was also the amplification factor applied in the following tests. Table 5.2 shows the final results without wave misalignment and Table 5.3 the results with 30° wave misalignment. Both tables show the measured incoming wave height and peak period, as well as the reflection coefficient. In general, the results show a good match of the measured sea states with the target sea states. Only for sea states EC A.1 and EC B.2, the measured wave height deviates more than 10% from the target value. However, it should be considered that these sea states have very small wave heights at lab-scale, which means that there is only a small deviation in absolute values. The deviation

of the peak periods is also relatively small, with values below 5% except for EC D.1, which shows a deviation of 8%.

Table 5.2: Significant wave height, peak period and reflection coefficient for the 2021 experimental campaign irregular sea states with 0° misalignment.

		EC A.1	**EC B.1**	**EC C.1**	**EC D.1**	**EC E.1**
Hs [m]	Target	0.0227	0.0370	0.0840	0.1957	0.2223
	Measured	0.0197	0.0341	0.0831	0.1964	0.2045
	Deviation [%]	**13.09**	**7.84**	**1.07**	**0.37**	**8.01**
Tp [s]	Target	0.7346	0.8417	1.1606	2.1792	2.1
	Measured	0.7389	0.8260	1.1111	2.0056	2.0037
	Deviation [%]	**0.59**	**1.87**	**4.27**	**7.97**	**4.59**
Kr [%]	Measured	20.2	13.21	9.2	10.95	10.64

Table 5.3: Significant wave height, peak period and reflection coefficient for the 2021 experimental campaign irregular sea states with 30° misalignment.

		EC B.2	**EC C.2**	**EC D.2**
Hs [m]	Target	0.0370	0.0840	0.1957
	Measured	0.0317	0.0872	0.1918
	Deviation [%]	**14.32**	**3.81**	**1.98**
Tp [s]	Target	0.8417	1.1606	2.1792
	Measured	0.8009	1.1177	2.2407
	Deviation [%]	**4.85**	**3.70**	**2.82**
Kr [%]	Measured	12.69	12.88	16.39

Figure 5.4 shows the full wave spectra of the 2021 experimental campaign sea states with no misalignment and Figure 5.5 shows the spectra with 30° misalignment. For each sea state, 3 different spectra are displayed: the target spectrum, the incoming spectrum obtained by WG1 to WG5 and the total spectrum obtained by WG10 at the turbine position. Because the raw spectra showed many spikes, a moving average filter was applied to smooth the spectra.

In general, there is a good agreement between the measured spectra and the target spectra. The total spectra is always slightly higher than the target spectra, as it also

contains the reflected wave field. The incoming spectra are quite close to the target spectra. The spectrum of EC A.1 shows an unusual peak at 0.75 Hz, which does not occur in any other wave spectrum and also did not occur in the first run of EC A.1. It is therefore assumed that this peak was caused by some external disturbances. EC A.1 has a very low significant wave height of 2.3 cm, and is thereby susceptible to any kind of disturbance. During the second run of EC A.1, construction works were carried out in the hall next to the wave basin, which might have caused some low frequency noise in wave spectrum.

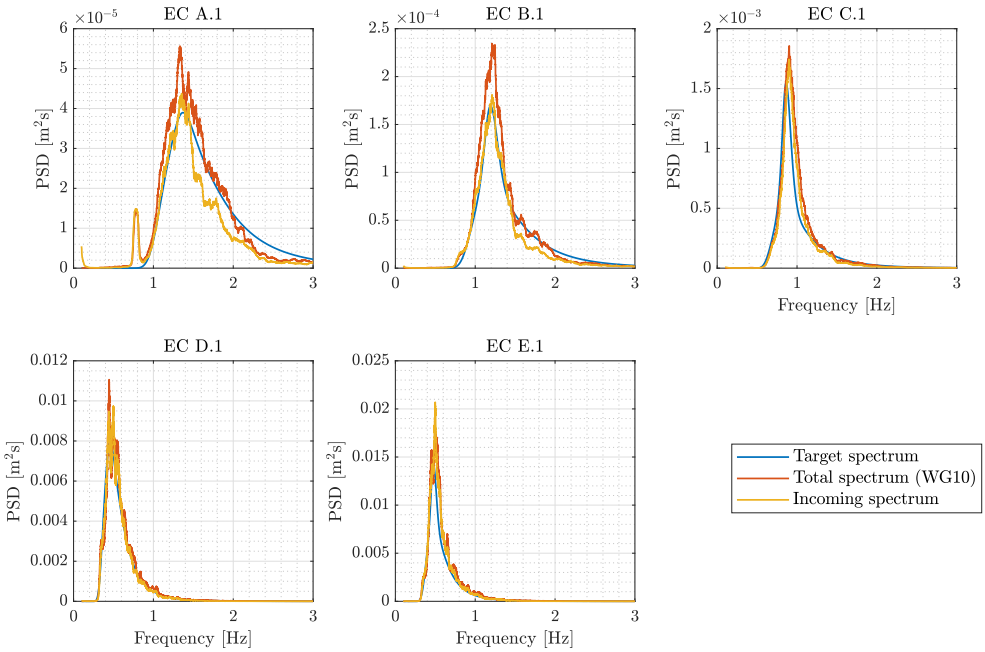

Figure 5.4: Target, measured incoming and measured total wave spectra for the 2021 experimental campaign sea states with 0° misalignment.

In the wave spectra for the sea states with 30° misalignment there is a cut-off in the energy content above 1.5 Hz. This is caused by a limitation of the wave paddles when creating the misaligned wave field. In order to change the direction of the waves, the wave paddles move in a sinusoidal way. The maximum frequency at which the wave paddle form this motion seems to be around 1.5 Hz, which means that no misaligned waves above this frequency can be created. Nevertheless, the energy content above this frequency is very low, especially for larger sea states. Therefore, this limitation is considered as not problematic.

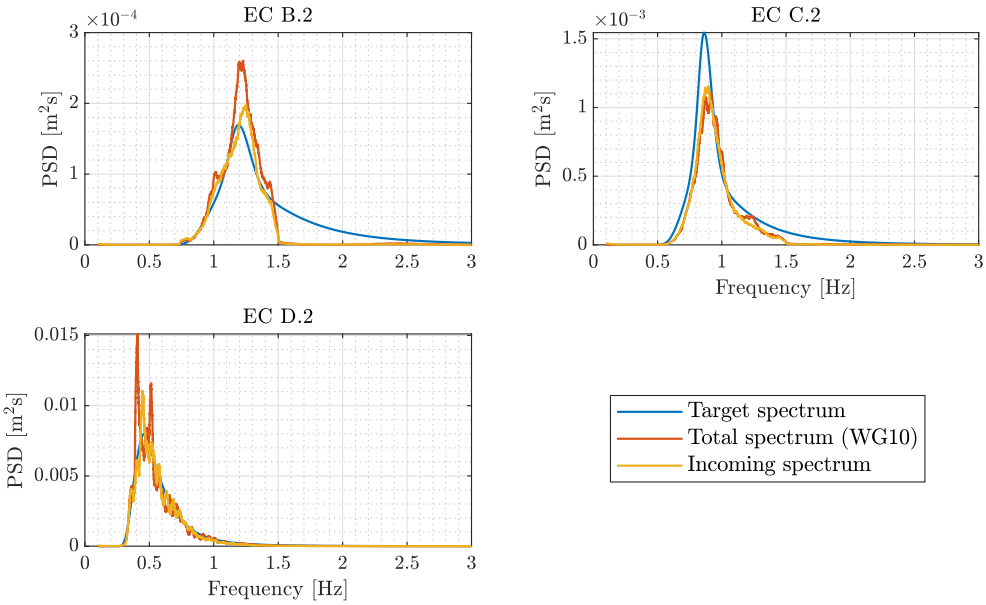

Figure 5.5: Target, measured incoming and measured total wave spectra for the 2021 experimental campaign sea states with 30° misalignment.

Table 5.4: Significant wave height, peak period and reflection coefficient for irregular sea states of the 2017 measurement campaign.

	2017 Campaign:	**EC 3**	**EC 5**	**EC 6**	**EC 11**
Hs [m]	Target	0.055	0.069	0.103	0.175
	Measured	0.0515	0.0669	0.1028	0.1724
	Deviation [%]	**6.36**	**3.04**	**0.19**	**1.49**
Tp [s]	Target	0.839	0.9420	1.149	1.833
	Measured	0.8499	0.8767	1.1111	1.7045
	Deviation [%]	**1.30**	**6.93**	**3.3**	**7.01**
Kr [%]	Measured	14.69	12.87	11.82	9.98

The 2017 experimental campaign sea states had already been calibrated in a previous test campaign and the corresponding control signals for the wave paddles stored. Thus, these sea states were not calibrated, but only documented by running the corresponding control signals and measuring the resulting wave spectra. Table 5.4 shows the measured significant wave height and peak period of the incident wave spectrum

and the reflection coefficient. The measured values match very well the target values with all deviations below 10%. Figure 5.6 shows the corresponding wave spectra. Again, 3 different spectra are displayed for each sea state: the incident spectra based on WG1 to WG5, the total wave spectrum measured by WG10 and the target spectrum. The shape of the measured spectra is slightly different from the target spectra, with higher energy content around the peak frequency and lower content at higher frequencies. The total energy content however is very similar to the target spectra, as can be seen in the significant wave heights.

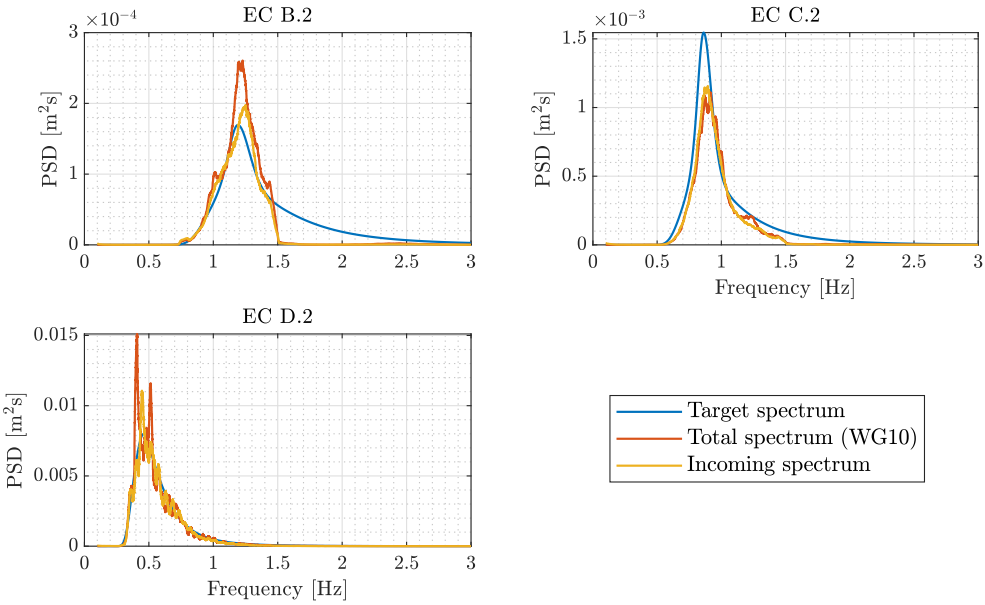

Figure 5.6: Target, measured incoming and measured total wave spectra for 0° for the different ECs of the 2017 experimental campaign.

Regular Waves

The regular sea states of the 2021 experimental campaign consist of 5 different wave periods with 2 different wave heights. All regular waves were run once with an amplification factor of 1 and the measured wave height and period were documented. WG10 at the turbine position was used as measurement. Table 5.5 shows the measured wave height and period compared to the target values and Figure 5.7 displays the time-series of the measured waves compared to the target waves. The measured periods are almost identical to the target periods. The wave heights also show a good match, except for higher waves, where the generated waves tend to be too high.

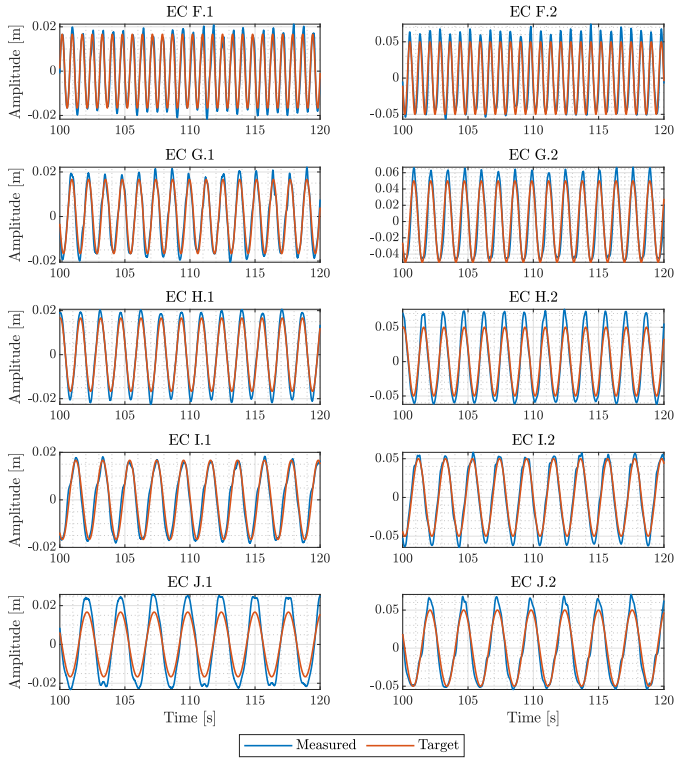

Figure 5.7: Time-series of the measured and target regular waves of the 2021 experimental campaign regular sea states.

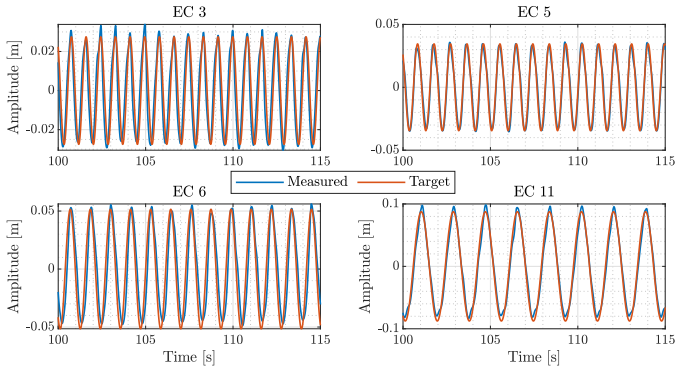

Figure 5.8: Time-series of the measured and target regular waves of the 2017 experimental campaign regular sea states.

Similarly to the irregular sea states of the 2017 experimental campaign sea states, pre-calibrated control signals were also available for the regular sea states. These control signals were run once and the wave height and wave period were measured. Table 5.6 lists the results obtained by WG10 at turbine position and Figure 5.8 shows the corresponding time-series, again compared to the target values. The results show a good match for both the wave height and wave period.

Table 5.5: Wave height and period for 2021 experimental campaign regular sea states.

Configuration 1		**EC F.1**	**EC G.1**	**EC H.1**	**EC I.1**	**EC J.1**
H [m]	Target	0.0333	0.0333	0.0333	0.0333	0.0333
	Measured	0.0385	0.0356	0.0388	0.0335	0.049
	Deviation [%]	**15.62**	**6.91**	**16.52**	**0.60**	**47.15**
T [s]	Target	0.77	1.29	1.55	2.07	2.58
	Measured	0.7692	1.2903	1.5484	2.0690	2.5806
	Deviation [%]	**0.10**	**0.02**	**0.10**	**0.05**	**0.02**
Configuration 2		**EC F.2**	**EC G.2**	**EC H.2**	**EC I.2**	**EC J.2**
H [m]	Target	0.10	0.10	0.10	0.10	0.10
	Measured	0.1067	0.1105	0.1313	0.1121	0.1151
	Deviation [%]	**6.70**	**10.50**	**31.30**	**12.10**	**15.10**
T [s]	Target	0.77	1.29	1.55	2.07	2.58
	Measured	0.7692	1.2903	1.5484	2.0690	2.5806
	Deviation [%]	**0.10**	**0.02**	**0.1**	**0.05**	**0.02**

Table 5.6: Wave height and period for 2017 regular sea states.

2017 Campaign		**EC 3**	**EC 5**	**EC 6**	**EC 11**
Hs [m]	Target	0.055	0.069	0.1030	0.1750
	Measured	0.0574	0.0688	0.0973	0.1666
	Deviation [%]	**4.36**	**0.29**	**5.53**	**4.8**
Tp [s]	Target	0.8390	0.9420	1.15	1.833
	Measured	0.8421	0.9412	1.1429	1.8182
	Deviation [%]	**0.37**	**0.08**	**0.62**	**0.81**

5.2 Rotor ID

As mentioned previously, the turbine model was scaled in order to preserve the Froude number, which results in a different Reynolds number and therefore a different mean thrust force than the purely downscaled one. As explained in Section 4.1.1, the blades were redesigned in order to better match the thrust curve. However, the thrust curve still does not match perfectly the downscaled thrust curve of the full-scale model. This is also due to small deviations in the manual mounting procedure of the blades on the turbine, which are difficult to avoid. For this reason, a rotor ID was carried out.

For carrying out the rotor ID, the wind turbine was placed on a fixed platform attached to the rail bridge at a height that matched the hub height when the turbine was placed on the floater. The wind speed was set to a range of values both below and above rated wind speed and the pitch angle θ was adjusted until the measured thrust of the model matched the desired scaled thrust according to the DTU 10 MW RWT report [54] and the scaling laws presented in Section 4.1.1. Figure 5.9 shows the measured thrust forces and blade pitch angles compared to the reference values. To obtain the sensitivity to a change in blade pitch angle, the thrust values for blade pitch angles +/- 1° were also recorded. The corresponding thrust values are shown in Figure 5.9 in black circles and squares, respectively.

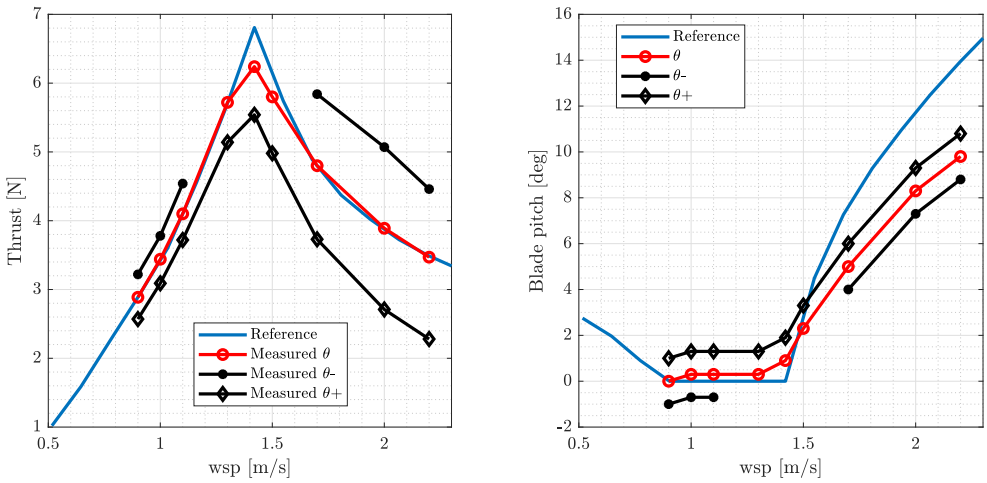

Figure 5.9: Rotor ID test for rotor thrust and blade pitch angle. Measured values in red circles, values obtained for blade pitch angles of +/- 1° are shown in black squares and circles, respectively.

It was not possible to obtain the desired thrust values around rated wind speed because the maximum generator torque was exceeded and the turbine therefore shut down. This is a surprising result, as in previous test campaigns, using the same

turbine model, the desired thrust could be achieved. It is suspected that the friction in the generator gears was higher than in the 2017 campaign, which lead to a higher torque for the same thrust value. Moreover, small deviations in the mounting of the blades on the turbine could also cause a different rotor ID than in previous campaigns. At wind speeds at which the reference thrust could not be achieved, the sensitivity analysis for -1° could naturally not be carried out, as a smaller pitch angle would result in even higher thrust, and eventually higher generator torque. Figure 5.10 shows the results for the thrust and the corresponding blade pitch angles for both the presented 2021 test campaign and the 2017 TLP campaign [62]. The blade pitch angles in the current test campaign are smaller than the ones obtained in the 2017 campaign. There seems to be a constant offset between both campaigns, which indicates that there was indeed a difference in the initial manual mounting process of the blades. Another potential issue that could explain the rotor ID deviations is the difference in the ambient temperature between both campaigns, which affects the air density. While the 2017 experimental campaign was mainly conducted in the summer, the 2021 experimental campaign was conducted in the spring under considerably lower ambient temperatures.

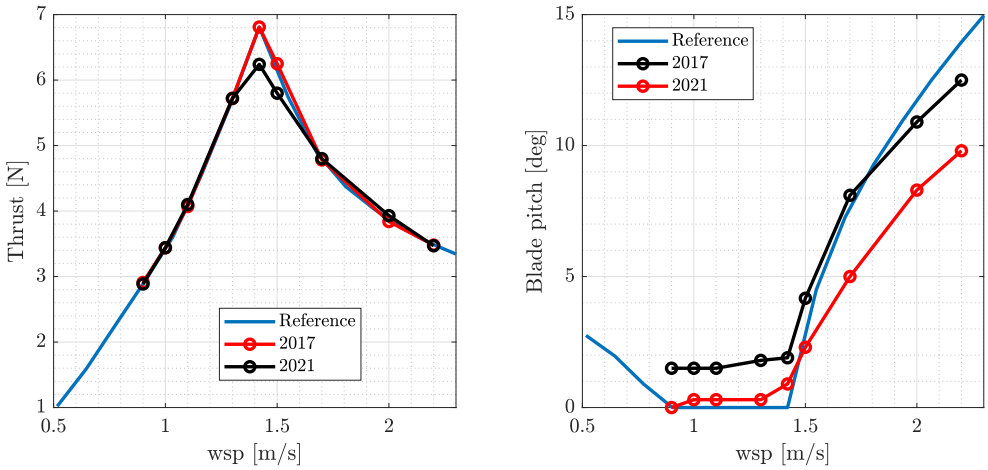

Figure 5.10: Rotor ID comparison with the previous 2017 experimental campaign [62].

After finishing the rotor ID tests, additional lubricant was applied to the generator gears. However, due to time constraints in the lab, it was decided not to repeat the rotor ID tests with the additional lubricant.

5.3 Decay tests

For the purpose of finding out the dynamic properties of the floating wind turbine, several decay tests with varying amplitudes were performed for the 6 DoFs of the floater. An initial displacement was imposed to the structure after which it was released back to the equilibrium position. Measuring the decay allows to determine both the natural frequencies and the damping ratios of the floater. These tests were carried out by attaching a rope to different points of the model. For the surge and sway decay tests, the rope was attached to the tower bottom and the model was pulled from the respective directions. For the heave decay tests, the model was manually pushed from the nacelle towards the water. For the roll and pitch decay tests, one rope was attached to the tower-top of the model and the rope was pulled from the respective directions. Lastly, in the case of the yaw decay tests, two ropes were attached to the fair leads of the back columns of the floater, while one person pulled from one direction, the other person pulled from the other one. Note that these decay tests were carried out with the second and final mooring line configuration explained in Section 4.1.3.

For each DoF, several free decay tests were carried out consecutively. Due to the asymmetry of the floater and the resulting strong coupling between the degrees of freedom, it was not possible to completely isolate an initial displacement in the desired DoF without inducing a certain initial displacement in some of the other DoFs. This was especially the case for the yaw and sway motion, for which no clean decay could be achieved. Table 5.7 shows the identified natural frequencies and damping ratios after having analyzed the logged time-series for every decay test. The displayed natural frequencies are the average value of each decay test in the respective DoF. It is interesting to note that the natural pitch frequency is significantly lower than the natural surge frequency.

The damping ratio ζ of each DoF is calculated based on the logarithmic decrement δ, which can be obtained from the measured decay time-series:

$$\delta = \ln\Big(\frac{a_j}{a_{j+n}}\Big) = \frac{2\,\pi\,n\,\zeta}{\sqrt{1-\zeta^2}} \tag{5.4}$$

where a_j is the amplitude at point j and a_{j+n} the amplitude n oscillations later. Table 5.7 lists the damping ratios calculated based on the measured decays. However, it is difficult to determine the damping ratios exactly, especially for strongly damped DoFs. The definition of the logarithmic decrement assumes that the ratio between any two maximum values in a decay is constant, which is not the case for many of the measured decays. The displayed damping ratios should therefore be considered as rough approximations. Nonetheless, the results show the expected strong damping of the heave motion due to the heave plates.

Table 5.7: Results from the model decay tests.

Model decay test						
Parameters	Surge	Sway	Heave	Roll	Pitch	Yaw
Damped natural frequency [Hz]	0.36	0.28	0.5	0.22	0.15	0.29
Damping ratio [-]	0.054	0.039	0.16	0.094	0.06	0.16

As aforementioned in Section 4.1.3, the mooring line system had to be readjusted to avoid both surge and heave natural frequencies coinciding with the peaks of the extreme sea states, triggering a resonance state. However, this change only reduced the surge natural frequency, shifting it towards lower natural frequencies, but the heave natural frequency was not modified considerably. For the different sea states reproduced during the experimental campaign, the heave natural frequency coincided with the peak period of the extreme sea states: EC D and EC E of the 2021 experimental campaign sea states and EC 11 from the 2017 experimental campaign (see Figure 5.11). Since the heave plates typically dampen out the motion significantly, a potential heave resonance was considered as acceptable.

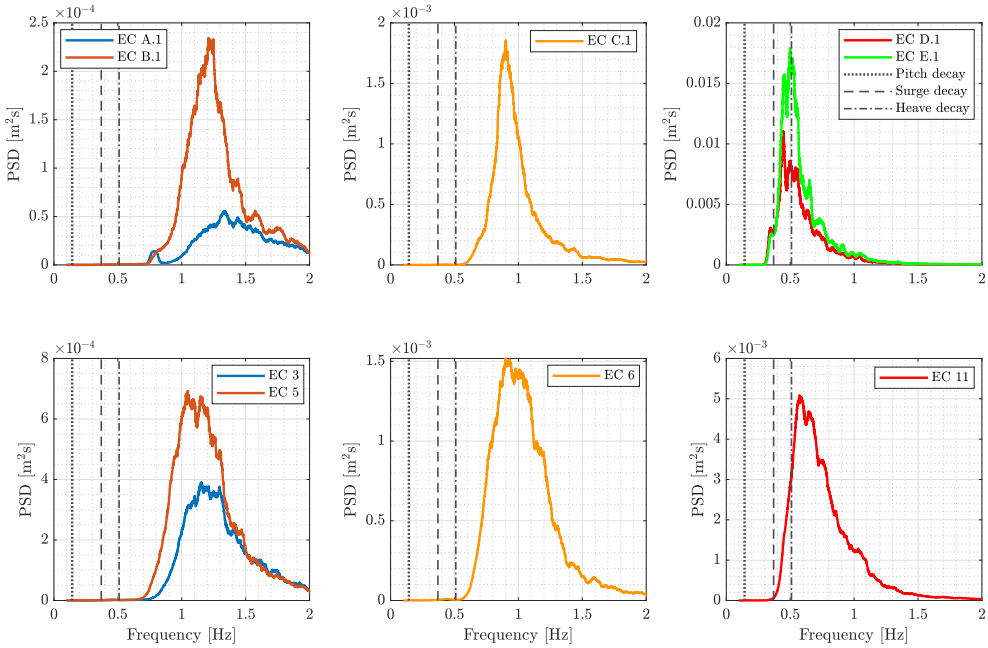

Figure 5.11: Main floater natural frequencies together with the wave spectra of the different sea states.

5.4 Lab controller tuning

In this section the procedure for finding the parameters of both the detuned baseline controller and the new tower-top loop controller is presented. Robustness constraints and performance criteria for the design of the controllers are mentioned. Results for different detuned controllers are shown, eventually leading to the chosen baseline detuned controller. The same is done for the new tower-top loop control strategy.

5.4.1 Baseline detuned controller

In order to tune the controller for the 1:60 DTU-TetraSub Wind Turbine model, a HAWCStab2 model of the 1:60 DTU 10MW RWT was run considering some initial parameters taken from the slow offshore controller designed by researcher M. Mirzaei for the 2017 campaign [53, 52], which is based on the Basic DTU Wind Energy Controller [17]. After this simulation was run, some fix parameters were determined (see Table D.1 in the Appendix D).

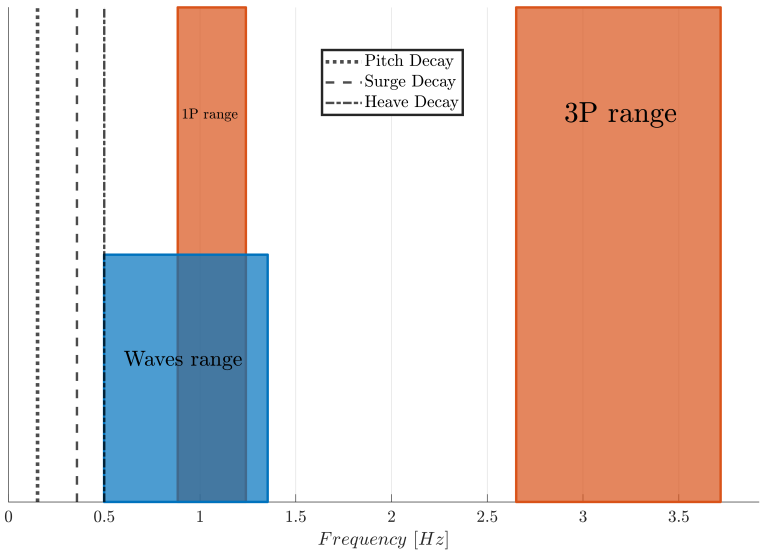

Figure 5.12: Natural frequencies from the main relevant 3 DoFs and excitation frequencies of the rotational speed of the rotor as well as the waves.

Before the controller tuning procedure is explained in detail, it is important to highlight that an important factor to consider when designing a wind turbine controller is to ensure that the excitation frequencies do not coincide with the natural frequencies of the structure itself. Floating wind turbines are not only affected by

the 1P and 3P frequencies from the rotating blades, but also by the waves acting on the structure. If the excitation frequencies of the external loads acting on the structure coincide with the natural frequencies of the structure, the structure experiences resonance, which can lead to increased fatigue loads or even structural failure if the vibrations are not properly damped. With an operational range of ω = [53.02-74.37] rpm, a wave frequency climate range of f_{wave} = [0.49-1.35] Hz and natural frequencies determined in Section 6.3, the most relevant excitation frequencies can be sketched as shown in Figure 5.12. Note how the heave natural frequency is within the wave frequency range, however the heave plates typically dampen out the motion significantly, so no excessive heave motion is expected.

As commented in Section 2.2.1.2, there exist two different variations of full load control strategy, constant torque and constant power. In the same way as in the previous 2017 experimental campaign, the chosen full load control strategy was constant torque. At this point, the objective was to find the fastest robust controller without enabling the new tower-top velocity loop, which does not trigger the pitch instability above rated. For this purpose, several basic controllers with different closed-loop frequencies up to 0.4 Hz were tuned in HAWCStab2, resulting in different parameters K_i and K_p above rated. In order to test the performance of the different controllers, the same step wind test was run for every controller with varying wind speeds [1.2-2.2] m/s. The different wind speeds were kept for a minute, unless the model was really unstable above rated, having to carry out an emergency shutdown. The performance of the controller below rated was basically the same regardless of the controller tested. As a result of this, the main interest lies in the region around rated and above rated, where the instability is most likely to occur due to the negative gradient of the thrust force being the highest in this region (see Section 2.2.2).

Figure 5.13 shows the performance of different controllers under these step wind tests. The procedure for carrying out the step wind tests was always the same, but since the wind speed is a stochastic phenomenon including turbulence, there were some slight differences in the wind speed at hub height. Also note that the wind speed shown is the result of applying a correction factor to the signal coming from the wind probe (WP1) that was placed at hub height right in front of the wind maker (see Figure 5.1), and hence the wind speed at the rotor area was slightly lower. The black dotted horizontal lines stand for the rated wind speed (v_{rated} = 1.47 m/s) and rated rotor speed (ω_{rated} = 74.36 RPM) of the small-scale model wind turbine, respectively. The only difference between the four different controllers used for these tests was the chosen closed-loop frequency, and consequently the different parameters K_i and K_p above rated (see Table D.2 in the Appendix D). In total, four different wind steps are depicted for the four different controllers. The first wind step corresponds to a wind speed below rated, and hence all the controllers behave in the same way keeping the blade pitch angle at its minimum. The following wind step corresponds to a transition area between below and above rated leading to different behaviours of the controllers depending on how fast they are. Even though the floater pitch signal was not logged for these tests, it is in this wind step where the pitch instability started being noticeable for the fast controllers due to the experienced negative aerodynamic

damping explained in Section 2.2.2. The following wind step is just above rated where the pitch instability should be the maximum one. The same does not happen for the blade pitch, since the blade pitch needs to be higher for higher wind speeds in order to keep the torque constant, and hence the amplitude will increase together with the wind steps, however limited by the minimum pitch angle.

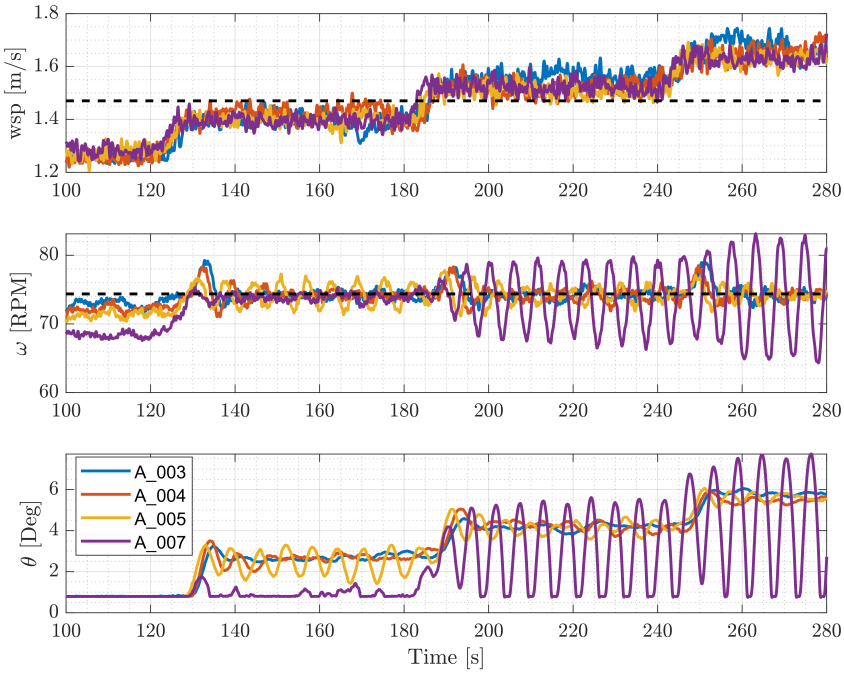

Figure 5.13: Wind turbine operational parameters performance under the wind step tests for different controllers.

Now it is time to analyze the performance of the different controllers one by one. The first of them is the controller A_003, which was the fastest conventional controller that was stable above rated. A closed-loop frequency of 0.15 Hz was used to calculate the parameters K_p and K_i above rated. It is clear that it is the most stable controller since the blade pitch is mainly kept constant for every wind step since the pitch instability is not triggered. However, the overshoots of the rotor speed seem to be the highest ones even though this parameter also depends on the wind speed turbulence, and hence no statistical data have been analyzed. For a better statistical analysis, being able to reproduce exactly the same wind speed or running the same test several times would have been interesting. As the objective has been reached, this controller will be referred as the **baseline controller** from now on. However,

the chosen closed-loop frequency, which is defined as the new natural frequency of the whole system once the controller is enabled, coincides with the pitch natural frequency. As aforementioned in Section 4.2, the HAWCStab2 model is based on an onshore turbine model, therefore the defined natural controller frequency does not exactly correspond to the pitch natural frequency.

Controller *A*_004 was tuned for a closed-loop frequency of 0.2 Hz. It presents exactly the same behaviour as the baseline controller, however in the above rated regions some instability could be observed in the floater pitch, and then confirmed by the blade pitch angle signal. It can be said that this controller is in a transition point between being stable and unstable. This can be confirmed by the controller *A*_005, which was tuned for a closed-loop frequency of 0.25 Hz and is obviously unstable because it is able to respond faster to changes as seen in the rated transition window leading to large oscillations in the rotor speed. Lastly, controller *A*_007 was tuned for a closed-loop frequency of 0.35 Hz leading to a large instability, eventually resulting in an emergency shutdown of the wind turbine.

5.4.2 Tower-top velocity loop

The objective of this section is tuning the new controller, in other words, finding the K_{tt} value that when the tower-top velocity loop is enabled allows to stabilize a previously unstable controller, and hence reducing the dynamic response of the faster controller leading to a performance similar to the baseline controller, while being able to react faster to changes in the wind speed. The chosen controller, the **tower-top loop controller** will be the fastest controller that can cope with the pitch instability within an acceptable range.

The procedure for tuning the new controller was running the baseline unstable controllers with different K_{tt} gains until the controller became stable. For triggering the pitch instability, only one wind speed was needed, this wind speed was 1.67 m/s, which is the most critical operating point where the pitch instability is maximum. This critical wind speed was reached at time T = 60 s, after which the pitch instability appears. Exactly 30 seconds later, at T = 90 s, the tower-top velocity loop was enabled. From that moment, either the chosen gain was insufficient and the system became more unstable having to shut down the turbine, or the gain helped in reducing the instability. The logical tuning order was to find the K_{tt} values from less unstable controllers to the most unstable ones. The new controller was proven to be stable for the unstable baseline controllers, meaning those controllers tuned for closed-loop frequencies of 0.2, 0.25 and 0.3 Hz.

Figure 5.14 shows the performance of different controllers with different K_{tt} gains tuned with a closed-loop frequency of 0.35 Hz, which was the most unstable controller shown in Section 5.4.1. Three different controllers are depicted to demonstrate the importance of choosing the right gain. Controllers *D*_002, *D*_008 and *D*_015 correspond to the starting point with the lowest gain, the fine-tuned gain and the highest gain, respectively (see Table D.3 in the Appendix D). The three controllers have an

identical unstable behaviour until the tower-top loop is enabled, as it could be expected. In comparison with the previous analysis, more signals have been included. The commanded blade pitch is the contribution to the total blade pitch angle change coming from the tower-top velocity loop, or in other words, the product of the real-time tower-top velocity by the K_{tt} gain as seen in Eq. 2.42. Other signals such as the wind turbine generator torque, the floater pitch motion, the filtered tower-top fore-aft acceleration and the integrated tower-top fore-aft velocity were included in the post-processing data analysis for a better understanding of the physical behaviour of the model and the controllers.

For the implementation of the new tower-top velocity loop, it is fundamental to obtain this tower-top velocity in real-time. In Section 3.1, two possible methods to obtain the velocity were presented. Due to the very tight schedule of the experimental campaign, only the integration of the tower-top fore-aft acceleration method was tried out.

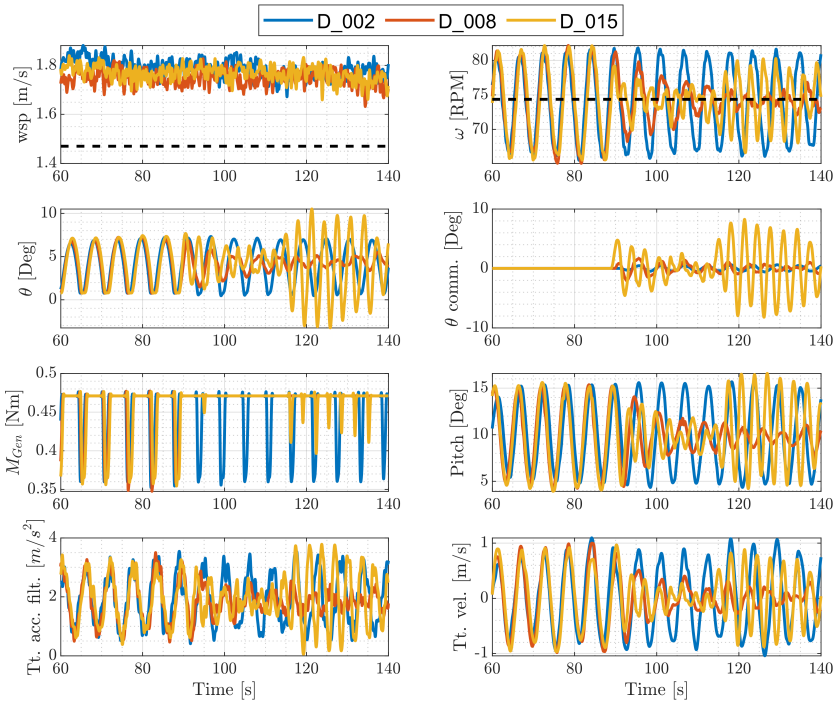

Figure 5.14: Controller performance for three different K_{tt} gain values.

The results for controller D_002 show that the gain is so small that it has barely any effect on the instability of the system. The commanded blade pitch is insignificant,

and consequently the total blade pitch is still highly influenced by the fore-aft motion of the tower. Even though the wind speed is above rated, the relative wind speed seen by the rotor varies periodically below and above rated with the floater pitch rotation, leading to a fluctuation in the generator torque which should be ideally constant. This fluctuation in the generator torque also leads to a fluctuation in the rotor speed as a result of the equation of motion of the rotor speed (see Eq. 2.27). As explained in Section 2.2.2, the turbine experiences negative aerodynamic damping, which can lead to unstable operational conditions.

The results for controller *D_*008 show that the **tower-top loop controller** has been found, as it can bring the system back from an unstable operating point to a stable one. In this case, the commanded blade pitch is more significant resulting in a gradual decrease of the total blade pitch amplitude over time. This damped total blade pitch brought about a constant generator torque causing the rotor speed fluctuation to be damped out over time leading to some minor overshoots mainly caused by wind turbulence or minor floater pitch motions. The floater pitch instability is clearly damped out stabilizing around the mean floater pitch for that wind speed.

The results for controller *D_*015 show that a higher gain leads to a very aggressive control strategy. The controller seems to bring the system back to stability after it has been enabled. However, after some seconds the controller itself seems to trigger the instability again. At some point, the commanded blade pitch signal is too big and it has a large contribution to the total blade pitch angle, leading to the same situation in which negative aerodynamic damping is experienced by the wind turbine.

Note that the positive mean of the accelerometer is due to the mean floater pitch, which causes the accelerometer to also measure a part of the gravitational acceleration. It is also noteworthy that the signals shown in both Figure 5.13 and 5.14 have been filtered. A third order Butterworth low-pass filter was used on all signal outputs with a cut-off frequency of 2 Hz.

After having defined all controller parameters for the different control strategies, the production test could be carried out. The following section will analyze the results of the production tests and the performance of the different controllers in detail.

CHAPTER 6

Results

In this chapter the results of the production tests are analyzed. Before analyzing the test results, the post-processing tools applied to the signals are explained. Then, the results of the wave-only tests are presented and investigated. Afterwards, the wind-only cases are scrutinized and discussed. Likewise, the wind and waves tests are examined in the next section. Finally, the performance of the two controllers of study are assessed and compared to each other.

6.1 Post-processing

Several filters were applied to the raw data from the measurement equipment in order to remove noise, spikes and non-physically high frequency components. First, all of the logged signals were loaded and a piecewise cubic hermite interpolation with the MATLAB *pchip* function was applied in the event of NaN values due to any unexpected mechanical or electrical issues. Then, at least once a day a *Zero run* was conducted between tests. These *Zero runs* consisted of logging the signals with the turbine parked and without wind and waves for one minute. The mean of the logged signals in these tests was used later to subtract it from the production tests except for the three mooring lines that had to preserve their initial pretension values. Afterwards, a 3^{rd}-order low-pass Butterworth filter with a normalized cut-off frequency of two times the cut-off frequency of 10 Hz divided by the sampling frequency of the corresponding signals was implemented. Higher orders could have been used as they would have yielded better off-frequency rejection, but at the expense of a higher computational time. Furthermore, a zero-phase forward and reverse digital Infinite Impulse Response (IRR) filtering was applied to all the signals with a modification of the MATLAB *filtfilt* function. Finally, a moving average filter with 20 leading and lagging points was applied to the PSD plots in order to have a better picture of the frequencies dominating the different time-series.

6.2 Wave-only tests

First the response of the floating wind turbine to wave-only conditions is analyzed. Wave-only conditions imply that the turbine and therefore the controller are not active. The wave conditions tested comprise regular, irregular and focused waves.

Note that the free surface elevation presented in all plots of the results section was measured by WG8, 4 m next to the turbine at the same distance from the wave maker as the turbine (see Figure 4.8). As the floater was located at a distance of 5m from the wave maker, it is assumed that the wind field did not affect the waves.

6.2.1 Response to regular waves

First the response of the floater to regular waves is analyzed. For this purpose the floater was exposed to regular waves with 5 different wave periods: T = [0.77, 1.29, 1.55, 2.07, 2.58] s. For each wave period two different wave heights were tested: H = [0.033, 0.1] m. Each regular wave test had a duration of 5 min. These regular waves correspond to EC F to EC J listed in Table C.1 in Appendix C. Hereafter the time-series of the floater response will be analyzed together with the corresponding power spectral densities (PSD) of the time-series. For calculating the PSD, the first 60 seconds of the time-series are removed as transient.

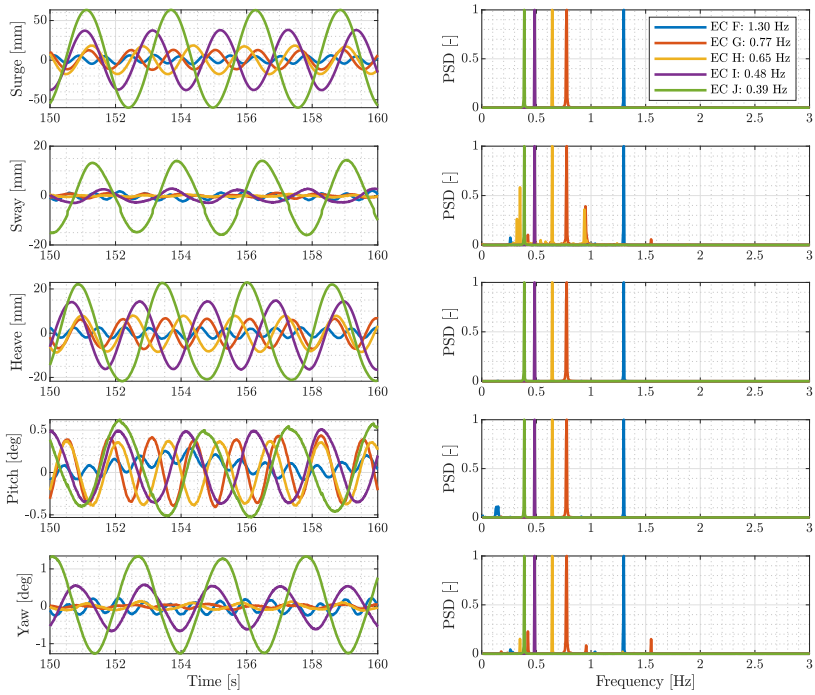

Figure 6.1: 6 DoFs motion of the floater under regular waves with H = 0.033 m, together with the corresponding normalized PSD.

Figure 6.1 shows the 6 DoFs floater motion under all regular waves with wave height H = 0.033 m, as well as the corresponding power spectra. Figure 6.2 displays

the same results for all regular waves with wave height $H = 0.1$ m. The magnitude of the spectral densities are very different for the various cases. In order to be able to display all PSDs in the same figure, the spectral densities are normalized by dividing each of them by the corresponding maximum value. The color code for the wave frequencies is depicted in the legend in the upper right. Looking at the time-series of the floater response to wave heights $H = 0.033$ m, there is a clear trend of lower frequencies resulting in larger floater motion. This can be explained by the lower wave excitation frequencies being closer to the natural frequencies of the floater. This trend is much less pronounced for the pitch motion. Here the response amplitudes are relatively close to each other for wave frequencies from 0.48 Hz to 0.77 Hz. In the case of the sway motion, the response for a frequency of 0.39 Hz is significantly higher than for the other frequencies. A possible explanation is that the wave excitation frequency is relatively close to the natural sway frequency of 0.29 Hz. However, the effect is far less pronounced for the surge motion, which has its natural frequency at 0.35 Hz. It is interesting to note that for a wave frequency of 0.48 Hz, which is very close to the natural heave frequency of 0.5 Hz, no distinct resonance is visible in the floater response. This indicates that the heave plates damp the heave motion significantly.

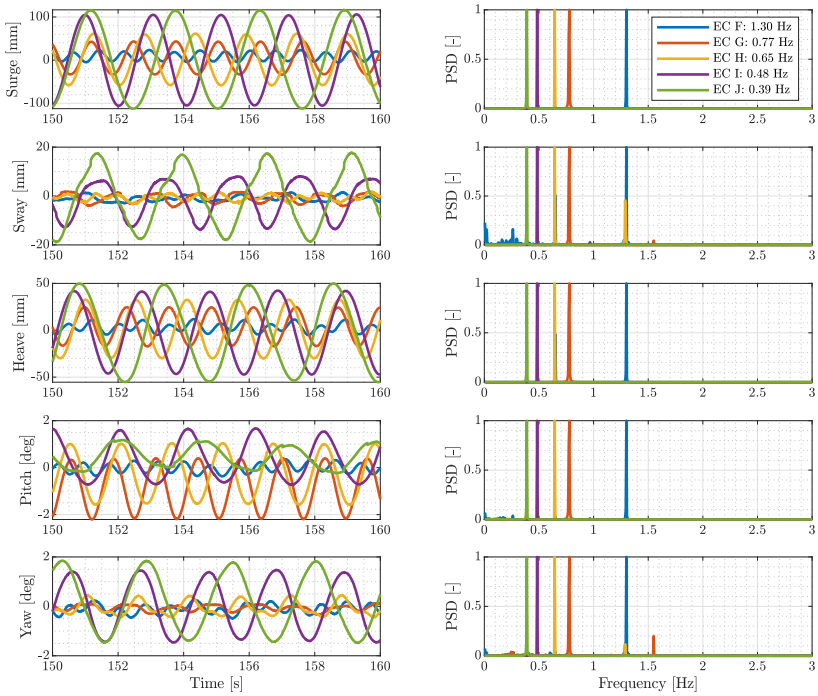

Figure 6.2: 6 DoFs motion of the floater under regular waves with $H = 0.1$ m, together with the corresponding normalized PSD.

The time-series of the floater responses to wave heights $H = 0.1$ m show similar trends as the responses to $H = 0.033$ m. However, the difference in amplitude for different wave frequencies seems to be slightly smaller than for $H = 0.033$ m, especially for the sway motion. For the pitch motion the response for $f = 0.48$ Hz is even higher than for 0.39 Hz. It is also interesting to note that the pitch angle displays a negative offset for $f = 0.77$ Hz, but a positive offset for $f = 0.48$ Hz.

When looking at the power spectra, it can be seen that most of them show one sharp peak at the corresponding wave excitation frequency. This indicates a clear harmonic motion in the respective DoF. Nevertheless, there are some exceptions to this observation. The PSD of the pitch motion for the highest wave frequency of 1.30 Hz and the smaller wave height of 0.033 m shows a small peak at the natural pitch frequency of 0.15 Hz. These low frequency oscillations are also visible in the corresponding time-series. The PSD plots of the sway motion are much less clean than for the other DoFs. Especially for $f = 0.77$ Hz for the small wave height and for $f = 1.30$ Hz for the large wave height several other peaks occur in the PSD. This effect can also be seen in the time-series of the sway motion, which shows a less clean harmonic motion than the other DoFs.

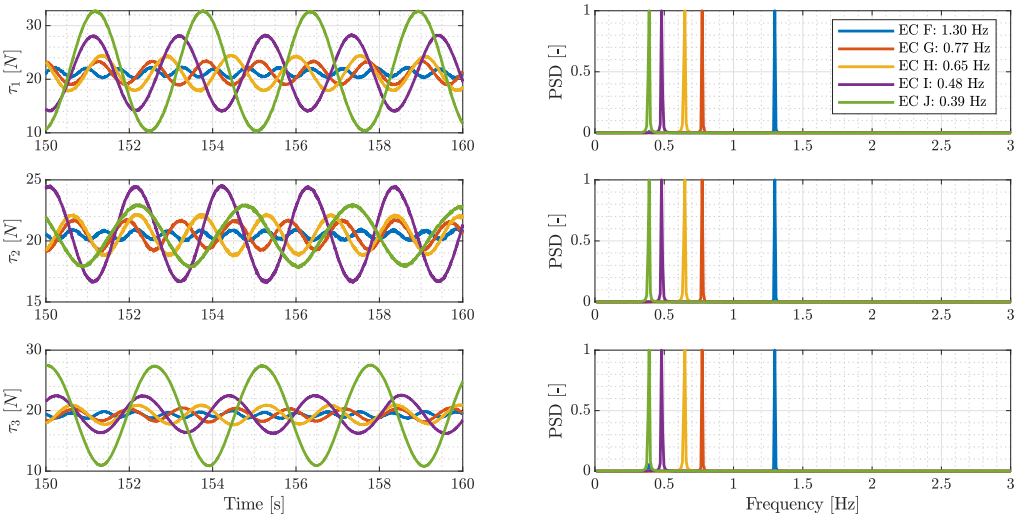

Figure 6.3: Tensions in ML1 (front), ML2 (left) and ML3 (right) for regular waves with $H = 0.033$ m, together with the corresponding normalized PSD.

Next, the same analysis is carried out for the tension in the mooring lines. Figure 6.3 shows the time-series and power spectra of the mooring line tensions for regular waves with $H = 0.033$ m. The PSDs are again normalized to unity and the first 60 seconds are discarded as transient. Figure 6.4 shows the same results for regular waves with $H = 0.1$ m. As for the floater motion, there is a tendency of higher tensions for lower wave excitation frequencies. As the mooring line tensions are directly caused by

the floater motion this is to be expected. The forces oscillate around the pretension of approximately 20 N. It should be noted that the pretension is slightly different for the different mooring lines. An interesting observation is that for a wave frequency of f = 0.48 Hz, the oscillations in the ML2 tensions are significantly higher than for ML3, while for f = 0.39 Hz it is the other way around. This is a surprising observation, as both mooring lines are symmetric and the waves have a 0° inclination angle. Figures 6.1 and 6.2 showed that for f = 0.39 Hz the sway motion is much higher than for 0.48 Hz. Hence it seems that a large sway motion affects ML3 more than ML2. A possible explanation is that the mooring lines are not perfectly symmetric and ML3 is more oriented in sway direction than ML2.

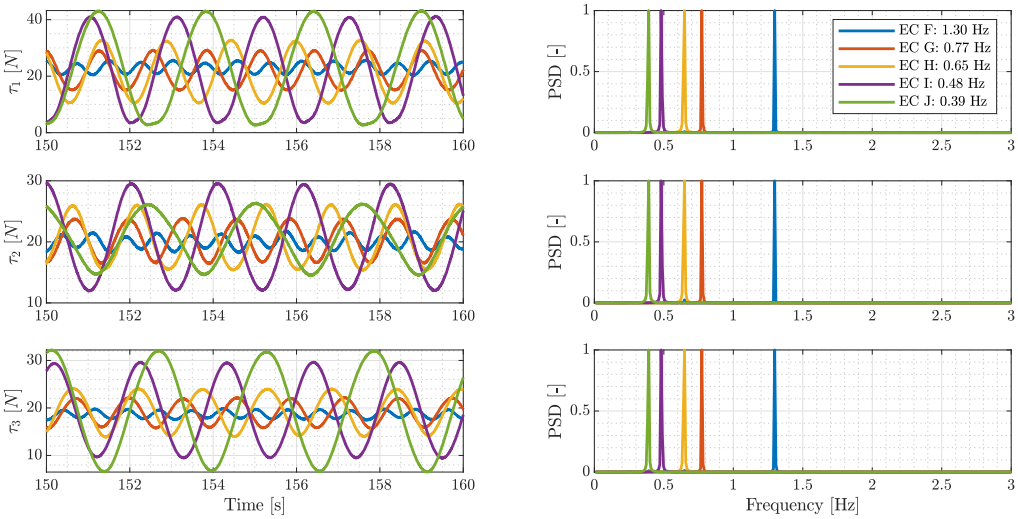

Figure 6.4: Forces in ML1 (front), ML2 (left) and ML3 (right) for regular waves with H = 0.1 m, together with the corresponding normalized PSD.

To investigate a possible misalignment of the mooring lines further, Figure 6.5 displays time-series of the tension in ML2 and ML3 for all regular sea states. As the pretension in the mooring line is slightly different, the mean value is subtracted to allow a better comparison of the dynamic effect on the mooring line tensions. For higher frequencies the amplitudes of the oscillations are very similar, but for some cases ML2 seems to show higher oscillations. For the lowest frequency of 0.39 Hz, ML3 shows a significantly higher response than ML2. These results allow no definite conclusion, but they indicate that ML3 is higher affected by the sway motion than ML2.

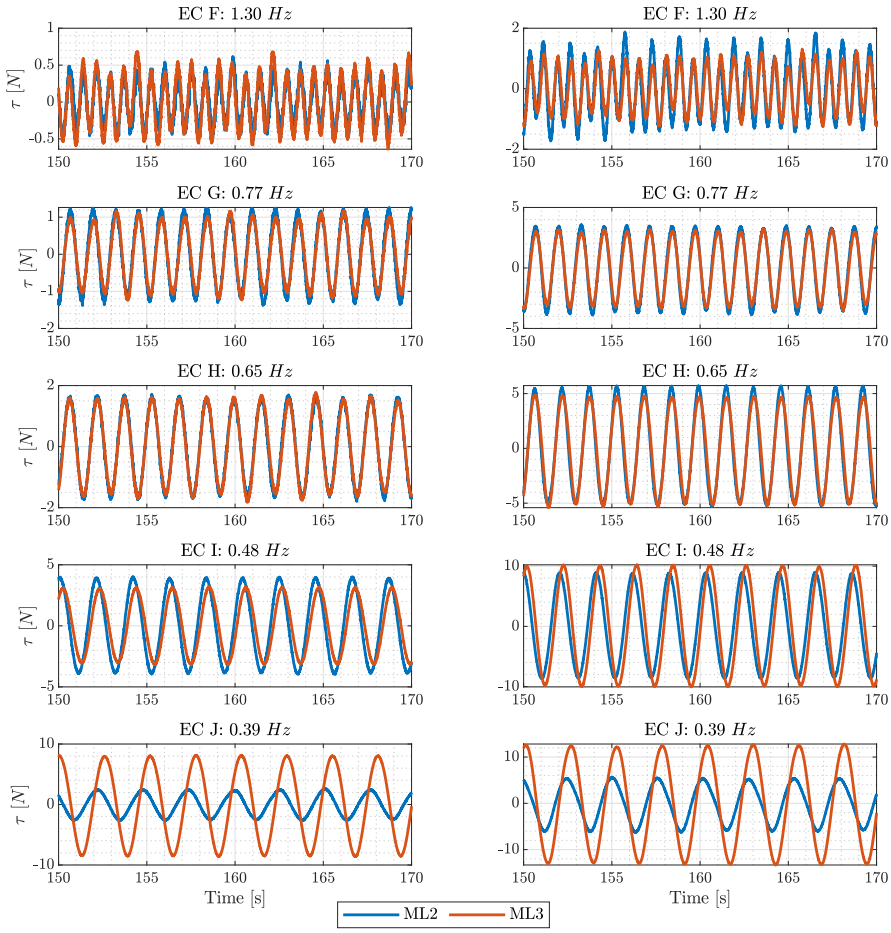

Figure 6.5: Tensions in ML2 and ML3 for all regular waves for wave heights $H = 0.033$ m (left pane) and $H = 0.1$ m (right pane). Mean value is subtracted from the time-series.

6.2.2 Response to irregular waves

As described in Section 2.1.4.2, the irregular waves consist of the aggregation of several waves with different wave heights and periods, hence representing the real-life conditions in a better way than the regular waves. However, it is difficult to compare several time-series for the purpose of data analysis due to its stochastic behaviour. In order to get a better picture of the turbine response, in this project the exceedance probability P is used, which simplifies the comparison of large amount of data:

$$P = p\left(X \geq x_i\right) = 1 - \frac{i}{N+1} \tag{6.1}$$

For each signal the peaks were identified and stored based on a zero-crossing approach implemented as a MATLAB function by H. Bredmose, A. Pegalajar & M.Borg (2016) for use in the LIFE50+ project. The function takes the time-series of the signal and divide it into individual signals, where each signal is defined between two zero-crossings of the original signal. The maximum values of each individual signal are then determined and stored. The peaks are sorted from minimum to maximum and assigned with an index i in order to compute the exceedance probability of each peak based on its index and the total number of peaks *N*. This approach secures the extreme events to be independent [65].

For the analysis, three different irregular sea states from the 2021 ECs set are chosen: EC B (Hs = 3.7 cm, Tp = 0.842 s), EC C (Hs = 8.4 cm, Tp = 1.16 s) and EC D (Hs = 19.57 cm, Tp = 2.18 s) representing a small, medium and extreme sea state. All three sea states were tested in both 0° and 30° misalignment. It should be pointed out that for the extreme sea state EC D, the wave peak frequency of 0.46 Hz is very close to the natural heave frequency of 0.5 Hz.

Figure 6.6 shows the time-series, PSD and probability exceedance of the floater surge, heave and pitch response, as well as the free surface elevation. A 1-minute time window of the entire time-series is also depicted. For calculating the PSD, the first 5 minutes are discarded as transient. Because of the different magnitude of the power spectra, they are normalized such that the maximum spectral density in each spectrum corresponds to unity. The non-normalized power spectra of all presented quantities are shown in Appendix C.2. The natural pitch, surge and heave frequency of the floater obtained in the decay tests are displayed as dotted, dashed and dashed-dotted lines respectively. As expected, the larger sea states result in a larger floater response, as seen in both the time-series and the probability exceedance plots. The frequency spectrum of the surge motion for EC B and EC C has a peak at the natural surge frequency of around 0.36 Hz and at the respective wave spectrum. For EC D the highest energy contribution in surge motion can be seen at a peak around the wave peak frequency, extending from the natural surge to the natural heave frequency. The heave responses for EC B and EC C show a peak at the corresponding wave spectra, a small peak at the heave frequency and a very sharp peak at the pitch decay frequency of 0.15 Hz. This indicates a very strong coupling between the heave and pitch motion of the floater, meaning that a pitch motion introduces a lot of heave motion. In the case of EC D, with the heave frequency and the wave peak frequency almost coinciding, the heave response is dominated by these frequencies. The power spectra of the pitch motion show a very sharp peak at the natural pitch frequency for all three sea states. For EC D and EC C there is also a small contribution at the corresponding wave peak frequencies. Interestingly for EC B there is no contribution at the exciting wave frequency visible, which suggests a high pitch flexibility.

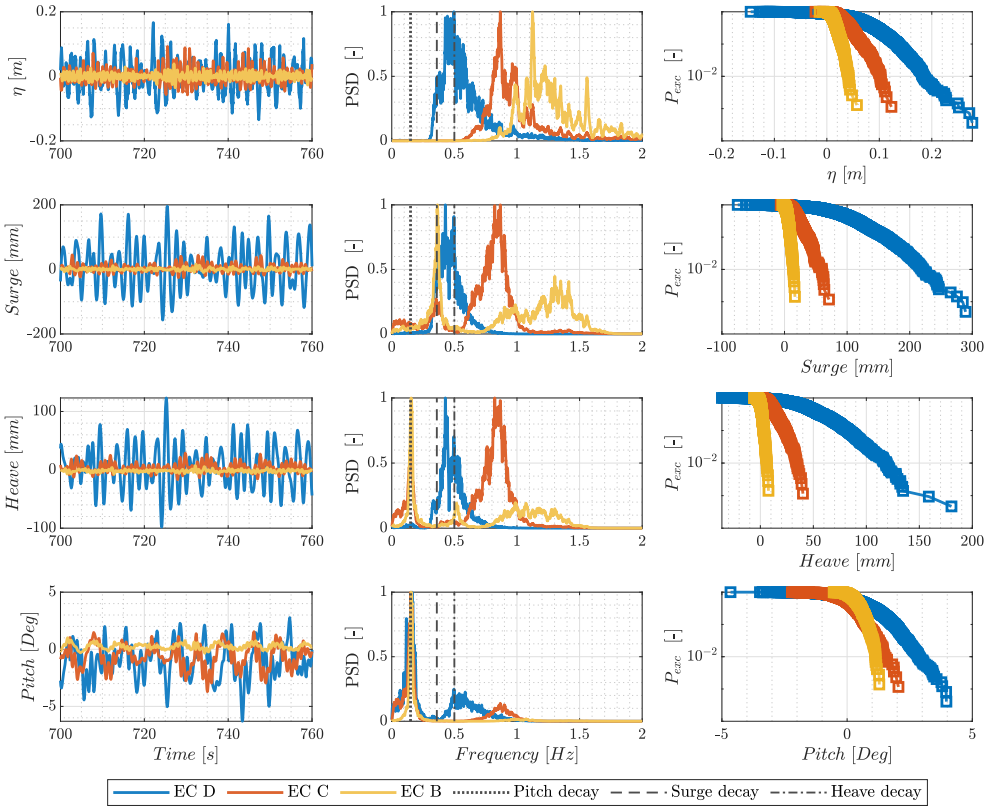

Figure 6.6: Surface elevation and surge, heave and pitch response of the floater in wave-only conditions for 3 different sea states.

Figure 6.7 displays the time-series, PSD and probability exceedance for the shear forces and accelerations at the tower-top in fore-aft (x) and side-side (y) direction for all considered sea states. As there is no wind in these tests, the only forces acting at the tower-top are inertial and gravitational forces. Because there is more motion in fore-aft direction than in side-side direction, there are also higher accelerations and therefore forces acting in this direction. Similarly, because there is more floater motion in the larger sea states, there are also higher forces and accelerations, as can be seen in the time-series and probability exceedance plots. However, the difference between EC B and EC C seems to be rather small. In terms of power spectra, the fore-aft shear forces and accelerations show peaks at the natural pitch frequency and the corresponding wave frequencies for all sea states. The sharp peak at the natural pitch frequency indicates again that the floater motion is dominated by the pitch motion. Curiously, for the extreme sea state EC D there is also a significant energy contribution around 1 Hz for all accelerations and forces. The reason for this

contribution is unclear, as this frequency is quite far away from both the exciting wave spectrum of EC D and the natural frequencies of the floater.

The power spectra of the side-side forces and accelerations are dominated by the corresponding wave spectrum and a sharp peak at 0.22 Hz, which corresponds to the natural roll frequency obtained in the decay tests. The natural frequencies observed in the wave-only cases therefore seem to agree well with the frequencies measured in the decay tests. The side-side power spectra show some additional energy contribution at around 4 Hz. This frequency is expected to be the natural tower frequency of the turbine. The exact natural tower frequency is unknown, as it depends on the support of the turbine. But because the natural tower frequency was found in a similar range in previous test campaigns, the peak at 4 Hz is assumed to be caused by the natural tower frequency.

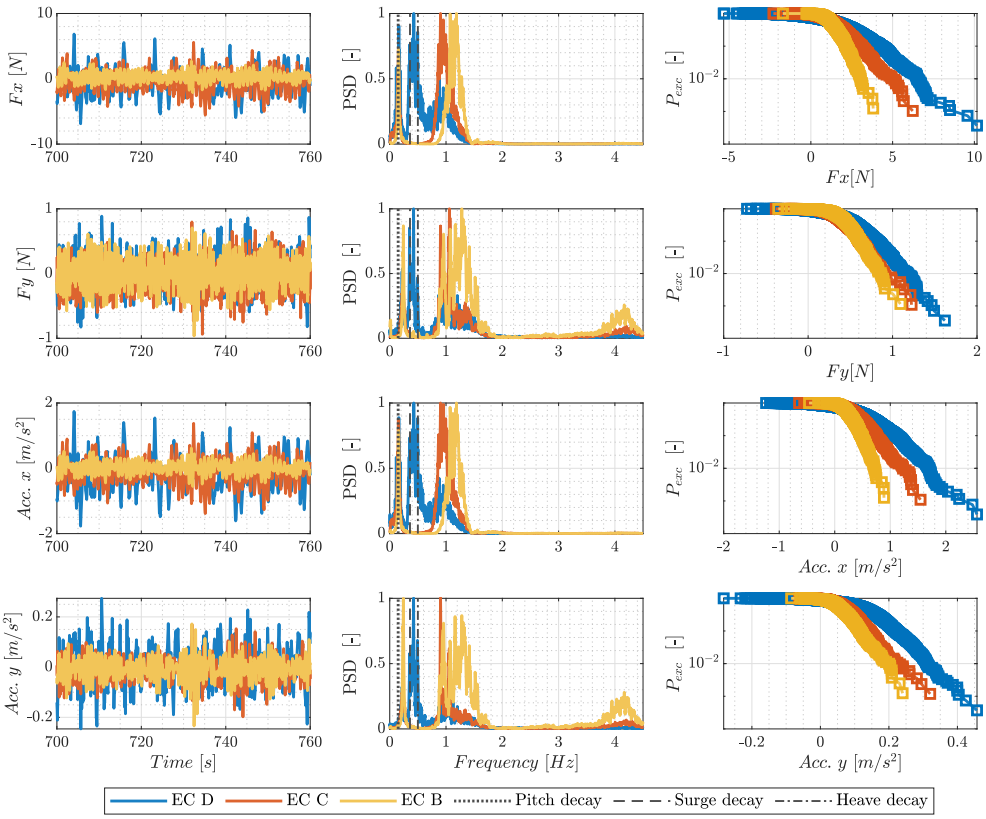

Figure 6.7: Shear forces and accelerations at the tower-top in fore-aft (x) and side-side (y) direction in wave-only conditions for 3 different sea states.

Figure 6.8 shows the time-series, normalized power spectra and probability exceedance for the tension in all three mooring lines. Because ML1 is aligned with the incoming waves, it experiences the highest motion and therefore the largest oscillations in the measured tension, as it can be seen in the time-series and probability exceedance. The magnitude of the oscillations in ML2 and ML3 seems to be very similar, as it is expected due to symmetry. The power spectra of the tension in ML1 for EC B shows a very broad peak around the wave frequency spectrum and a very sharp peak at the natural surge frequency. In the case of EC C there is also a peak around the wave peak frequency and a smaller contribution at the surge frequency. For EC C the wave spectrum seems to dominate the tension in ML1, while for EC B the surge frequency seems to be more important. In the case of the extreme sea state EC D, the power spectra of ML1 is dominated by a combined peak of surge, heave and wave frequency at around 0.5 Hz.

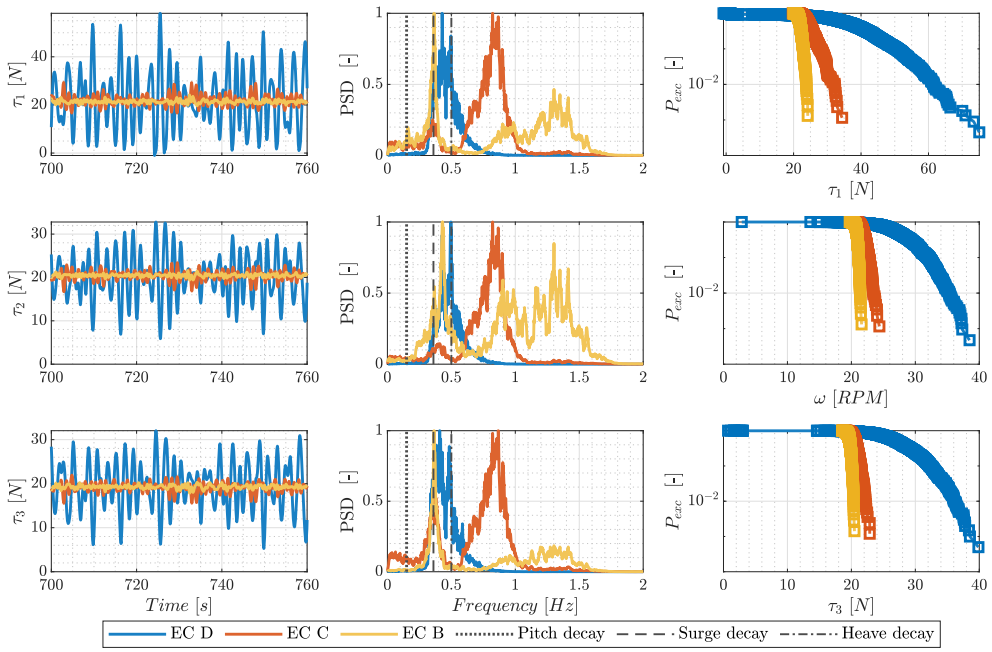

Figure 6.8: Forces in all three mooring lines in wave-only conditions for 3 different sea states.

The power spectra of the tension in ML2 shows large contributions at the wave frequency and surge frequency in the case of EC B, while for EC C and EC D there is only a small energy content at the surge frequency visible and the power spectra are mainly dominated by the wave frequency. The power spectra for ML3 show a higher contribution at the surge frequency than ML2 for all sea states. Similarly

to the regular wave results, this indicates that the mooring lines are not perfectly symmetrically aligned and are therefore differently affected by surge and sway motion.

6.2.3 Response to focused waves

In the next step of the analysis, the floater response to focused wave groups is investigated. Two different focused wave tests were carried out in the measurement campaign, representing EC 6 and EC 11. Each test had a total duration of 13:30 min, containing 8 realizations of a focused wave group separated by 100 s.

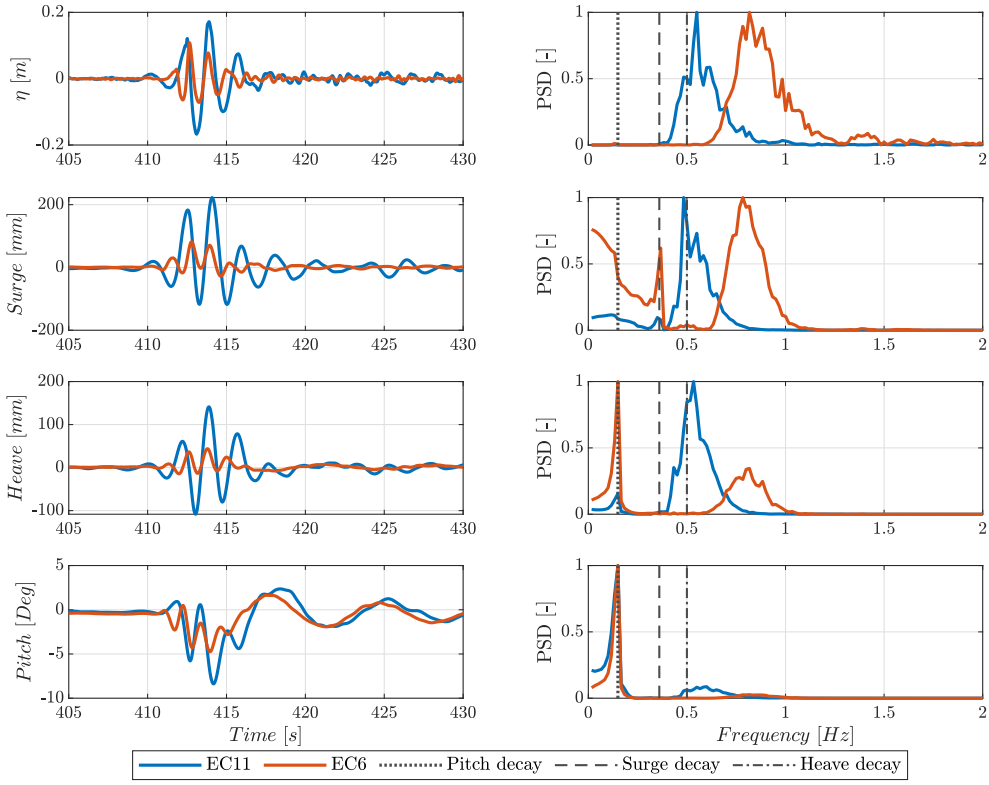

Figure 6.9: Surface elevation, surge, heave and pitch motion of the floater for focused waves.

Figure 6.9 shows the time-series of surface elevation and the corresponding surge, heave and pitch response of the floater for one realization of a focused wave group for both EC 6 and EC 11. The normalized corresponding power spectra are also displayed. The power spectra are calculated based on 60 seconds around the focused wave group and are normalized such that the maximum spectral density is unity. Due to the short

duration, the resolution of the power spectra is relatively coarse. It can be seen in the time-series that the surge and heave motion oscillate around approximately zero for the duration of the focused wave. The pitch motion however shows a negative mean value when the focused wave is hitting the floater, before returning back to a zero mean once the wave group has passed. A negative pitch angle corresponds to the floater leaning forward. A possible explanation of this behavior is the asymmetric design of the floater, which seems to cause a higher restoring moment for positive pitch angles than for negative pitch angles. In wind conditions the pitch angle is expected to be predominantly positive, because the aerodynamic thrust is acting on the turbine and pushing it backwards. Based on this consideration a higher restoring moment for positive pitch angles appears to be reasonable.

Regarding the power spectra, the floater surge motion shows a large peak at the wave frequency and a smaller contribution at the natural surge frequency for both sea states. The heave PSD for EC 11 is dominated by the wave frequency with only a small peak at the natural pitch frequency. For EC 6 however the peak at the natural pitch frequency is much larger than the peak at the wave frequency. This again highlights the strong coupling between pitch and heave motion, which could already be seen in the analysis of the irregular sea states. Similarly, the power spectra of the pitch motion is dominated by one sharp peak at the pitch natural frequency.

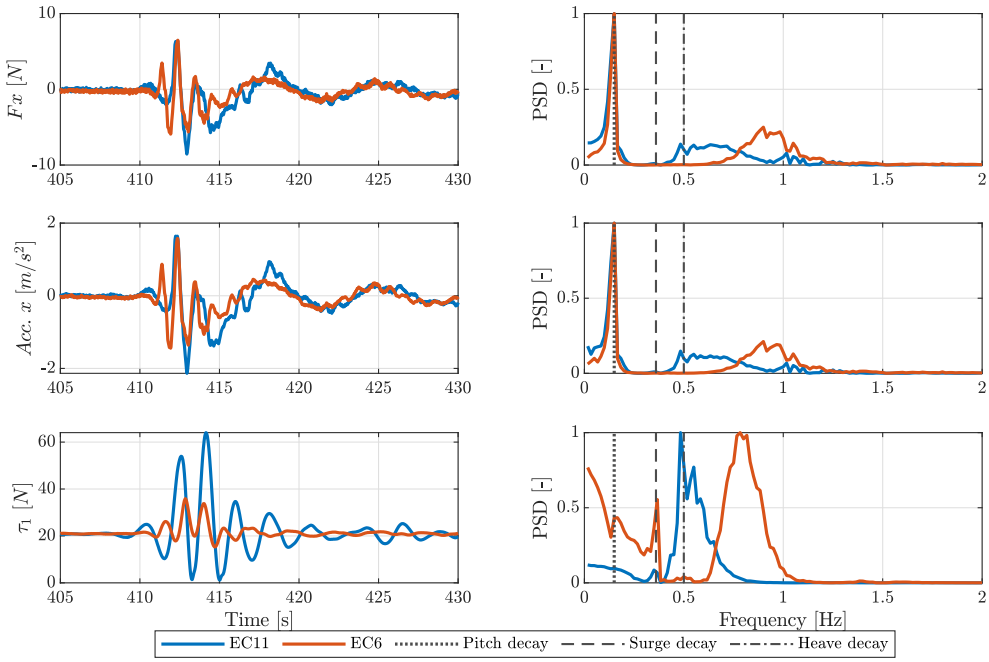

Figure 6.10: Tower-top shear force and acceleration in fore-aft (x) direction and front mooring line tension for focused waves for 2 different sea states.

Figure 6.10 displays the time-series and corresponding normalized power spectra of the tower-top fore-aft (x) shear force and acceleration, as well as the tension in ML1. In wave-only conditions, the only contribution to the fore-aft shear force at the tower-top, other than a minor gravitational contribution, is the inertia force, which is directly caused by the acceleration. Consequently, the shape of both the time-series and power spectra is almost identical for the shear force and acceleration. Both power spectra are dominated by the pitch natural frequency and have only a small contribution at the respective wave frequency. This illustrates again the high flexibility of the floater in pitch. The time-series and power spectra of the front mooring line tension is very similar to the corresponding time-series and power spectra of the surge motion, which highlights the strong correlation between the surge motion and the front mooring line tension. In general, the results from the focused wave tests agree well with the previous observations from the irregular sea states analysis.

6.2.4 Harmonic Decomposition

The wave kinematics described in Section 2.1.4.2 are based on linear wave theory. In a real-world lab environment, however, non-linear higher-order wave effects can also have a significant impact on the hydrodynamic loading and, consequently, the structural response. In order to investigate the influence of these higher-order effects on the floater behavior, the harmonic decomposition method proposed by Fitzgerald et al.(2014) [66] is applied. The method is briefly described hereinafter, for more details refer to [66, 67].

The free surface elevation η and other hydrodynamic quantities can be expressed as the summation of independent contributions of different order:

$$\eta_0 = \eta^{(1)} + \eta^{(2)} + \eta^{(3)} + \eta^{(4)} + \mathcal{O}(\epsilon^5) \tag{6.2}$$

Hereby the superscript (n) denotes the n-th order contribution. For a sufficiently narrow-banded spectrum, the classic Stokes-type perturbation expansion can be used to express hydrodynamic forces. Using this theory, the surface elevation can be expressed until the 5-th order as followed:

$$\begin{aligned}\eta_0 = {} & A\, b_{11}\, \cos\phi + A^2\, (b_{20} + b_{22}\, \cos 2\phi) + A^3\, (b_{31}\, \cos\phi + b_{33}\, \cos 3\phi) \\ & + A^4\, (b_{40} + b_{42}\, \cos 2\phi + b_{44}\, \cos 4\phi) + \mathcal{O}(\epsilon^5)\end{aligned} \tag{6.3}$$

Where A denotes the amplitude, ϕ the fundamental frequency and b_{nm} the interaction coefficient describing the interaction of the n-th order with the m-th harmonic frequency. For instance, the coefficient b_{31} describes the third order contribution to the first harmonic frequency (= fundamental frequency).

Expression 6.3 describes the free surface elevation created by a wave paddle signal with a zero degree phase shift (η_0). By shifting the wave paddle signal by 90°, 180° and 270°, similar expressions can be derived for η_{90}, η_{180} and η_{270}, respectively. The process for doing so is described in detail in a previous Master's Thesis at DTU by Steffensen (2020) [67]. Through the following different linear combinations of η_0, η_{90}, η_{180} and η_{270}, the total signal can be decomposed into individual harmonic contributions:

$$\frac{\eta_0 - \eta_{90}^H - \eta_{180} + \eta_{270}^H}{4} = A\, b_{11}\, \cos\phi + A^3\, b_{31}\, \cos\phi + \mathcal{O}(A^5) \tag{6.4}$$

$$\frac{\eta_0 - \eta_{90} + \eta_{180} - \eta_{270}}{4} = A^2\, b_{22}\, \cos 2\phi + A^4\, b_{42}\, \cos 2\phi + \mathcal{O}(A^6) \tag{6.5}$$

$$\frac{\eta_0 + \eta_{90}^H - \eta_{180} - \eta_{270}^H}{4} = A^3\, b_{33}\, \cos 3\phi + \mathcal{O}(A^5) \tag{6.6}$$

$$\frac{\eta_0 + \eta_{90} + \eta_{180} + \eta_{270}}{4} = A^2\, b_{20} + A^4\, b_{40} + A^4\, b_{44}\, \cos 4\phi + \mathcal{O}(A^6) \tag{6.7}$$

Hereby the Hilbert transform, denoted by the superscript H, is introduced, which shifts the phase of a signal by 90°. Eq. 6.4 yields the first harmonic, which consists of the linear contribution and some third order contribution. Eq. 6.5 expresses the second super-harmonic (twice the fundamental frequency), consisting of a second and fourth order contribution. The third linear combination Eq. 6.6 yields the third super-harmonic, which only contains a third order contribution, and hence the only single order signal (disregarding higher orders). Finally, Eq. 6.7 describes the fourth super-harmonic and the difference sub-harmonic, containing contributions from the second and fourth order wave field.

In the measurement campaign, the sea states EC 6 and EC 11 were realized with a 0°, 90°, 180° and 270° phase shift of the wave paddle signal. The results from these tests are used to apply the described harmonic decomposition to all signals of interest. Figure 6.11 shows the results of the complete harmonic decomposition of the surface elevation, pitch, surge and heave motion of the floater for EC 6. Displayed are the power spectra of the complete signal (with 0° phase shift) and of all the individual harmonics obtained with Eq. 6.4 - 6.7. Note that the spectra are displayed on a logarithmic scale. The probability exceedance of all individual harmonics is also displayed, which allows for a quick overview of the different contributions of the separate harmonics to the total signal. Note that the minimum distance between the peaks was not adjusted for each harmonic, instead the wave peak period of the corresponding sea states was used, which might influence the resulting probability exceedance plots.

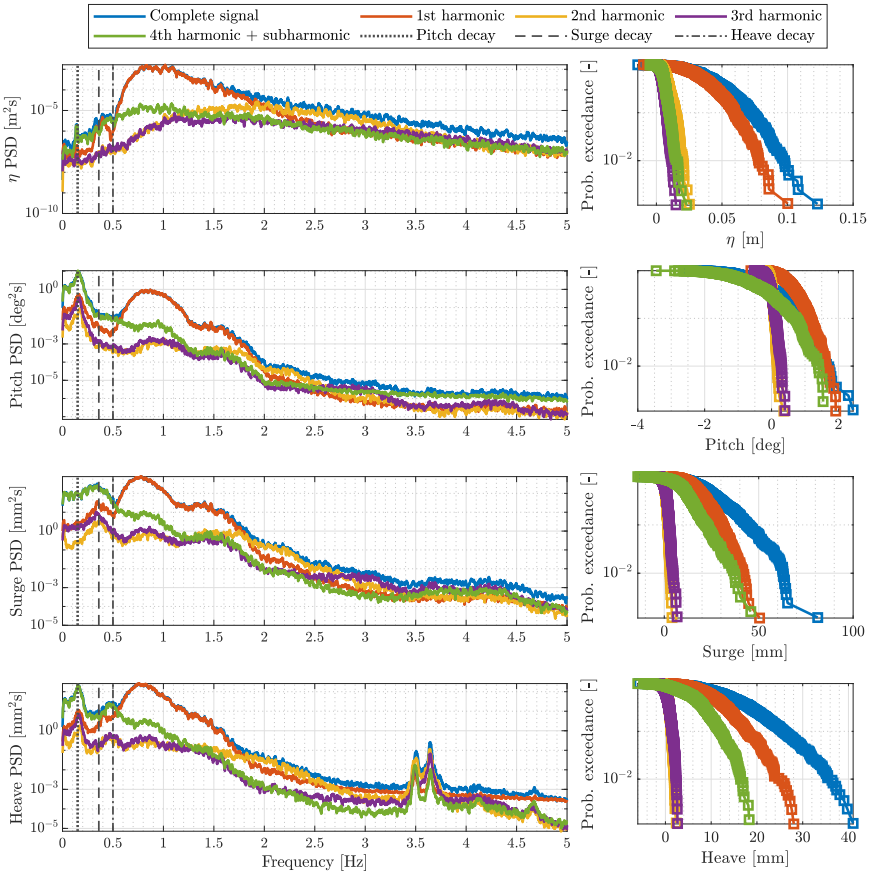

Figure 6.11: Harmonic decomposition for surface elevation (WG8), pitch, surge and heave motion for EC 6.

Looking at the surface elevation, it can be seen that the main contribution comes from the first harmonic and therefore mainly from linear effects. Only for frequencies above 2 Hz, the higher harmonics cause a visible difference between the complete signal and the first harmonic. For frequencies below 0.5 Hz, the contribution from the sub-harmonics can be seen. The power spectra of the complete pitch motion signal (blue line) shows a very large peak at the natural pitch frequency of 0.15 Hz and a smaller peak at the wave peak frequency of around 1 Hz. Looking at the contributions from the individual harmonics shows that the peak at the pitch frequency is mainly caused by the sub-harmonics. The pitch behaviour of the floater is therefore strongly influenced by the sub-harmonics, which are caused by higher order-wave effects. This highlights the importance of non-linear wave effects. The power spectra of the surge motion show a similar picture as the pitch motion. The

complete signal has a peak at the natural surge frequency and the wave peak frequency. Again the peak at the natural floater frequency is mainly caused by the sub-harmonic contribution. This effect can also be seen in the probability exceedance plot, in which the sub-harmonic signal has a similar contribution as the first harmonic signal. The heave power spectra are again similar to the pitch motion, with peaks at the natural pitch frequency (due to the already observed strong coupling between the pitch and heave motion) and the wave peak frequency. There is an additional double-peak in spectra at around 3.5-3.7 Hz, which might be caused by some influence of the natural tower frequency. Nonetheless, it should be kept in mind that the spectra are displayed on a logarithmic scale, which means that this peak seems large compared to the neighbouring frequencies, but is very small compared to the peaks at the pitch and wave frequency.

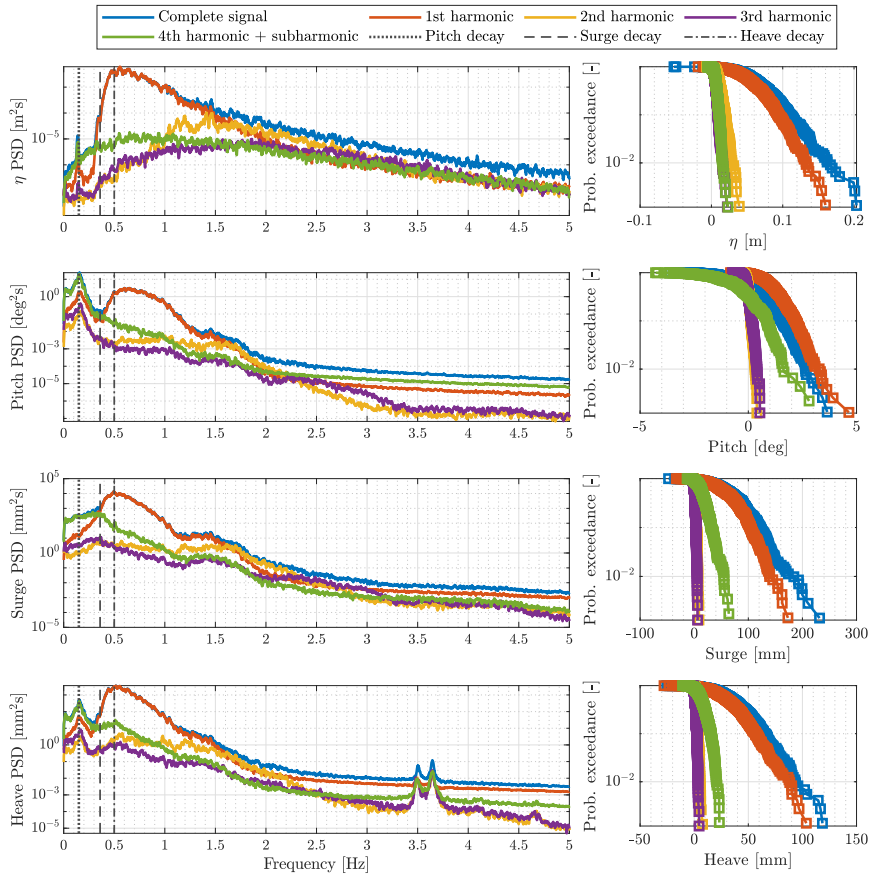

Figure 6.12: Harmonic decomposition for surface elevation (WG8), pitch, surge and heave motion for EC 11.

Figure 6.12 shows the results of the harmonic decomposition for surface elevation, pitch, surge and heave for EC 11. Similar observations can be made as for the case of EC 6. Again, the natural floater frequencies are mainly excited by the sub-harmonics. Because the wave peak frequency of EC 11 almost coincides with the natural heave frequency, there is a larger contribution at the natural heave frequency, especially for surge and heave motion.

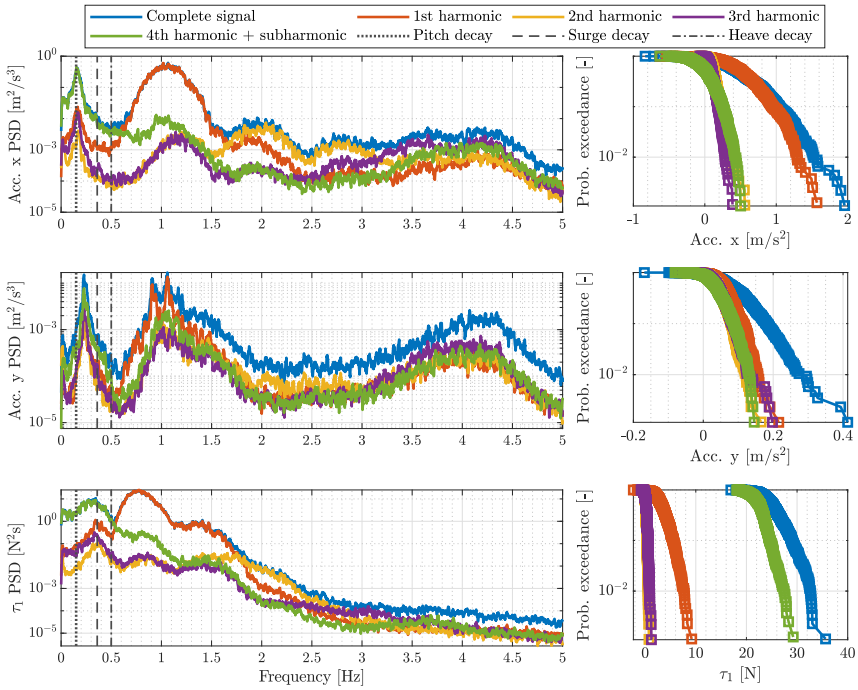

Figure 6.13: Harmonic decomposition for tower-top acceleration in fore-aft (x) and side-side (y) direction and tension in front mooring line for EC 6.

The results of the harmonic decomposition for the tower-top fore-aft (x) and side-side (y) acceleration and front mooring line tension are shown in Figure 6.13 for EC 6 and in Figure 6.14 for EC 11. The power spectra of the complete signal of the fore-aft acceleration have peaks at the natural pitch and the wave peak frequency. Once again, the natural pitch frequency seems to be excited by the sub-harmonics. In the case of EC11 the fore-aft acceleration shows an additional peak at around 1 Hz, which is different from the peak at the wave peak frequency of around 0.5 Hz. The harmonic decomposition shows that this frequency contribution is not caused by higher harmonics, as it is already contained in the first harmonic. The reason for this peak remains unclear and further investigation is necessary in order to determine its cause. For the side-side accelerations, the first peak in the spectra is slightly shifted

towards the roll frequency of 0.21 Hz, as it was already observed previously. The peak around 4 Hz, which is assumed to be the influence of natural tower frequency, can be seen in all harmonics, with the highest contribution from the 3rd harmonic, followed by the fourth harmonic.

The power spectra of the mooring line tension have almost an identical shape as the surge motion of the corresponding sea state for all harmonics. This is an expected result, as the front mooring line tension is mainly determined by the surge motion. The mooring line tension is the only signal with a non-zero mean due to the pretension of approximately 20 N. The probability exceedance plots show that this mean value was filtered out for all higher harmonics and only remains in the sub-harmonic signal and therefore also in the total signal, while the higher harmonics only show the dynamic contribution.

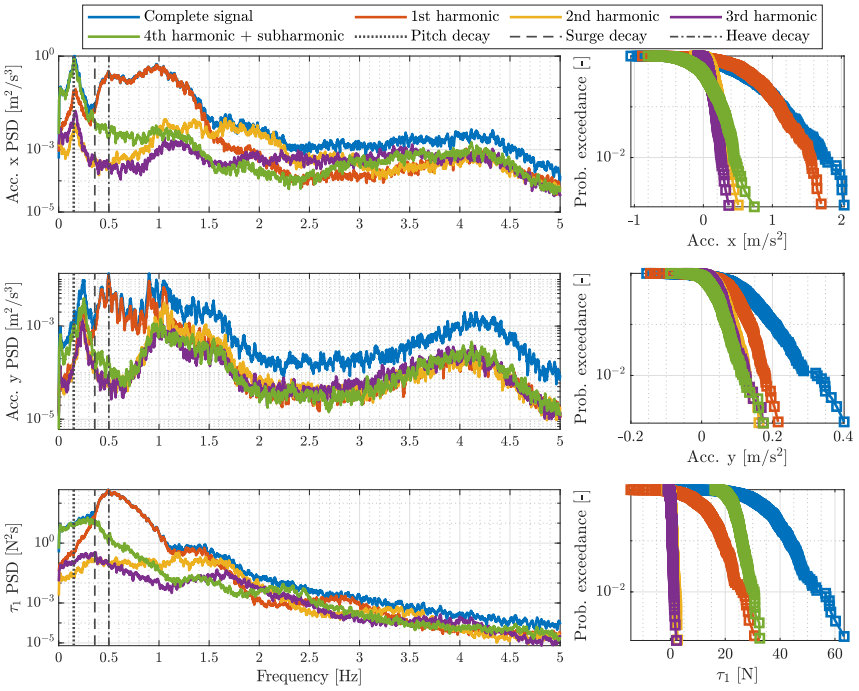

Figure 6.14: Harmonic decomposition for tower-top acceleration in fore-aft (x) and side-side (y) direction and tension in front mooring line for EC 11.

In conclusion, the harmonic decomposition shows that non-linear effects on the sub-harmonics have an important impact on the floater motion. In order to fully understand and simulate the hydrodynamic behavior of the tested floater, it is important to also take higher-order wave effects into account.

6.3 Wind-only tests

Wind-only tests were performed to tune the two different controllers. To that end, two different kind of wind-only tests were run. The wind step tests were mainly tested for tuning the baseline controller and the constant wind speed tests were used for tuning the tower-top loop controller. However, these tests were not logged in the DHI system, which means that only the wind turbine operational data was recorded. Once the controllers were tuned, some wind-only tests were logged in both systems, for the purpose of having a better picture of the system response. In this section the general behavior of the turbine is discussed using the results obtained with the baseline controller (A_003). A detailed comparison of the different controllers will be presented in section 6.5.

6.3.1 Wind step tests

The first wind-only tests was the wind step test, which consisted of keeping the rotational speed of all the fans of the wind maker constant for 60 seconds, after which the rotational speed was increased to the next value, and so on. The chosen rotational speeds and its corresponding wind speeds at hub height at the rotor plane can be seen in Table 6.1. Note that for a rotational speed around 1527 RPM, the fans experienced some resonance, and hence it was decided to skip this wind step.

Table 6.1: Different rotational speeds of the fans corresponding to every wind speed at hub height at the rotor plane.

ω_{gen} **[RPM]**	995	1102	1210	1317	1425	1527	1640	1747	1800
Wind sp. [m/s]	1.16	1.29	1.42	1.55	1.67	1.8	1.94	2.06	2.2

Figure 6.15 shows the system response for the eight different wind steps. It is again necessary to highlight that the measured wind speed was not measured at the rotor, but at the WP1 position (see Figure 5.1), and hence a correction factor, obtained during the wind calibration, was used. The first three wind steps are below rated wind speed and the remaining above rated. Together with the wind steps, the floater surge and pitch motion, the rotor speed, the generator torque, the blade pitch angle, the tower-top fore-aft (x) shear force and the front mooring line tension time-series are shown.

The whole system response is mainly influenced by the thrust force (see Figure 2.14). Once the controller is enabled, the blade pitch changes from the initial pitch angle (θ_{init}) to the minimum pitch angle (θ_{min}). In operational points below rated, the controller keeps the blade pitch constant and adjusts the generator torque in order to track the optimal C_p-value, as it was explained in Section 2.2.1.1. The aerodynamic thrust increases until it reaches its maximum value at the third wind step, which corresponds to rated wind speed. Therefore this step also experiences the

highest floater mean pitch angle, tower-top fore-aft shear force and front mooring line tension. For higher wind speeds the controller starts pitching the blades, reducing the aerodynamic thrust and keeping the rotational speed constant. It should be pointed out that the fore-aft shear force F_x shown in Figure 6.15 not only contains the aerodynamic thrust, but also a significant gravitational contribution due to the high mean pitch angle.

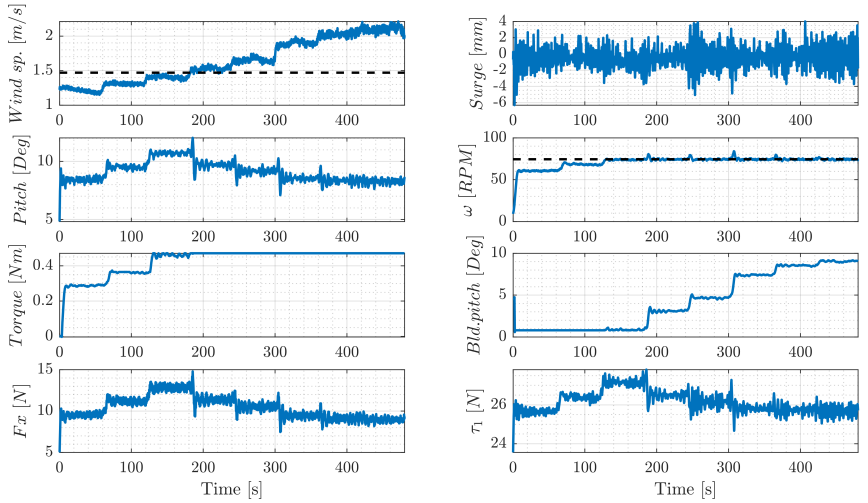

Figure 6.15: Performance of baseline controller (A_003) for a step wind test.

Due to the high pitch flexibility of the floater, which was already observed in the wave only tests, the floater experiences an unusual high mean pitch angle. Around rated wind speed, the pitch angle reaches values of over 10°. A pitch angle of this magnitude is usually not desired for a floating wind turbine. On the other hand, it should be highlighted that the TetraSub concept foundation was not designed and optimized for this particular turbine, which might influence the resulting pitch angle. Besides, the TetraSub foundation was first designed for full-scale and then downscaled without further modelling and analysis. Hence scaling effects could also influence the floater behavior.

In the fourth wind step, which would be critical in the case of a not detuned controller, rated conditions have been reached. The thrust is lower, and consequently all the parameters are reduced accordingly. However, note how every time the wind step is increased, there is a certain overshoot in the signals. This is mainly related to the fact that the detuned baseline controller is relatively slow, and hence it is not able to react to fast changes in the wind speed, leading to an overshoot of the blade pitch angle, which becomes noticeable for the floater pitch motion, the rotational speed, the tower-top shear force and the front mooring line tension.

The only parameter that does not seem to be influenced by the thrust force is the floater surge motion, which does increase for higher thrust values. It appears to suffer from higher oscillations whenever there is a new wind step, but other than that the mean value is rather constant. It was already observed in the wave-only tests that the floater only shows very small surge motion compared to the pitch motion. Presumably, the high mean pitch angle plays a more important role for the surge motion than the thrust itself pushing the system backwards.

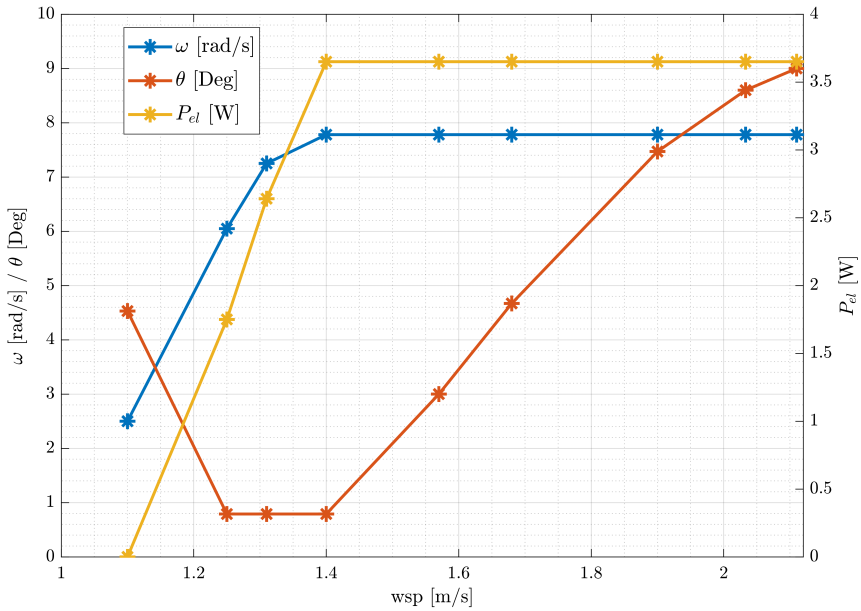

Figure 6.16: Rotational speed, blade pitch angle and electrical power versus wind speed curves for the baseline controller.

From the presented wind step test, the different operational curves of the wind turbine can be determined for the baseline controller (*A_003*). Three operational curves, namely, the rotational speed, blade pitch angle and electrical power curve are shown in Figure 6.16. Note how these curves built from the measured data are similar to the theoretical ones shown in Figure 2.11. There is a cut-in wind speed after which the wind turbine starts operating with its operational parameters at its initial values. Then, two evident operating areas can be observed: Region 1 (below rated) and Region 2 (above rated). In Region 1, the blade pitch angle is kept at its minimum, while both the rotor speed and the electrical power increase following the partial-load control strategy. In Region 2, the rotational speed and the electrical power is slightly oscillating around their rated values, while the blade pitch is increased to

limit rotational speed and power to their rated values.

6.3.2 Constant wind

The second of the wind-only tests was the constant wind test, which consisted of keeping the rotational speed of all the fans of the wind maker constant. Three cases were run: one wind speed below rated (V = 1.1 m/s), another wind speed just above rated (V = 1.68 m/s) and the maximum wind speed (V = 2.18 m/s).

Before analyzing the results, it is important to highlight that the system response is heavily influenced by the thrust force acting on the rotor. The thrust is the lowest for the wind speed below rated, and consequently resulting in the lowest system response. The thrust is the highest for the wind speed just above rated and slightly lower for the maximum wind speed, and consequently the rest of signals behave accordingly. Regarding the wind turbine operational parameters, the pitch angle is kept at its minimum while the generator torque and the rotational speed are controlled under the partial-load control strategy for the case of a below rated wind speed. Above rated, the blade pitch is constantly changing due to wind turbulence, leading to a bit of fluctuation in the rotational speed while keeping the generator torque at rated. Note how the blade pitch angle is higher for the maximum wind speed compare to the one for the wind speed just above rated, eventually leading to a lower thrust.

Figure 6.17 shows the time-series, PSD and probability exceedance for the floater surge and pitch response, as well as the rotational speed for the different wind speeds. The floater surge motion seems to experience larger oscillations for the wind speeds above rated as seen in both the time-series and exceedance probability plots. In terms of power spectra, the surge motion has a sharp peak around the natural surge frequency of 0.36 Hz for all the wind speeds as well as some minor energy content at 0.92 Hz for the lowest wind speed, which corresponds to the 1P frequency. As expected, the mean floater pitch is the highest for the largest thrust and vice versa. The power spectra of the pitch motion shows a high energy content around the pitch natural frequency, a smaller energy content around the wind spectrum frequencies as well as a residual peak around the 1P frequency (1.23 Hz) from the rotating blades for the wind speeds above rated. For the wind speed below rated, an important energy content is seen around the wind spectrum frequencies and a minor content is observed around the floater pitch natural frequency. Note how the pitch natural frequency has been slightly shifted to the right as a result of the new equilibrium point found from the highly tilted system. One could think that the higher the thrust, the higher the mean floater surge motion. However, the mean floater surge seems to be more negative the higher is the thrust, probably as a result of the tilted system. While the rotor speed PSD shows a high energy content around the wind spectrum frequencies for the wind speed below rated, there is a high energy content around the pitch natural frequency and a smaller peak at the 1P frequency for the wind speeds above rated. Below rated the rotor speed mainly depends on the wind speed, while above rated it mostly depends on the blade pitch angle changes, which are mainly

driven by the floater pitch motion.

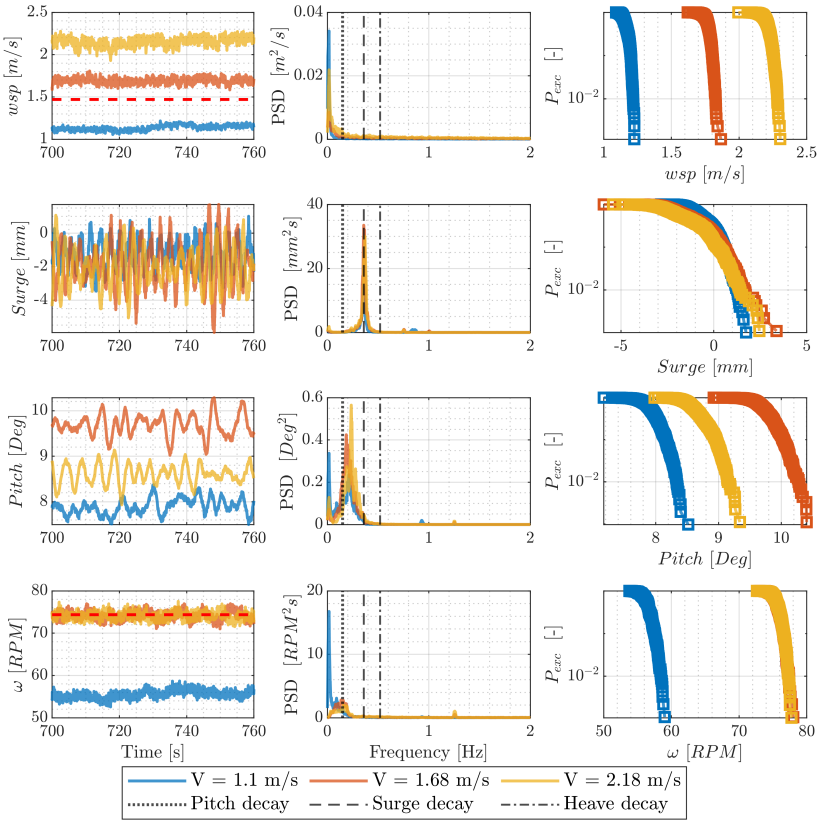

Figure 6.17: Surge, pitch and rotational speed in wind-only conditions for 3 different wind speeds with the baseline controller (A_003).

Figure 6.18 displays the time-series, PSD and probability exceedance for the tower-top shear forces and accelerations in fore-aft (x) and side-side (y) direction for all the wind speeds. The tower-top shear force in fore-aft direction is the result from both the partial contribution of the thrust forces acting on the rotor and the gravitational forces experienced when the system is tilted. Then, the signal is amplified when the thrust is higher, since the floater pitch is higher, hence increasing the gravitational contribution. The same can be said for the acceleration in the fore-aft direction. Both the shear forces and accelerations in fore-aft direction are higher for the wind speed just above rated and lower for the wind speed below rated as seen in the time-series and exceedance probability plots.

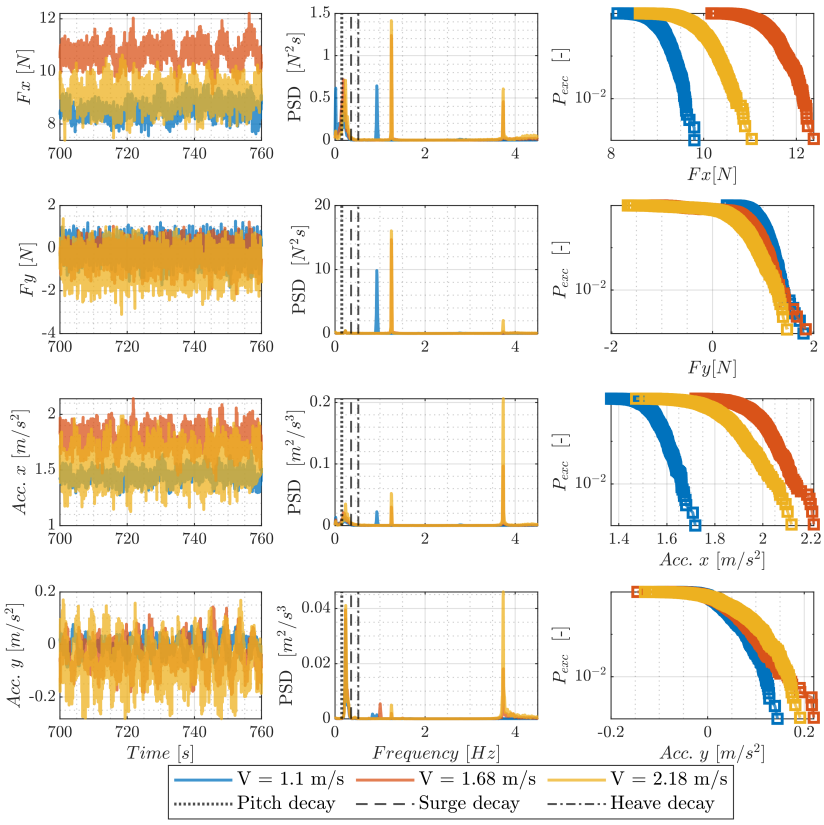

Figure 6.18: Tower-top shear forces and accelerations in fore-aft (x) and side-side (y) direction in wind-only conditions for 3 different wind speeds with the baseline controller (A_003).

In terms of power spectra, the fore-aft shear force presents a high energy content around the floater natural pitch frequency, a lower energy content around the assumed tower natural frequency of around 4 Hz, as well as a sharp peak at the 1P and 3P frequencies of the corresponding wind speeds. The same can be said for the fore-aft accelerations, but the 3P peak is higher than the 1P peak for this case. Likewise, a high energy content is observed around the wind spectrum frequencies and around a range of frequencies centered at the natural pitch frequency. The power spectra of the side-side shear forces are mainly dominated by sharp peaks at the 1P and 3P frequencies of the corresponding wind speeds. The side-side accelerations also show an important contribution from the 3P and 1P frequencies. Besides, an important contribution is observed for all the wind speeds for a range of frequencies centered at

0.22 Hz, which corresponds to the natural roll frequency obtained in the decay tests.

Figure 6.19 shows the time-series, power spectra and probability exceedance for the tension in all the three mooring lines for all the wind speeds. Because ML1 is aligned with the incoming wind, it experiences the largest tensions, which are the highest for the largest thrust forces, and vice versa, as it can be seen in the time-series and exceedance probability plots. The magnitude of the tensions in ML2 and ML3 are the lowest for the wind speed below rated, medium for the wind speed just above rated and maximum for the maximum wind speed. Note that the difference between tensions in ML2 and ML3 comes from the fact that it was very difficult to manually adjust the initial pretension of the three mooring lines to the same initial values. Furthermore, the wave-only tests already showed that ML2 and ML3 were not perfectly symmetric.

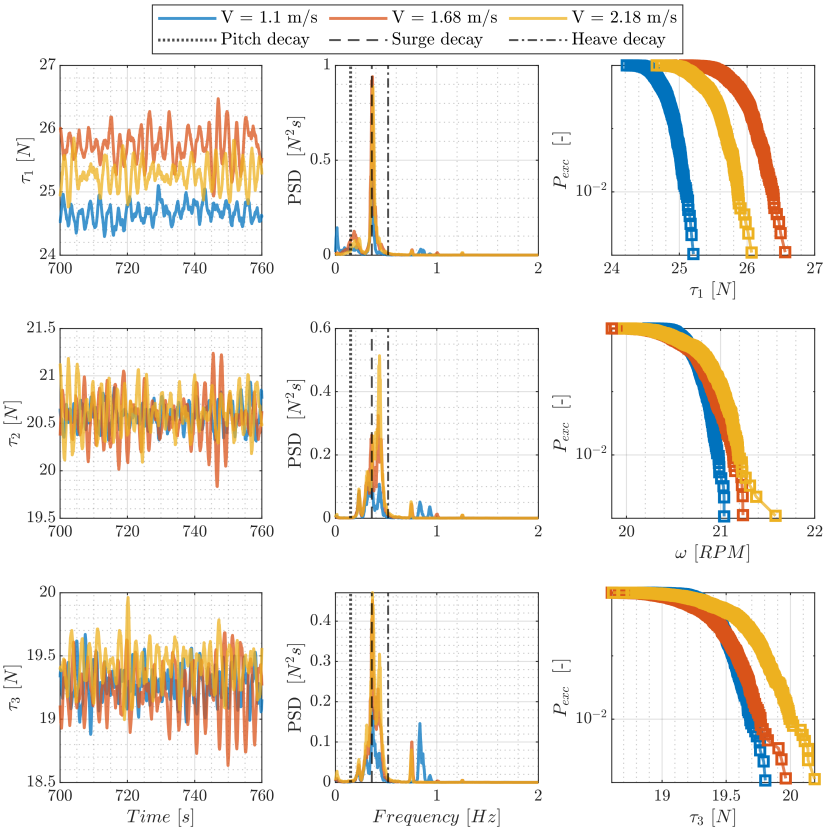

Figure 6.19: Mooring line tensions in wind-only conditions for 3 different wind speeds with the baseline controller (A_003).

The power spectra of the tension in all the mooring lines for all the wind speeds show a sharp peak around the natural surge frequency, which means that the tension in the mooring lines is mainly driven by the floater surge motion. However, the peak seems to be a little bit shifted to the right around 0.42 Hz for ML2, which could also be caused by the mooring lines not being perfectly symmetric. For the wind speed below rated, there exists a small energy content for ML1 around the wind spectra range of frequencies as well as a peak around the 1P frequency of 0.92 Hz. For the wind speed above rated there is also a smaller peak around 0.8 Hz for all mooring lines. The origin of this peak is unknown, as it does not match any of the known exciting frequencies or natural frequencies. Lastly, ML2 and ML3 show a sharp peak around the roll natural frequency for all the mooring lines and wind speeds.

The results of the wind-only tests showed that the aerodynamic thrust is causing a high mean pitch angle of the floater, which confirms the observation of a high pitch flexibility from the wave-only tests. In the next step the combined effect from wind and wave loads on the floater will be investigated.

6.4 Wind and waves

To assess the system response under normal operating conditions, i.e. under wind and waves acting on the system simultaneously, wind and waves tests were conducted. These wind and waves tests consisted of reproducing any of the aforementioned sea states together with a constant wind speed. The analysis in this section will focus on **EC C** (see Table 6.2). To measure the effect of the wind forcing on the system response, the results will be compared to the **EC C** sea state without wind. Note that the baseline controller (A_003) was applied in the case of having wind included.

Figure 6.20 shows the time-series, power spectra and exceedance probability of the free surface elevation, floater surge, heave and pitch motion for the two cases of study. The surge motion presents higher oscillations for the wind and waves case, as seen in the exceedance probability plot. The effect of including wind results in a mean floater pitch offset as shown in both the time-series and exceedance probability plots. Now, the rotor not only experiences gravitational and inertial forces, but also aerodynamic forces eventually leading to a tilted wind turbine. This and the way the Qualisys system captured the 6 DoFs motion may explain the main offset observed in the floater heave motion. The inclination of the aluminum frame used for capturing the 6 DoFs motion results in a negative heave in comparison with the waves-only case.

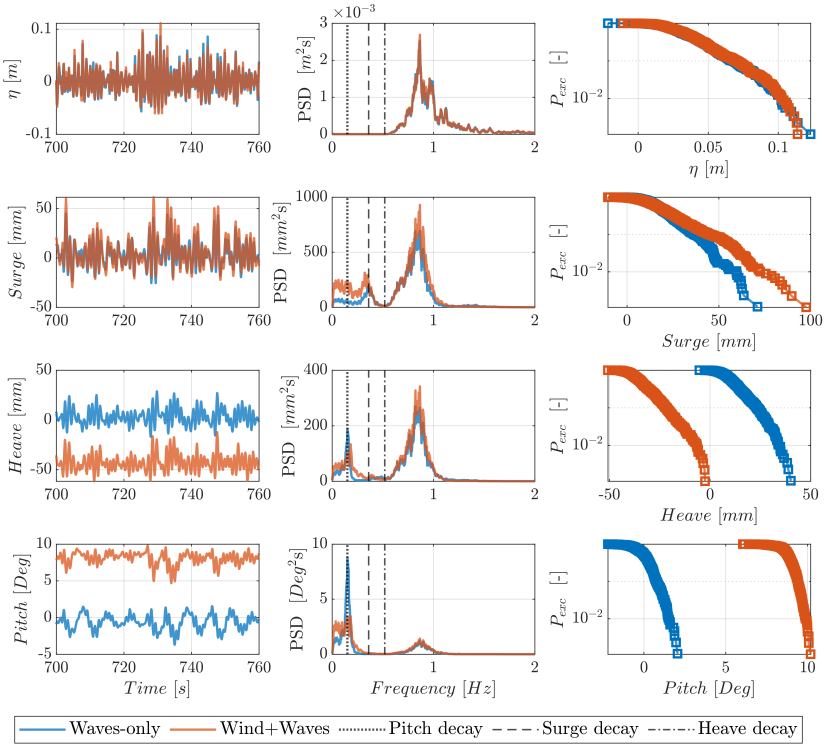

Figure 6.20: Floater response in irregular waves with and without wind for EC C.

Regarding power spectra, the floater surge motion shows an important contribution from the wave spectrum as well as a minor contribution around the surge natural frequency for both cases. In the case of including wind, a minor contribution around the wind spectra can be observed. The floater heave motion shows an important contribution from both the wave spectrum and a range of frequencies centered at the pitch natural frequency for both cases. The floater pitch rotation is mainly driven by the natural pitch frequency and smaller energy contents around the wave and wind spectrum frequencies.

Figure 6.21 displays the time-series, PSD and probability exceedance for the tower-top shear forces and accelerations in fore-aft (x) and side-side (y) direction for the two cases of study. A mean offset can be observed in the shear forces and accelerations in the fore-aft direction between both cases. This can be observed in both the 1-minute time-series window and the exceedance probability plots. As aforementioned, in the wind and wave case aerodynamic forces are added on top of the inertial and gravitational forces experienced at the tower-top. A comparison of the time-series of the fore-aft shear force and acceleration, with and without wind, clearly illustrates

how the wind loads determine the mean value of the response, while the wave loads dominate the dynamic part of the response. Regarding the tower-top shear forces and accelerations in the side-side direction, larger oscillations can be observed in both the time-series and exceedance probability plots for the case of including wind.

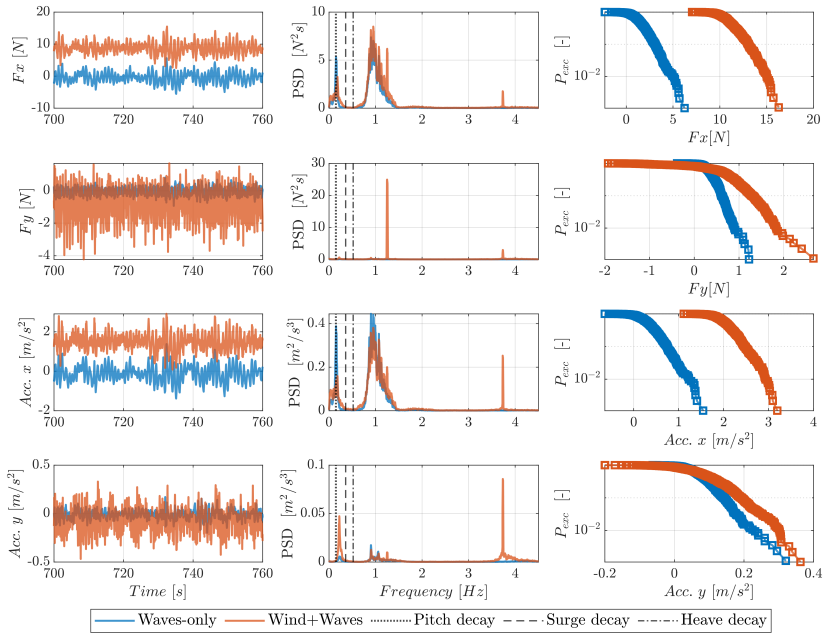

Figure 6.21: The comparison of the tower-top accelerations and shear forces response in irregular waves with and without wind for EC C.

In terms of power spectra, the tower-top shear forces and accelerations in the fore-aft direction show an important energy contribution around the wave spectrum frequencies and the pitch natural frequency for both cases. However, sharp peaks can be observed at the 1P and 3P frequencies in the case of including wind. The 1P peak is higher for the shear force, while the 3P is higher for the acceleration. With respect to the shear forces and accelerations in the side-side direction, the higher energy content in the waves and wind case does not allow to discern the power spectra for the waves-only case. There exists a high energy content around the wave spectrum frequencies and the roll natural frequency as well as a minor energy content around 4 Hz, which is assumed to be around the natural tower frequency. The side-side shear force for the wind and waves case shows a high peak at the 1P frequency and a minor one at the 3P frequency, while the contrary happens for the side-side acceleration. Also, a minor contribution around the roll and tower natural frequency can be observed for

this case.

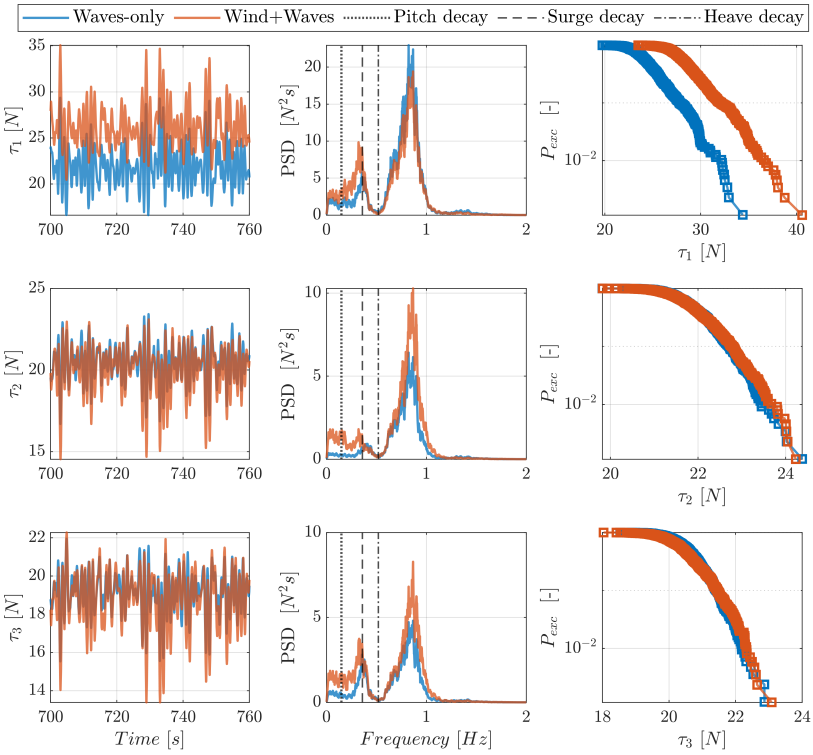

Figure 6.22: Mooring line tensions in irregular waves with and without wind for EC C.

Figure 6.22 shows the time-series, power spectra and probability exceedance for the two cases of study. Following the same reasoning as before, the wind and waves case experiences the highest tensions in ML1 since wind and waves are aligned and the total contribution comes from both the wind and wave forcing. This can be confirmed taking a look at the time-series and exceedance probability plots. However, the same cannot be said for ML2 and ML3, which seem to have a pretty similar behaviour for both cases. Because ML2 and ML3 are not aligned with the wind, the influence of the additional wind loading cannot be seen as clearly as for ML1. In terms of power spectra, all the mooring lines show a high energy content around the wave spectrum frequency and a minor contribution coming from a range of frequencies around the surge natural frequency for both cases. However, the energy content around the surge natural frequency for ML2 seems to be considerably lower than the one in ML3,

likely due to the small asymmetry of the mooring line system. Furthermore, a small contribution can be seen around the pitch natural frequency and the wind spectra frequencies for the wind and waves case.

The analysis of the wind and wave cases showed that the combined effect of wind and waves increases the response of the floater. Hereby the wind loads mainly effect the mean value of the response, as it was seen in the high mean pitch angle, while the wave loads dominate the dynamic part of the floater response.

6.4.1 Effects of wind and wave misalignment

In order to analyze the effects of wind and wave misalignment a number of test with a wave heading of $\beta = 30°$ were carried out. The floater motion was captured by the Qualisys system in the global floater coordinate system (x, y). However, when dealing with misaligned waves, the response is normally projected into the wave coordinate system ($\hat{x}$, $\hat{y}$). This allows for a more appropriate comparison of the effect of misalignment on the different degrees of freedom, hence the surge, sway, roll and pitch (ξ_1, ξ_2, ξ_4, ξ_5) in cases with wave misalignment were projected as described in Eq. 6.8, while heave and yaw (ξ_3, ξ_6) remained unchanged. It should also be noted that both the tower-top shear forces and accelerations were also projected into the wave coordinate system.

$$\begin{aligned} \hat{\xi}_1 &= \xi_1 \cos(\beta) + \xi_2 \sin(\beta) & \hat{\xi}_4 &= \xi_4 \cos(\beta) + \xi_5 \sin(\beta) \\ \hat{\xi}_2 &= \xi_2 \cos(\beta) - \xi_1 \sin(\beta) & \hat{\xi}_5 &= \xi_5 \cos(\beta) - \xi_4 \sin(\beta) \\ \hat{\xi}_3 &= \xi_3 & \hat{\xi}_6 &= \xi_6 \end{aligned} \tag{6.8}$$

The chosen EC for the misalignment analysis is **EC C** (see Table 6.2), since it was the only case for which all the needed tests were run. Furthermore, the baseline controller (A_003) was used for the cases with wind. As a result of the projection, the x,y-directions refer to fore-aft and side-side accelerations in the wave coordinate system for the cases with wind and wave misalignment. All in all, four cases will be presented in each figure; aligned and misaligned waves with and without wind.

Figure 6.23 depicts the free surface elevation, floater surge, heave and pitch motion time-series, power spectra and exceedance probability plots for the four cases of the analysis. Note that the free surface elevation was measured by WG8, which was placed 4 m next to floater at the same distance to the wave maker as the turbine (see Figure 4.8), to have a better picture of the waves acting on the system. Taking a look at the floater surge motion, it seems that the largest response is given when the wind and waves are aligned; on the contrary the case with misaligned waves without wind shows the lowest response. Moreover, the wave alignment seems to have a higher influence on the surge response than the effect of having wind, as it can be observed in the exceedance probability plot. Regarding the power spectra, all of the cases are mainly dominated by the wave frequency range and a range of frequencies around the surge natural frequency.

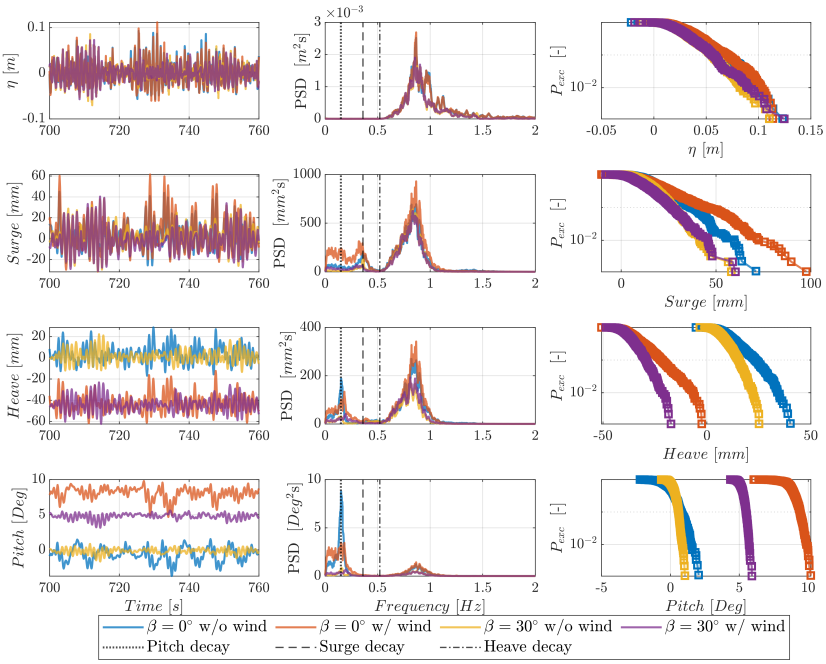

Figure 6.23: The comparison of the floater response in irregular waves with wave heading $\beta = 0°$ and $\beta = 30°$ with and without wind for EC C.

In the case of the floater heave motion, the energy content is always higher with no misalignment and even higher whenever there is wind as seen in the PSD plot. The energy content is mainly seen around the wave frequency range and a range of frequencies around the pitch natural frequency for all the cases. However, whenever wind is included, the pitch natural frequency peak seems to be shifted towards slightly higher frequencies. This can be explained as the modification of the whole system due to the high mean pitch angle leading to a small modification of the floater natural pitch frequency. As seen in the time-series and exceedance probability plots, the floater heave motion shows a negative mean whenever there is wind included as a result of the high floater mean pitch and the way the Qualisys system captures the floater motion. Note also that the heave motion shows lower oscillations for 0° wave heading. Regarding the floater pitch motion, in the wind and wave cases the mean pitch angle is clearly smaller for the misaligned case, which is a direct consequence of projecting the pitch motion, which is mainly caused by wind loads, into the wave direction. In the wave only cases, the mean pitch is similar but the oscillations are larger for the aligned case, indicating a higher stiffness in the projected direction. All of the cases show an important energy content around the wave frequency range and the pitch natural frequency, slightly shifted to the right in the case of including wind.

It is also important to highlight an energy content around the roll natural frequency in the case of wave-only with misalignment, as well as an important energy content around the wind spectra for the cases including wind.

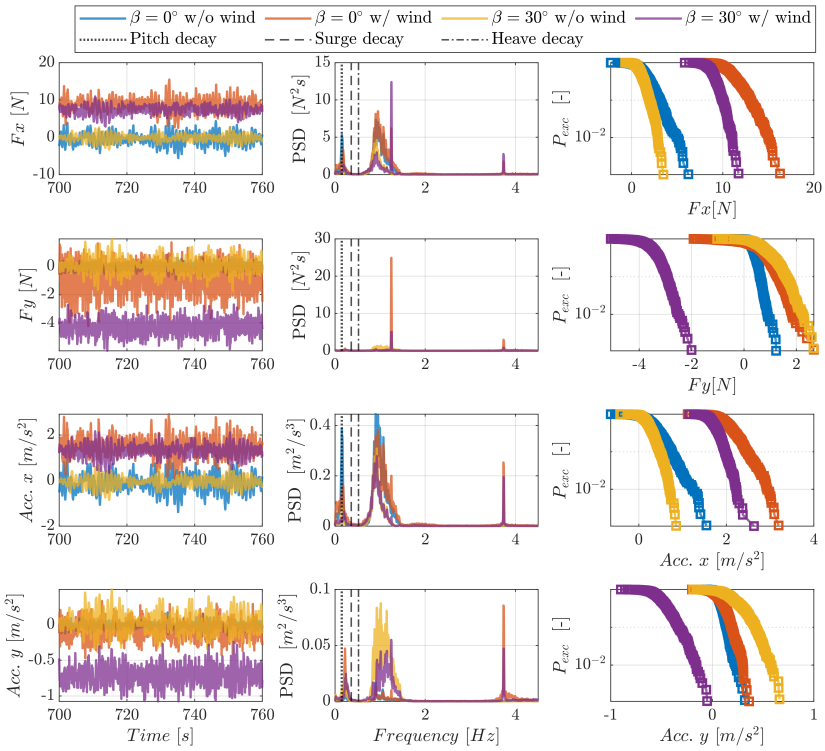

Figure 6.24: The comparison of the tower-top accelerations and shear forces response in irregular waves with wave heading $\beta = 0°$ and $\beta = 30°$ with and without wind for EC C.

Figure 6.24 shows the tower-top shear forces and accelerations in the fore-aft (x) and side-side (y) direction time-series, power spectra and exceedance probability plots for the four cases of study. Taking a look at the fore-aft shear forces and accelerations time-series and exceedance probability plots, the behaviour is quite similar for both of them. The largest response is given in aligned waves and wind as the wind forcing is added on top of the wave forcing together with a static gravitational component due to the tilted system. In terms of power spectra, all the cases show an energy content around the wave frequency spectrum and the pitch natural frequency. In addition, sharp peaks can be seen around the 1P and 3P frequencies, being higher at the 1P frequency for the shear forces, and vice versa for the accelerations whenever

wind is included. These peaks are specially important for the case of wind and waves misalignment since the wind effects are more important than the misaligned waves. Likewise, the side-side shear forces and accelerations seem to have a similar behaviour. Since the signals do not have their mean value subtracted, a permanent offset for the wind and wave misaligned case is observed, since the wind induces a component in the negative $\hat{y}$-direction. For the waves-only cases, an energy content can be seen around the roll natural frequency and the wave frequency spectrum, as well as a lower energy content around the assumed tower natural frequency for the case of aligned waves. For the cases with wind and wave, the side-side shear forces show a very sharp peak around the 1P frequency as well as a minor peak around the 3P frequency. This could be caused by a rotor imbalance, resulting into a 1P and 3P excitation due to gravitational forces. The side-side accelerations also show a higher peak at 3P and a minor peak at 1P. Moreover, an energy content is seen around the roll natural frequency, the wave frequency spectrum and the tower natural frequency.

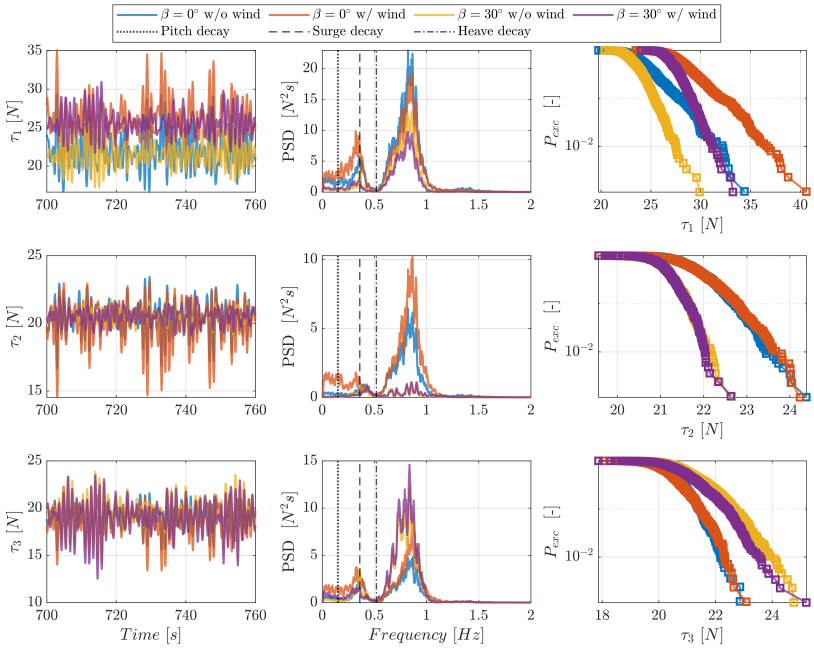

Figure 6.25: Mooring line tensions in irregular waves with wave heading $\beta = 0°$ and $\beta = 30°$ with and without wind for EC C.

Figure 6.25 depicts the mooring lines tension time-series, power spectra and exceedance probability plots for the four different cases of study. The largest tensions for ML1 are given for the case of aligned wind and waves as the external loads are

aligned with the line. The inclusion of wind causes the system to be tilted, which causes the fair lead to be in a higher position over the SWL, and eventually leading to a higher tension in ML1. The lowest tension in ML1 is given for the case of misaligned waves without wind since ML1 is no longer aligned with the waves. For the two mooring lines in the back, the wave alignment is the most important factor determining their response. In the case of wave misalignment, the waves are aligned with ML3, and hence the tensions are the highest in this case, the contrary happens with ML2 that experiences the lowest tensions due to a higher misalignment between the waves and ML2. In terms of power spectra, all of the cases show an important energy content around the wave frequency range and surge natural frequency.

The very high mean pitch angle caused by the aerodynamic thrust complicates the analysis of the wind and wave misalignment cases. In the presented analysis, the floater motion as well as the tower-top shear forces and accelerations were projected into the wave direction, while the aerodynamic forces are still acting in the wind direction, making it difficult to directly compare wind and wave induced effects. A more detailed comparative analysis of projected and non-projected cases would be necessary to draw definite conclusions from the misalignment cases.

6.5 Controllers comparison

The floating wind turbine model was tested in a range of wind and wave conditions and with different control strategies. A particular set of wind-wave climates (see Table 6.2) was run for both controllers: the baseline controller (*A_003*) and the tower-top loop controller (*D_008*).

Table 6.2: Environmental conditions tested for both controllers.

Environmental condition		**EC C**	**EC 5**	**EC 6**
H_s[m]	Full scale	4.986	4.014	6.168
	Model scale	0.0831	0.0669	0.103
T_p [s]	Full scale	8.6	6.74	8.6
	Model scale	1.111	0.87	1.11
V_{hub} [m/s]	Full scale	17.0	13.0	17.0
	Model scale	2.2	1.67	2.2
T_{dur} [min]	Full scale	180	180	180
	Model scale	25	25	25
Misalignment		0°	0°/30°	0°/30°

6.5.1 Response to Step Wind tests

Figure 6.26 shows the performance of the two different controllers for one of the aforementioned step wind tests. As both controllers follow the same partial load strategy and the tuned parameters are identical below rated, the performance of the controllers only depends on the turbulence of the wind coming from the wind generator for this operating conditions. For this reason, the wind steps below rated have not been depicted.

Despite minor differences due to turbulence, the wind speed for the wind steps seem to match quite well. The first wind step shown corresponds to a wind speed just above rated, the operational point in which the pitch instability is most critical. In fact, this can be appreciated in the large floater pitch oscillations experienced under the tower-top loop controller. These oscillations lead to the same behaviour for the rest of the logged signals, except for the generator torque, which is kept constant by the applied constant torque strategy. In general terms, the baseline controller presents lower oscillations. However, taking a look at the rotational speed, there are higher overshoots for the baseline controller than for the new tower-top loop controller every time there is a wind speed change. Note that the applied wind steps were small, corresponding to changes of only 1 m/s on full-scale. For larger wind speed changes, these overshoots could eventually damage the generator or even result in turbine shutdowns. This evidences that even though the oscillations are lower for the baseline controller, the fact that the controller cannot respond to very fast changes of the wind speed may incur into some undesired problems. For instance in

the case of an extreme wind gust, the slow reaction of the baseline controller could result in very large extreme loads.

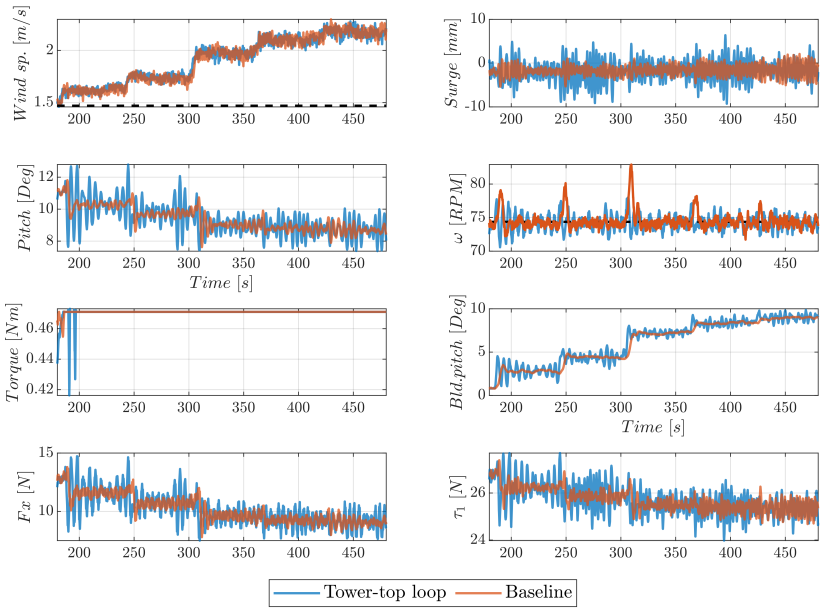

Figure 6.26: Performance of the two different controllers of study under a step wind test.

6.5.2 Response to Irregular Waves with Wind

After analyzing the step wind test, now the performance of the controllers under normal operational conditions is investigated. Since the pitch instability effects are largest around rated conditions, the environmental condition **EC 5** without wave misalignment is chosen for comparing the impact of the controllers on the system response. Furthermore, this EC was also tested for the slowest detuned offshore controller (A_001) and the results will also be included in the analysis. See Table D.2 from the Appendix D for more details of the aforementioned controller.

In Figure 6.27 the free surface elevation, floater surge, heave and pitch motion time-series are presented together with their corresponding power spectra and exceedance probability plots for the three different controllers. The floater surge response is almost identical for the three controllers, showing slightly higher oscillations for the tower-top loop controller as can be observed in both the time-series and exceedance probability plots. Looking at the power spectra plots, it is observed that the surge motion is mainly dominated by the surge natural frequency together with a smaller

excitation coming from the wind spectrum and the wave frequency ranges. The heave and pitch motion are mainly dominated by the pitch natural frequency. However, the energy content around the pitch natural frequency is higher for the case of the tower-top loop controller in comparison with the others, even making the wave frequency range not visible in the case of the floater pitch motion. This sharp peak at the pitch frequency highlights the influence of the tower-velocity loop in the new controller, which is directly driven by the pitch motion of the turbine. An energy content around the wind spectrum frequencies can be spotted for the baseline and detuned controller. The floater pitch time-series signal shows slightly higher oscillations for the case of the tower-top loop controller, which can be confirmed looking at the exceedance probability plots.

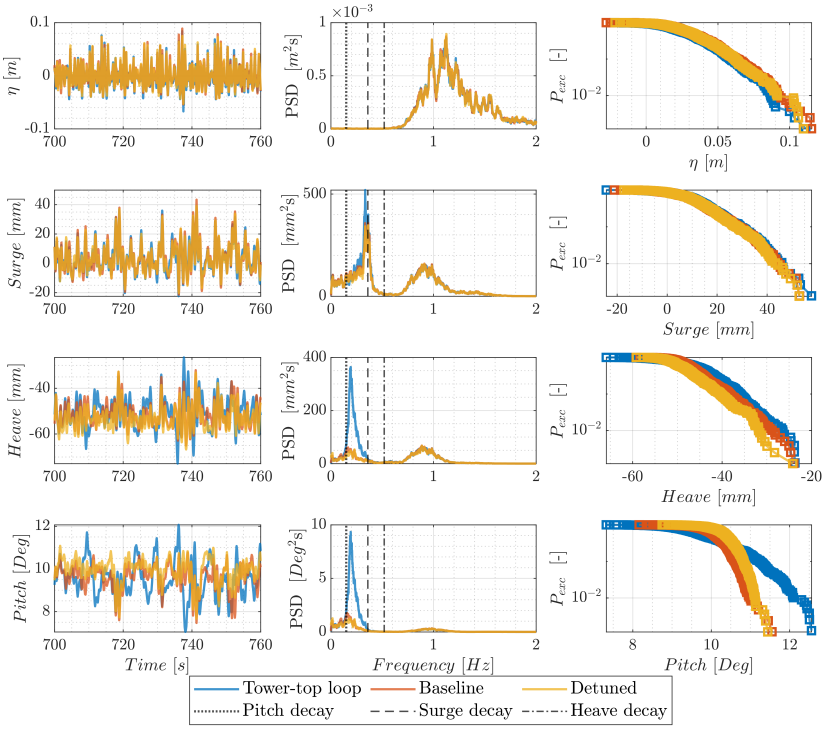

Figure 6.27: Floater response to irregular waves and wind forcing under the three controllers for EC 5. Time-series, power spectra and exceedance probability.

In Figure 6.28 the wind speed, rotor speed and total blade pitch angle are presented together with their corresponding power spectra and exceedance probability plots for all controllers. Note that the generator torque has not been included because it is constant above rated due to the chosen full-load control strategy.

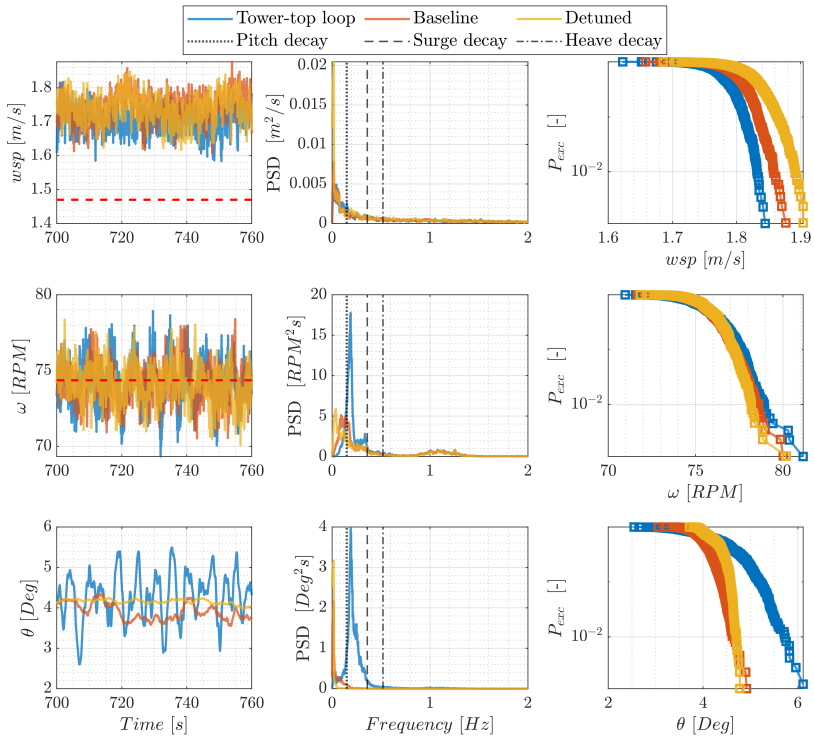

Figure 6.28: Turbine operational data in irregular waves and wind forcing under the three controllers for EC 5. Time-series, power spectra and exceedance probability.

Taking a look into the time-series signals, there seem to be higher oscillations in both the rotor speed and blade pitch angle for the tower-top loop controller, mainly driven by the floater pitch motion as seen in the power spectra plots. Regarding the rotor speed power spectra, while the detuned controller shows an important contribution from the wind power spectrum, the baseline controller presents a higher contribution around the floater pitch natural frequency. All of the controllers show a minor contribution from the waves power spectrum and the 1P frequency. The blade pitch angle is mainly dominated by the wind power spectrum for both the baseline and detuned controller, whereas it is hugely dominated by the pitch natural frequency for the tower-top loop controller. The aggressiveness of the tower-top loop controller can be seen easily, as it pitches the blades more than the baseline controller, confirmed in the exceedance probability plot. The effect of the aggressive pitching of the blades for the tower-top loop controller causes likewise the rotational speed to achieve the highest values. Note how the detuned controller keeps the blade pitch more constant than the baseline controller, since it is slower reacting to changes in the wind speed.

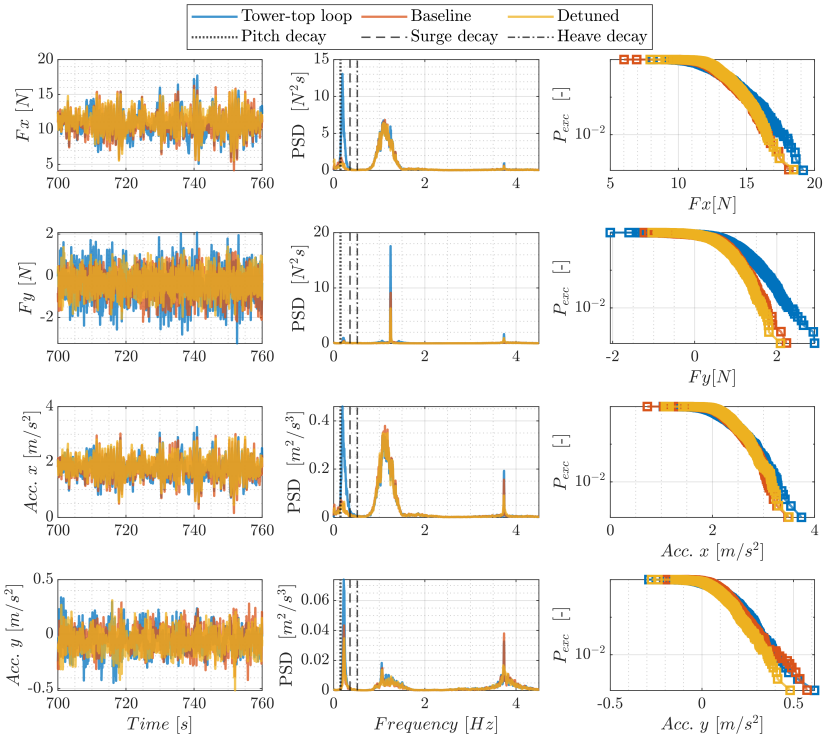

Figure 6.29: Tower-top fore-aft (x) and side-side (y) shear forces and accelerations in irregular waves and wind forcing under the three controllers for EC 5. Time-series, power spectra and exceedance probability.

In Figure 6.29 the tower-top fore-aft (x) and side-side (y) shear forces and accelerations are presented together with their corresponding power spectra and exceedance probability plots for the three controllers. The mean value of the time-series are almost identical, but the higher oscillations experienced for the tower-top loop controller can be identified in the exceedance probability plots. With regards to the fore-aft shear force and acceleration PSD plots, the response under the tower-top loop controller is mainly dominated by a range of frequencies with a peak around the pitch natural frequency with a lower contribution from the wave range and the 3P frequency, whereas the response under the other two controllers is mostly dominated by the frequencies around the wave range with a minor contribution from the wind spectra, the pitch natural frequency and the 3P frequency. The side-side shear forces are mainly dominated by a peak at the 1P frequency together with a minor contribution from another peak at the 3P frequency for all the controllers, while the accelerations are predominantly dominated by a range of frequencies around the roll natural fre-

quency. Lastly, a lower energy content is seen around the wave spectrum frequencies, a peak at the 3P frequency and around the assumed tower natural frequency of 4 H.z.

Figure 6.30 shows the time-series, the power spectra and the exceedance probability plots for the three mooring lines under the three different controllers. In this case, the behaviour of the controllers seems to be quite similar. As expected ML1 experiences the highest tensions, since the line is aligned with the wind and waves while the other two lines experience lower tensions, as a result of the misalignment with the wind and wave forcing. In general trends, the mooring lines response are mainly driven by the floater surge natural frequency and a range of frequencies around the wave spectrum frequencies, as seen in the PSD plots. However, an important energy content is seen around the pitch natural frequency for the tower-top loop controller, which indicates the strong coupling between the surge and pitch motion. Looking at the exceedance probability plots, it is interesting to see how the tensions are normally larger for the tower-top loop controller due to the higher pitch and surge motion.

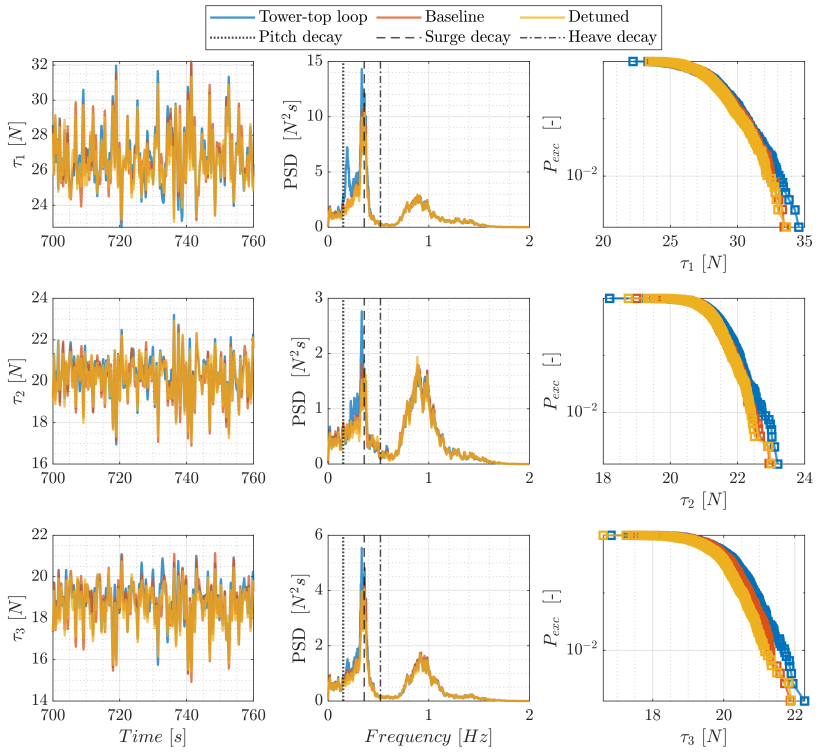

Figure 6.30: Mooring lines response to irregular waves and wind forcing under the three controllers for EC 5. Time-series, power spectra and exceedance probability.

Figure 6.31 presents the standard deviation of the ECs seen in Table 6.2 without wave misalignment. The calculations are done for the two main controllers of study: the baseline controller (A_003) and the tower-top loop controller (D_008). A transient time of 5 minutes was discarded when calculating the standard deviations.

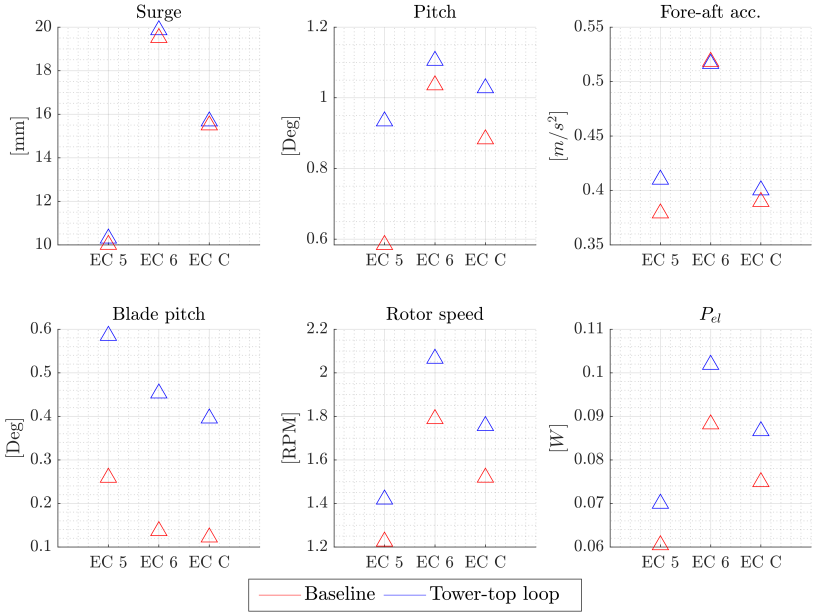

Figure 6.31: Standard deviation for surge, pitch, tower-top fore-aft acceleration, blade pitch, rotor speed and electrical output power for several ECs and the two controllers of study.

First of all, even though the wind speeds for EC 6 and EC C were the same due to limitations related to the wind maker, both the surge and pitch standard deviation are larger for EC 6 under the two controllers. As a consequence of the waves being larger for EC 6, the hydrodynamic forces acting on the floater create a larger moment opposing to the mean pitch moment created by the wind, and hence the larger the oscillations for both the surge and pitch. Following the same reasoning, EC5 presents the lowest standard deviation for both the surge and pitch as it represents the lowest sea state. Now, focusing on the different performances of the two controllers, the tower-top loop controller presents higher oscillations for all the considered cases. Particularly remarkable is the big difference seen for the EC 5 pitch standard deviation. This is the case in which the pitch instability is more critical resulting in higher oscillations for a fast controller as the tower-top loop one. For EC 6 and EC C, for which the thrust curve gradient is lower, the pitch instability is lower, and hence the standard deviations. The tower-top fore-aft acceleration presents a similar behaviour

to the pitch standard deviation as the larger waves cause larger pitch oscillations and hence larger acceleration oscillations.

In terms of wind turbine operational parameters, the blade pitch angle standard deviation is the highest for EC 5 and lower for EC 6 and EC C. The blade pitch angle change is mainly driven by the wind speed seen by the rotor blades, which strongly depends on the fore-aft tower motion. Since the fore-aft tower motion is the highest just above rated, the standard deviation of the blade pitch angle is the highest. The same happens between EC 6 and EC C. The wind speed is identical, but the waves are larger for EC 6, which introduces a higher fore-aft tower motion, eventually leading to a slightly higher blade pitch angle change. The new tower-top loop controller has a more aggressive behaviour than the baseline controller, as evidenced by the higher standard deviations in the blade pitch, ultimately causing the same in the rotor speed. However, the rotor speed standard deviation is higher for cases in which the sea states are larger, meaning that the effect of the sea states has a bigger influence than the effect of the pitch instability triggered by the wind speed just above rated. The electrical output power has been calculated as the product of the generator torque times the rotor speed. It is therefore expected that the output electrical power presents the same behaviour as the rotor speed standard deviation, since a constant torque strategy is followed above rated.

In order to allow for a more in-depth analysis of the controller performances, the mean, the standard deviation, the maximum and the 90^{th} percentile of the main logged signals for the two different controllers of study have been calculated for all the ECs shown in Table 6.2. Again, an initial transient of 5 minutes has been discarded. Table 6.3 - 6.5 list the results for EC 5, EC 6 and EC C, respectively. Looking first at the mean values, it can be seen that both controllers result in very similar values. The tower-top loop controller results in a higher mean surge, while the mean floater pitch is slightly lower than for the baseline controller. However, the differences remain under 5%, except for the surge of EC C, which shows a deviation of around 10%. The mean values of the tower-top accelerations and shear forces are almost identical for both controllers, the same applies for the mooring line tension. Furthermore, both controllers result in the same mean power output. Regarding the standard deviations, the tower-top loop controller generally shows slightly larger values, as it was already seen in Figure 6.31. The biggest difference occurs in the floater pitch angle, the blade pitch angle and the rotational speed. Across the different sea states, EC 5 shows the biggest difference between the two controllers. While the tower-top loop controller shows higher standard deviations and therefore higher structural responses, these differences are relatively small, especially for EC 6 and EC C. In the case of EC C, the standard deviations of the mooring lines are even slightly smaller for the new controller than for the baseline controller.

Due to the higher oscillations of the tower-top velocity loop controller, the maximum values are also slightly higher for most quantities. This is again especially the case for the floater pitch, the blade pitch angle and the rotational speed. Both controllers seem to experience occasional overshoots in the rotational speed, which are

slightly higher for the tower-top loop controller. The 90^{th} percentiles shows a similar picture as the standard deviations with slightly higher values for the tower-loop controller, indicating higher oscillations of the system.

Table 6.3: Main statistical parameters of the main logged signals under the two controllers of study for EC 5.

	EC 5							
	Mean		Standard deviation		Maximum		$90^{th} PC$	
	A_003	D_008	A_003	D_008	A_003	D_008	A_003	D_008
Surge [mm]	2.79	2.95	10.01	10.30	52.96	57.74	15.69	16.05
Pitch [Deg]	9.70	9.58	0.58	0.93	11.55	12.56	10.34	10.80
Fx [N]	10.71	10.86	1.58	1.80	18.11	19.17	12.80	12.99
Fy [N]	-0.38	-0.43	0.65	0.83	2.23	2.92	0.44	0.64
Acc. x [m/s^2]	1.78	1.75	0.38	0.41	3.48	3.74	2.23	2.27
Acc. y [m/s^2]	-0.04	-0.05	0.10	0.12	0.57	0.61	0.09	0.09
ω [RPM]	74.16	74.16	1.23	1.42	80.02	81.16	75.73	75.97
θ [Deg]	4.02	4.23	0.26	0.59	4.92	6.11	4.35	4.95
ML1 [N]	26.61	26.77	1.49	1.63	32.81	33.84	28.54	28.86
ML2 [N]	20.10	20.20	0.94	0.99	23.12	23.59	21.18	21.36
ML3 [N]	18.80	18.92	0.98	1.04	21.49	21.84	19.97	20.17
P_{el} [W]	3.65	3.65	0.06	0.07	3.94	4	3.74	3.73

Table 6.4: Main statistical parameters of the main logged signals under the two controllers of study for EC 6.

	EC 6							
	Mean		Standard deviation		Maximum		90^{th} PC	
	A_003	D_008	A_003	D_008	A_003	D_008	A_003	D_008
Surge [mm]	9.57	9.77	19.51	19.86	97.61	97.78	35.44	36.03
Pitch [Deg]	9.70	9.58	1.04	1.11	10.16	11.01	8.84	9.21
Fx [N]	8.59	8.80	2.23	2.30	18.28	18.29	11.49	11.79
Fy [N]	-0.85	-0.83	0.94	0.98	2.92	2.23	0.35	0.42
Accx [m/s^2]	1.43	1.51	0.52	0.52	3.74	3.48	2.09	2.17
Accy [m/s^2]	-0.08	-0.07	0.13	0.13	0.49	0.58	0.09	0.09
ω [RPM]	74.16	74.16	1.79	2.07	81.88	82.91	76.44	76.82
θ [Deg]	8.59	8.61	0.14	0.45	9.10	9.94	8.77	9.18
ML1 [N]	26.66	26.73	2.99	3.06	39.29	40.13	30.54	30.68
ML2 [N]	19.75	19.76	1.83	1.90	24.05	24.01	21.90	21.98
ML3 [N]	18.50	18.60	1.87	1.86	23.23	23.60	20.75	20.81
P_{el} [W]	3.65	3.65	0.08	0.1	4.03	4.08	3.78	3.77

Table 6.5: Main statistical parameters of the main logged signals under the two controllers of study for EC C.

	EC C							
	Mean		Standard deviation		Maximum		90^{th} PC	
	A_003	D_008	A_003	D_008	A_003	D_008	A_003	D_008
Surge [mm]	3.80	4.29	15.49	15.68	97.61	97.78	24.27	23.43
Pitch [Deg]	8.15	8.12	0.88	1.03	10.19	11.18	9.29	9.05
Fx [N]	8.75	8.82	1.70	1.80	16.29	16.77	11.03	10.82
Fy [N]	-0.84	-0.84	0.91	0.90	2.67	2.39	0.30	0.32
Accx [m/s^2]	1.49	1.51	0.39	0.40	3.20	3.42	2.01	1.97
Accy [m/s^2]	-0.07	-0.09	0.10	0.10	0.36	0.35	0.05	0.06
ω [RPM]	74.16	74.16	1.52	1.76	80.91	81.05	76.39	76.10
θ [Deg]	8.64	8.71	0.12	0.40	9.06	9.91	9.21	8.80
ML1 [N]	26.19	26.04	2.49	2.47	39.21	39.00	29.29	29.43
ML2 [N]	20.03	20.07	1.68	1.60	24.36	23.94	21.96	21.97
ML3 [N]	18.82	18.80	1.53	1.55	22.34	22.15	20.61	20.62
P_{el} [W]	3.65	3.65	0.075	0.08	3.99	3.99	3.73	3.76

In general, the baseline can be considered to perform slightly better under the conducted irregular waves and wind tests. However, it should be pointed out that the tested conditions were somewhat limited. Only tests under normal operational conditions with low turbulence intensity were carried out. The low turbulence intensity of approximately 3% is a result of the wind generator in the test facilities. In a real-world application, significantly higher turbulence intensities can be expected. It is reasonable to expect that the performance of the faster tower-top loop controller would improve compared to the slower baseline controller for higher turbulence intensities. This was also indicated by the smaller rotational speed overshoot of the new controller in the step wind test. Furthermore, special cases like an extreme wind gust or a loss of the electrical grid were not tested in this campaign. It can be expected that a faster controller could cope better with these extreme events and reduce the resulting extreme loads. However, further tests would be necessary in order to confirm these assumptions.

CHAPTER 7

Conclusion

In this Master's Thesis, a new control strategy for a floating offshore wind turbine (FOWT) was developed and tested at the test facilities of Danish Hydraulic Institute (DHI). The main goal of the new controller is avoiding the so-called pitch instability, while being a faster controller than a conventional offshore controller. The lab-scale model consisted of the 1:60 DTU 10 MW Reference Wind Turbine (RWT) mounted on the TetraSub concept foundation designed and provided by Stiesdal Offshore Technologies (SOT). First, a theoretical overview of dynamic modelling and loads analysis of a FOWT together with the classical control strategies used in most conventional wind turbines was presented. The novel control strategy requires the tower velocity as an input to the controller, and hence two different approaches to get this velocity from the physical model were numerically pre-simulated: the differentiation of the floater motion and the integration of an accelerometer attached to the tower-top of the lab-scale model. Then, in order to make a first assessment of the new controller strategy before the experimental campaign started, different controllers were numerically simulated in the aero-hydro-servo-elastic code HAWC2. The numerical simulations showed that the new tower velocity loop is capable of stabilizing a previously unstable controller.

Next, a short description of both the 1:60 DTU 10 MW RWT model and the TetraSub concept foundation model was given. Likewise, the way the mooring line system was designed and installed in the wave basin was presented, together with a scheme of the wave basin. Since the small-scale floating wind turbine model was intended to be tested under real-life operating conditions, the facilities were equipped with a wind generator and a wave maker, which were briefly presented and described. Furthermore, the set of environmental conditions (ECs) planned to tested in the lab were presented. Lastly, the data acquisition (DAQ) system as well as the measuring equipment used during the whole experimental campaign were explained.

Before conducting the production tests, the ECs had to be calibrated and compared to the target values. First, the wind field produced by the wind generator was calibrated. The maximum mean wind speed at the rotor area resulted to be around 2.2 m/s at hub height, which indeed set a limit for the target ECs, and consequently it was decided to use this maximum wind speed for those ECs in which the targeted wind speed was higher. In the same way, the turbulence intensity was also documented, showing low values of around 3% for most parts of the rotor plane.

The wave maker was able to generate regular, irregular and focused waves. Furthermore, by turning the wave field using the directional wave maker, some climates were also tested with a wave misalignment with respect to the wind direction. The irregular waves calibration resulted in deviations from the target values between 0.19% - 14.32% for the wave height and 0.59% - 7.97% for the wave period. For the regular wave cases an almost perfect match was found for the wave period, with a maximum deviation of 0.81%. For the wave heights the deviations ranged from 0.6% to 47.15%. Bearing in mind the high number of sea states that were calibrated and the fact that there were some very small sea states, for which a small deviation in absolute values results in a very large relative deviation, the results were considered to be acceptable.

Before running any production tests, the aerodynamic performance of the fixed lab-scale wind turbine was recorded. Slight differences, specially shown as a constant offset in the pitch angle, were found with respect to previous experimental campaigns. Several issues such as the manual mounting process of the blades, excessive friction in the gear system or difference in the ambient temperature were discussed as potential reasons for these differences. Then, the turbine was mounted on the TetraSub concept foundation and free decay tests were performed for all 6 DoF of the floater motion in order to determine both the structural natural frequencies and damping ratios. For some extreme sea states, the heave natural frequency coincided with their peak period. However, since the floater heave plates typically dampen out the motion significantly, a potential heave resonance was considered as acceptable.

As the focus of this thesis was to develop and test a new controller for a FOWT, two different controllers were tuned for the physical small-scale floating wind turbine model. First, a slow conventional offshore wind turbine controller was tuned by trial and error. In order to tune this controller, wind step tests were performed for the wind turbine. The main design criterion was finding the fastest controller that could cope with the pitch instability of the wind turbine above rated wind speed. The resulting controller, denoted as the baseline controller, was found to be stable for a closed-loop frequency of 0.15 Hz. Any higher closed-loop frequency lead to pitch instability above rated. Once the baseline controller was defined, the next objective was to obtain a faster controller, which was able cope with the pitch instability by use of the new tower-top velocity loop. For that purpose, constant wind tests were conducted for the most critical wind speed, i.e. just above rated, to tune the controller parameters. This new controller included the contribution from the tower-top velocity, and hence it was tuned by modifying a tower-top gain and the new closed-loop frequency. Finally, a controller with a closed-loop frequency of 0.35 Hz was proven to be able to bring the system back to stability from instability. The new developed controller is referred to as the tower-top loop controller.

A detailed analysis of the wave-only tests was carried out, including regular waves, irregular waves and focused waves. The results showed a high pitch flexibility of the floater, with only small motion in surge. The tower-top fore-aft acceleration was strongly dominated by the natural pitch frequency, which was confirmed to be at the

measured value of 0.15 Hz from the decay tests. The same applies for the side-side acceleration and the natural roll frequency. No excessive heave motion was detected, despite the natural heave frequency coinciding with the peak frequency of the extreme sea states, which confirms a strong damping of the heave motion due to the heave plates. However, a strong coupling between heave and pitch motion could be seen in the analysis. The mooring line tension was mainly dominated by the natural surge frequency of 0.36 Hz measured in the decay tests. The harmonic decomposition of the wave-only tests proved a strong influence of subharmonics on the floater motion, which highlights the importance of higher-order wave effects on the floater dynamics.

The analysis of production tests with wind included showed that the aerodynamic thrust is causing a very large mean pitch angle of the floater, confirming the high pitch flexibility detected in the wave-only tests. The floater pitch angle reached values over 10° for tests around rated wind speed. A pitch angle of this magnitude is usually not desired in FOWT, however it should be noted that the deployed TetraSub concept foundation was not specifically designed and optimized for the DTU 10 MW RWT, which could be a cause for the unusual high floater pitch angle. By analyzing the step wind tests, typical curves for power, rotational speed and blade pitch angle could be obtained. Rated rotor speed was achieved at the expected rated wind speed and the controller successfully limited the rotor speed to its rated value while keeping the torque constant, therefore achieving the main control objectives.

The frequency analysis of the wind and wave tests yielded similar results as the wave-only tests, with additional energy content at the 1P and 3P frequency. Moreover, the peaks at the natural pitch frequency were a bit less pronounced, but additional energy contribution could be seen at very low frequencies due to the wind excitation. As a result of the high mean pitch angle, the natural frequency in pitch and roll seemed to be slightly shifted towards higher values. The effects of wave misalignment were also investigated.

The controller performance analysis showed that the faster controller, with the new tower-top velocity loop included, performs on a similar level as the slow detuned baseline controller. It was therefore successfully proven that the additional tower-velocity loop is able to stabilize a previously unstable controller. The tower-velocity loop thus allows the deployment of a faster controller for FOWTs, without introducing the described problem of pitch instability. The benefit of the faster controller could be seen in the step-wind tests, in which the new tower-top controller resulted in significant smaller overshoots of the rotational speed than the baseline controller.

From the detailed analysis of the production tests it was concluded that the structural response of the turbine is slightly higher for the baseline controller than for the novel tower-top loop controller. This results in higher standard deviations of the majority of measured quantities for the tower-top loop controller. However, the difference is very small in most cases. The biggest deviations can be seen in the floater pitch, blade pitch angle and rotor speed for EC 5, which had a wind speed just above rated. But even in this case, the differences in the standard deviations are relatively small with 0.35° for the floater pitch, 0.33° for the blade pitch angle and 0.19 RPM

for the rotational speed. For ECs with higher wind speeds the differences are even smaller. The analysis also showed that the power output is not negatively affected by the new controller, with the mean power output being identical to the baseline controller and the standard deviation showing only a very minor increase.

It should also be considered that in this test campaign, the controllers were only tested under normal operational conditions with an unusual low turbulence intensity of around 3%. Under real-world conditions, a significantly higher turbulence intensity can be expected. The faster tower-top loop controller is likely to cope better with an increased turbulence than the slow detuned controller. Furthermore, no ultimate load events like an extreme coherent wind gust or a loss of the electrical grid were tested. Nevertheless, these extreme design load cases are also an important aspect of wind turbine design. It can be expected that the faster tower-top loop controller could react faster to these extreme events and would result in lower ultimate loads than the slow baseline controller.

Additionally, it should be pointed out that the controller was only tested with one specific floater model. The performance of the controllers might differ when using a different floater type, especially when considering the unusual high pitch motion of the deployed floater concept. Due to the very small difference in the controller performances, one should be careful in drawing definite conclusions about the performances between the baseline and the new tower-top loop controller. It also cannot be excluded that scaling effects are influencing the controller performance, compared to a full-scale model.

Future work

An important next step in the presented project is the numerical modelling and re-simulation of the conducted tests. The creation and validation of a sound numerical model, through a successful re-simulation of the tests, would allow for further analysis of the new controller strategy. The numerical model then could be used to simulate the new controller in different conditions than the ones applied during the measurement campaign. Simulating cases like an extreme wind gust could give additional insight into the controller behavior and performance.

A validated numerical model of the floating wind turbine and the controller would also allow to test a larger number of different controller parameters. In the presented work, the controller parameters were tuned experimentally by trial-and-error runs. Naturally, this procedure does not guarantee the optimal combination of parameters. Not only the proportional and integral gain of the pitch controller must be defined, but also the new tower-top velocity gain could be chosen differently. Different combinations of these parameters might result in different controller performances.

The objective in the controller tuning procedure in this campaign was to obtain the fastest possible controller, which can be stabilized by the new tower-velocity loop. An interesting point of study would be to implement the new tower-velocity loop into a controller, which is slower than new controller tested in this campaign, but still faster than the baseline controller.

On an experimental level, it would be interesting to deploy the new controller strategy in different floater types and investigate if similar conclusions can be drawn as the ones presented in this thesis.

Bibliography

[1] "Paris Agreement," *United Nations Treaty Collection, Chapter XXVII 7. d*, pp. 58 – 76, 2015.

[2] "Reaching zero with renewables: Eliminating CO2 emissions from industry and transport in line with the 1.5 °C climate goal," tech. rep., IRENA, 2020.

[3] W. Europe, "Offshore Wind in Europe: Key trends and statistics 2020," tech. rep., 02 2021.

[4] "Offshore Wind Outlook 2019," tech. rep., IEA, 2019.

[5] "Floating Foundations: a Game Changer for Offshore Wind Power," tech. rep., IRENA, 2016.

[6] Equinor, "Equinor and ORE Catapult collaborating to share Hywind Scotland operational data." `https://www.equinor.com/en/news/2019-11-28-hywind-scotland-data.html`, 2019.

[7] GE, "Haliade-X offshore wind turbine." `https://www.ge.com/renewableenergy/wind-energy/offshore-wind/haliade-x-offshore-turbine`.

[8] S. Gamesa, "SG14 - 222 DD." `https://www.siemensgamesa.com/en-int/products-and-services/offshore/wind-turbine-sg-14-222-dd`.

[9] "Floating Offshore Wind Vision Statement," tech. rep., WindEurope, 2017.

[10] Equinor, "Hywind Scotland." `https://www.equinor.com/en/what-we-do/floating-wind/hywind-scotland.html`.

[11] E. Renewables, "Windfloat Atlantic." `https://www.edp.com/en/innovation/windfloat`.

[12] R. Proskovics, "Floating Offshore Wind: A Situational Analysis," tech. rep., 10 2018.

[13] I. Komušanac, "Wind energy in Europe in 2019: Trends and statistics," tech. rep., 02 2020.

[14] H. Nguyen and D. Naidu, *Evolution of Wind Turbine Control Systems*. 01 2013.

[15] J. Olondriz Erdozain, I. Elorza, C. Calleja, J. Jugo, and A. Pujana-Arrese, "Advanced Control For Floating Offshore Wind Turbine," 03 2017.

[16] "Danish research to strengthen the design of floating wind turbines." `https://www.vindenergi.dtu.dk/english/news/2018/10/danish-research-to-strengthen-the-design-of-floating-wind-turbines?id=23405be2-139c-4db2-9411-d1ab57949294`, 2018.

[17] M. H. Hansen and L. C. Henriksen, "Basic DTU Wind Energy Controller," tech. rep., DTU Wind Energy, 2013.

[18] B. Skaare, T. Hanson, F. Nielsen, R. Yttervik, A. Hansen, K. Thomsen, T. Larsen, B. Skaare@hydro, No, T. David, F. No, Gunnar, R. Com, A. No, and Melchior, "Integrated dynamic analysis of floating offshore wind turbines," *European Wind Energy Conference and Exhibition*, 01 2007.

[19] A. Goupee, B. Koo, R. Kimball, K. Lambrakos, and H. Dagher, "Experimental Comparison of Three Floating Wind Turbine Concepts," vol. 136, 07 2012.

[20] K. Kai, K. Takuya, O. Makoto, N. Akihiro, I. Satoshi, H. Yoshi-yuki, and H. Akihiro, "Wind Tunnel Testing on Negative-damped Responses of a 7MW Floating Offshore Wind Turbine," 2015.

[21] A. J. Goupee, R. W. Kimball, and H. J. Dagher, "Experimental observations of active blade pitch and generator control influence on floating wind turbine response," *Renewable Energy*, vol. 104, pp. 9–19, 2017.

[22] A. M. Hansen, R. Laugesen, H. Bredmose, R. Mikkelsen, and N. Psichogios, "Small scale experimental study of the dynamic response of a tension leg platform wind turbine," *Journal of Renewable and Sustainable Energy*, vol. 6, no. 5, p. 053108, 2014.

[23] H. Bredmose, R. Mikkelsen, A. M. Hansen, R. Laugesen, N. Heilskov, B. Jensen, and J. Kirkegaard, "Experimental study of the DTU 10 MW wind turbine on a TLP floater in waves and wind," 2015. EWEA Offshore 2015 Conference ; Conference date: 10-03-2015 Through 12-03-2015.

[24] R. F. Mikkelsen, "The DTU 10MW 1:60 model scale wind turbine blade," tech. rep., DTU Wind Energy.

[25] F. Madsen, T. Nielsen, T. Kim, H. Bredmose, A. Pegalajar-Jurado, R. Mikkelsen, A. Lomholt, M. Borg, M. Mirzaei, and P. Shin, "Experimental analysis of the scaled DTU 10 MW TLP floating wind turbine with different control strategies," *Renewable Energy*, vol. 155, pp. 330–346, 2020.

[26] H. Bredmose, F. Lemmer, M. Borg, A. Pegalajar-Jurado, R. Mikkelsen, T. Stoklund Larsen, T. Fjelstrup, W. Yu, A. Lomholt, L. Boehm, and J. Azcona Armendariz, "The Triple Spar campaign: Model tests of a 10MW floating wind turbine with waves, wind and pitch control," *Energy Procedia*, vol. 137, pp. 58 – 76, 2017.

[27] A. Pegalajar-Jurado, *Cascaded numerical models for offshore floating wind turbines*. PhD thesis, Technical University of Denmark, 2019.

[28] R. James and M. Costa Ros, "Floating Offshore Wind:Market and Technology Review," tech. rep., 6 2015.

[29] M. Leimeister, A. Kolios, and M. Collu, "Critical review of floating support structures for offshore wind farm deployment," *Journal of Physics: Conference Series*, vol. 1104, p. 012007, 10 2018.

[30] Equinor, "Hywind Tampen." `https://www.equinor.com/en/what-we-do/hywind-tampen.html`.

[31] T. Ishihara, M. B. Waris, and H. Sukegawa, "A study on influence of heave plate on dynamic response of floating offshore wind turbine system," 01 2009.

[32] COBRA, "Kincardine Offshore Floating Wind." `https://www.grupocobra.com/en/proyecto/kincardine-offshore-floating-wind-farm/`.

[33] M. V. O. Wind, "Eoliennes Flottantes du golfe du Lion (EFGL) Selects V164-10.0 MW turbines from MHI Vestas Offshore Wind." `https://mhivestasoffshore.com/eoliennes-flottantes-du-golfe-du-lion-efgl-selects-v164-10-0-mw-turbines-from-mhi-vestas-offshore-wind/`.

[34] K. G. Vijay, D. Karmakar, E. Uzunoglu, and C. Guedes Soares, *Performance of barge-type floaters for floating wind turbine*, pp. 637 – 645. 10 2016.

[35] Ideol, "Floatgen demonstarator." `https://www.ideol-offshore.com/en/floatgen-demonstrator`.

[36] A. Buljan, "EolMed Floating Wind Project to Feature MHI Vestas 10 MW Turbines." `https://www.offshorewind.biz/2020/10/05/eolmed-floating-wind-project-to-feature-mhi-vestas-10-mw-turbines/`.

[37] M. Kausche, F. Adam, F. Dahlhaus, and J. Großmann, "Floating offshore wind - Economic and ecological challenges of a TLP solution," *Renewable Energy*, vol. 126, pp. 270–280, 2018.

[38] G. Kuik and J. Peinke, *Long-term Research Challenges in Wind Energy - A Research Agenda by the European Academy of Wind Energy*, vol. 6. 01 2016.

[39] R. James, W.-Y. Weng, C. Spradbery, J. Jones, D. Matha, A. Mitzlaff, R. V. Ahilan, M. Frampton, and M. Lopes, "Floating Wind Joint Industry Project - Phase I Summary Report: Key findings from electrical systems, mooring systems, and infrastructure logistics studies.," tech. rep., Carbon Trust, 2018.

[40] D. K. Spearman, S. Strivens, C. Spradbery, N. Cosack, D. Matha, A. Macleay, J. Regelink, D. Patel, and T. Walsh, "Floating Wind Joint Industry Project - Phase II Summary Report," tech. rep., Carbon Trust, 2020.

[41] A. Pegalajar-Jurado, "Course notes: 46111 Offshore Wind Energy. Floating Wind Turbines II: Modelling, analysis and design," November 2020.

[42] J. Jonkman, "Dynamics modeling and loads analysis of an offshore floating wind turbine," tech. rep., 11 2007.

[43] H. Bredmose, "Course notes: 46111 Offshore Wind Energy. Linear Wave Theory," October 2020.

[44] P. A. Madsen, "Course notes: 41224 Linear Wave Dynamics. Fall 2019," 2019.

[45] A. Pegalajar-Jurado, "Course notes: 46111 Offshore Wind Energy. Floating Wind Turbines IV: Station keeping," November 2020.

[46] M. O.L.Hansen, *Aerodynamics of Wind Turbines*, ch. 7, p. 54. Routledge, 2015.

[47] F. Meng, A. W. H. Lio, and J. Rinker, "Course notes 46320: Loads, Aerodynamics and Control of Wind Turbines. Derivation of control equations in Region 1, 2 and 3," October 2020.

[48] F. Meng and A. W. H. Lio, "Lecture slides 46320: Loads, Aerodynamics and Control of Wind Turbines. Controller Tuning," October 2020.

[49] G. J. van der Veen, I. J. Couchman, and R. O. Bowyer, "Control of floating wind turbines," in *2012 American Control Conference (ACC)*, pp. 3148–3153, 2012.

[50] B. Fischer, "Reducing rotor speed variations of floating wind turbines by compensation of non-minimum phase zeros," *Renewable Power Generation, IET*, vol. 7, pp. 413–419, 07 2013.

[51] P. Dutilleux, M. Holters, S. Disch, and U. Zölzer, *Filters and Delays*, ch. 2, pp. 47–81. John Wiley Sons, Ltd.

[52] F. J. Madsen, T. R. Nielsen, H. Bredmose, M. Borg, A. Pegalajar-Jurado, and A. K. Lomholt, "Scaled TetraSpar Flooting Wind Turbine HAWC2 Model Report," tech. rep., December 2017.

[53] H. Bredmose, M. Borg, A. Pegalajar-Jurado, T. R. Nielsen, F. J. Madsen, A. K. Lomholt, R. Mikkelsen, and M. Mirzaei, "TetraSpar Flooting Wind Turbine Scale Model Testing Summary Report," tech. rep., August 2017.

[54] C. Bak, F. Zahle, R. Bitsche, T. Kim, A. Yde, L. Henriksen, M. Hansen, J. Blasques, M. Gaunaa, and A. Natarajan, "The DTU 10-MW Reference Wind Turbine," 2013. Danish Wind Power Research 2013 ; Conference date: 27-05-2013 Through 28-05-2013.

[55] H. Bredmose, A. Pegalajar-Jurado, A. M. Hansen, R. Laugesen, R. F. Mikkelsen, M. Borg, T. Kim, and N. Heilskov, "Experimental and numerical study of a 10MW TLP wind turbine in waves and wind," 2016. The Science of Making Torque from Wind 2016 ; Conference date: 05-10-2016.

[56] J. Newman, *Marine Hydrodynamics. 40th Anniversary Edition*. 2017.

[57] H. Bredmose, S. Larsen, D. Matha, A. Rettenmeier, E. Marino, and L. Saettran, *Collation of offshore wind wave dynamics*. 01 2012.

[58] R. Laugesen and A. M. Hansen, "Experimental Study of the Dynamic Response of the DTU 10 MW Wind turbine on a Tension Leg Platform, Eksperimentelt studie af det dynamiske respons af DTU 10 MW vindmøllen på en "Tension Leg Platform," 2015.

[59] A. Pegalajar-Jurado, A. Hansen, R. Laugesen, R. Mikkelsen, M. Borg, T. Kim, N. Heilskov, and H. Bredmose, "Experimental and numerical study of a 10MW TLP wind turbine in waves and wind," *Journal of Physics: Conference Series*, vol. 753, p. 092007, 09 2016.

[60] H. Wang, G. MA, L. Sun, and Z. Kang, "Truncation Design and Model Testing of a Deepwater FPSO Mooring System," *Journal of Offshore Mechanics and Arctic Engineering*, vol. 138, 01 2016.

[61] T. S. Larsen and T. Fjelstrup, "Experimental study of a triple spar floating wind turbine in wind and wave forcing, Eksperimentelt studie af en triple spar flydende vindmølle i bølger og vind," 2016.

[62] F. Johannes Madsen and T. Raahauge Lund Nielsen, "Experimental and numerical study of the scaled DTU 10MW floating wind turbine on a TLP platform," 2017.

[63] A. K. Lomholt and L. Boehm, "Implementation of a Modelscale Floating Wind Turbine Pitch-Generator Control, Implementering af Pitch-Generator styring for en Flydende Modelskala Vindmølle," 2016.

[64] J. Zelt and J. E. Skjelbreia, "Estimating Incident and Reflected Wave Fields Using an Arbitrary Number of Wave Gauges," *Coastal Engineering Proceedings*, October 1992.

[65] A. M. Pegalajar Jurado, "Numerical reproduction of laboratory experiments for a tlp wind turbine, numerisk reproduktion af laboratoriemålinger af en tlp vindmølle," 2015.

[66] C. Fitzgerald, P. Taylor, R. Eatock Taylor, J. Grice, and J. Zang, "Phase manipulation and the harmonic components of ringing forces on a surface-piercing column.," vol. 470, May 2014.

[67] S. E. Steffensen, "Experimental and numerical study of the damping effect from heave plates on teh response of floating offshore wind turbines in operational sea states.," August 2020.

[68] M. O.L.Hansen, *Aerodynamics of Wind Turbines*, ch. 9, p. 76. Routledge, 2015.

[69] G. K. V. Kumari Ramachandran, *A Numerical Model for a Floating TLP Wind Turbine*. PhD thesis, Queensland University of Technology, 2013.

[70] H. Bredmose and F. Pierella, "Course notes: 46111 Offshore Wind Energy. Forces from waves," October 2020.

[71] J. V. der Tempel, *Design of Support Structures for Offshore Wind Turbines*. PhD thesis, Technical University Delft, 2006.

[72] A. Pegalajar-Jurado, "Course notes: 46111 Offshore Wind Energy. Floating Wind Turbines III: Hydrodynamics and Control," November 2020.

APPENDIX A

Control theory

A.1 Optimal C_P tracking constant K

In this section the derivation of the optimal C_P-tracking constant K for the partial load control region is explained. The derivation is based on reference [47]. The aerodynamic power of a wind turbine is expressed as followed:

$$P_{aero} = P_{wind}\, C_P(\theta_{opt}, \lambda_{opt}) = \frac{1}{2}\,\rho\, A\, V^3\, C_P(\theta_{opt}, \lambda_{opt}) \tag{A.1}$$

Hereby λ_{opt} and θ_{opt} refer to the tip speed ratio and pitch angle, at which the optimal C_P is obtained. By applying the definition of the tip speed ratio $\lambda = \frac{\omega R}{V}$, P_{aero} can be expressed in the following form:

$$P_{aero} = \frac{\rho\, A\, R^3\, C_P(\theta_{opt}, \lambda_{opt})}{2\,\lambda_{opt}^3}\,\omega^3 \tag{A.2}$$

The aerodynamic power can also be expressed as the product of the aerodynamic torque Q_{aero} and the rotational speed ω:

$$P_{aero} = Q_{aero}\,\omega \tag{A.3}$$

Combining this with Eq. A.2 yields an expression for the aerodynamic torque:

$$Q_{aero} = \frac{\rho\, A\, R^3\, C_P(\theta_{opt}, \lambda_{opt})}{2\,\lambda_{opt}^3}\,\omega^2 \tag{A.4}$$

Assuming a generator efficiency η and no other losses, the generator power P_{gen} and generator torque Q_{gen} can be expressed as followed:

$$P_{gen} = \eta\, P_{aero} \tag{A.5}$$

$$n_g\,\omega\, Q_{gen} = \eta\,\omega\, Q_{aero} \tag{A.6}$$

$$Q_{gen} = Q_{aero}\,\frac{\eta}{n_g} \tag{A.7}$$

Hereby n_g represents the gear ratio between low speed and high speed shaft. Plugging expression (A.4) into expression (A.7) yields the final expression for the generator torque and the generator constant K:

$$Q_{gen} = \frac{\eta\,\rho\,A\,R^3\,C_P(\theta_{opt}, \lambda_{opt})}{2\,n_g\,\lambda_{opt}^3}\,\omega^2 = K\,\omega^2 \tag{A.8}$$

$$K = \frac{\eta\,\rho\,A\,R^3\,C_P(\theta_{opt}, \lambda_{opt})}{2\,n_g\,\lambda_{opt}^3} \tag{A.9}$$

A.2 Derivation of linear closed-loop controller equation of motion

This section explains the derivation of the linear equation of motion of the closed-loop controller system. The derivation is based on [47]. The starting point is the non-linear equation of motion of the drivetrain system:

$$I_{rotor}\,\ddot{\phi} = Q_{aero}(V, \omega, \theta) - \frac{1}{\eta}\,Q_{gen}(\omega) \tag{A.10}$$

Note that both $Q(V, \omega, \theta)$ and $Q_{gen}(\omega)$ are non-linear terms. In order to analyze the dynamics of the system properly, the equation is linearized around an operational point $op = (\omega_{rated}, V_{op}, \theta_{op})$. For simplicity the linearization is done around the operational point $\theta_{op} = 0$. Linearization is equivalent to a first-order Taylor expansion around the point of interest. Applying a Taylor expansion at the operational point leads to the following expressions:

$$\omega \approx \omega_{rated} + \Delta\omega = \omega_{rated} + \dot{\phi} \tag{A.11}$$

$$V \approx V_{op} + \Delta V \tag{A.12}$$

$$\theta \approx \theta_{op} + \Delta\theta \tag{A.13}$$

$$Q_{aero}(V, \omega, \theta) \approx Q_{aero}(V_{op}, \omega_{rated}, \theta_{op}) + \frac{\partial Q_{aero}}{\partial V}\Big|_0 \Delta V + \frac{\partial Q_{aero}}{\partial \omega}\Big|_0 \dot{\phi} + \frac{\partial Q_{aero}}{\partial \theta}\Big|_0 \Delta\theta \tag{A.14}$$

$$Q_{gen}(\omega) \approx Q_{gen}(\omega_{rated}) + \frac{\partial Q_{gen}}{\partial \omega}\Big|_0 \dot{\phi} \tag{A.15}$$

Furthermore it is known that at steady state ($\ddot{\phi} = 0$) and at the operational point the following relation applies:

$$I_{rotor}\,\ddot{\phi} = Q_{aero}(V_{op}, \omega_{rated}, \theta_{op}) - \frac{1}{\eta}\,Q_{gen}(\omega_{rated}) \tag{A.16}$$

$$Q_{aero}(V_{op}, \omega_{rated}, \theta_{op}) = \frac{1}{\eta} Q_{gen}(\omega_{rated}) \tag{A.17}$$

By applying Eqs. A.14, A.15 and A.17 to Eq. A.10, an expression for describing the dynamics of the closed-loop controller system around the operational point is obtained:

$$I_{rotor}\,\ddot{\phi} = \frac{\partial Q_{aero}}{\partial V}\Big|_0 \Delta V + \frac{\partial Q_{aero}}{\partial \omega}\Big|_0 \dot{\phi} + \frac{\partial Q_{aero}}{\partial \theta}\Big|_0 \Delta\theta - \frac{1}{\eta}\,\frac{\partial Q_{gen}}{\partial \omega}\Big|_0 \dot{\phi} \tag{A.18}$$

The change in wind speed in the term $\frac{\partial Q_{aero}}{\partial V}\Big|_0 \Delta V$ represents an external driving force and is omitted in the following as it doesn't influence the internal dynamics of the system. Finally $\Delta\theta$ is expressed by use of the proportional and integral gains:

$$\Delta\theta = k_P\,(\omega - \omega_{rated}) + k_I \int_0^t (\omega - \omega_{rated})\,dt \tag{A.19}$$

$$\Delta\theta = k_P\,\dot{\phi} + k_I\,\phi \tag{A.20}$$

Inserting Eq. A.20 into Eq. A.18 and rearranging yields an ordinary second order differential equation as the equation of motion of the closed-loop controller system:

$$I_{rotor}\,\ddot{\phi} + \Big(\frac{1}{\eta}\,\frac{\partial Q_{gen}}{\partial \omega}\Big|_0 - \frac{\partial Q_{aero}}{\partial \omega}\Big|_0 - \frac{\partial Q_{aero}}{\partial \theta}\Big|_0 k_P\Big)\,\dot{\phi} - \frac{\partial Q_{aero}}{\partial \theta}\Big|_0 k_I\,\phi = 0 \tag{A.21}$$

APPENDIX B

Loads on Offshore Wind Turbines

B.1 Aerodynamic loading

Unsteady BEM model

Wind is a stochastic phenomenon varying in time and space, therefore becoming important to know the position of any section along a blade with respect to a fixed coordinate system in order to realistically compute the aeroelastic behaviour of the wind turbine. In this project, a simple model, where the system is described by six coordinate systems as shown in Figure 2.7, is used.

First, an inertial system (coordinate system 1) is placed at the bottom of the wave basin. System 2 is placed at the floater platform and subjected to rotations and translations mainly excited by the hydrodynamic forces acting on the floater. Likewise, system 3, located at the transition piece between the tower bottom and the floater top, is moving along with the floater. A coordinate system can be expressed in another coordinate system by means of a transformation matrix, therefore a transformation matrix accounting for the platform rotations, i.e. rotations about the x-axis (roll, ξ_4), the y-axis (pitch, ξ_5) and the z-axis (yaw, ξ_6), can be built as:

$$
\begin{aligned}
\mathrm{a_{1x}} &= \begin{bmatrix} 1 & 0 & 0 \\ 0 & \cos(\xi_4) & \sin(\xi_4) \\ 0 & -\sin(\xi_4) & \cos(\xi_4) \end{bmatrix} \\
\mathrm{a_{1y}} &= \begin{bmatrix} \cos(\xi_5) & 0 & -\sin(\xi_5) \\ 0 & 1 & 0 \\ \sin(\xi_5) & 0 & \cos(\xi_5) \end{bmatrix} \\
\mathrm{a_{1z}} &= \begin{bmatrix} \cos(\xi_6) & \sin(\xi_6) & 0 \\ -\sin(\xi_6) & \cos(\xi_6) & 0 \\ 0 & 0 & 1 \end{bmatrix}
\end{aligned}
\tag{B.1}
$$

The total transformation matrix between system 1 and system 2 is found as $a_{12} =$

$a_{1x} \times a_{1y} \times a_{1z}$. If the floater is assumed to be stiff, system 3 experiments the same motions as system 2, and hence:

$$\mathrm{a}_{13} = \mathrm{a}_{12}\mathrm{a}_{23} = \mathrm{a}_{1\mathrm{x}}\mathrm{a}_{1\mathrm{y}}\mathrm{a}_{1\mathrm{z}} \begin{bmatrix} 0 & 0 & 1 \\ 0 & 1 & 0 \\ 1 & 0 & 0 \end{bmatrix} \tag{B.2}$$

System 4, non-rotating and placed in the nacelle, is rotated about the x-axis with the angle θ_{yaw} as well as rotated along the y-axis with the angle θ_{tilt}. System 4 is not rotated about the z-axis, and hence the transformation matrix between system 3 and system 4 is found as $a_{34} = a_{3x} \times a_{3y} \times a_{3z}$.

$$\begin{aligned} \mathrm{a}_{3\mathrm{x}} &= \begin{bmatrix} 1 & 0 & 0 \\ 0 & \cos(\theta_{yaw}) & \sin(\theta_{yaw}) \\ 0 & -\sin(\theta_{yaw}) & \cos(\theta_{yaw}) \end{bmatrix} \\ \mathrm{a}_{3\mathrm{y}} &= \begin{bmatrix} \cos(\theta_{tilt}) & 0 & -\sin(\theta_{tilt}) \\ 0 & 1 & 0 \\ \sin(\theta_{tilt}) & 0 & \cos(\theta_{tilt}) \end{bmatrix} \\ \mathrm{a}_{3\mathrm{z}} &= \begin{bmatrix} 1 & 0 & 0 \\ 0 & 1 & 0 \\ 0 & 0 & 1 \end{bmatrix} \end{aligned} \tag{B.3}$$

System 5, located on the main shaft, only experiences a rotation Ω about the z-axis throughout time if the shaft is assumed stiff, the only transformation between system 4 and system 5 is:

$$a_{45} = \begin{bmatrix} \cos(\Omega t) & \sin(\Omega t) & 0 \\ -\sin(\Omega t) & \cos(\Omega t) & 0 \\ 0 & 0 & 1 \end{bmatrix} \tag{B.4}$$

System 6, located at the root blade, is only rotated about the y-axis with the angle θ_{cone}, the only transformation between system 5 and system 6 is:

$$a_{56} = \begin{bmatrix} \cos(\theta_{\mathrm{cone}}) & 0 & -\sin(\theta_{\mathrm{cone}}) \\ 0 & 1 & 0 \\ \sin(\theta_{\mathrm{cone}}) & 0 & \cos(\theta_{\mathrm{cone}}) \end{bmatrix} \tag{B.5}$$

Finally a point P on the blade can be expressed in the inertial coordinate system (system 1), since the wind velocity is given with respect to this coordinate system:

$$\vec{r}_{P_1} = \begin{bmatrix} 0 \\ 0 \\ L_0 \end{bmatrix} + \mathbf{a}_{13}^T \begin{bmatrix} \xi_1 \\ \xi_2 \\ \xi_3 + h_f \end{bmatrix} + \mathbf{a}_{14}^T \begin{bmatrix} h_{\mathrm{t}} \\ 0 \\ 0 \end{bmatrix} + \mathbf{a}_{15}^T \begin{bmatrix} 0 \\ 0 \\ l_{\mathrm{s}} \end{bmatrix} + \mathrm{a}_{16}^T \begin{bmatrix} r \\ 0 \\ 0 \end{bmatrix} \tag{B.6}$$

Where L_0 is the length from the floater origin to the bottom of the wave basin, ξ_1, ξ_2, ξ_3 stand for the floater translational motions, i.e. surge, sway and heave, respectively, h_f is the floater height, h_t is the tower height, l_s is the length of the shaft and r is a radial position along the blade of study from the blade root.

The undisturbed wind velocity seen by the blade is computed by transforming the given wind speed with respect to the fixed coordinate system $\vec{V}_1$ to system 6:

$$\vec{V}_o = \begin{pmatrix} V_x \\ V_y \\ V_z \end{pmatrix} = a_{56} \cdot a_{45} \cdot a_{34} \cdot a_{13} \cdot \vec{V}_1 = a_{16} \cdot \vec{V}_1 \tag{B.7}$$

To find the relative velocity seen by the blade, $\vec{V}_{rel}$, the rotational velocity, $\vec{V}_{rot}$, the induced velocity, $\vec{W}$, the vibrational velocity of the blade, $\vec{V}_b$, plus the velocity of the floater, $\vec{V}_{float}$, must be added as vectors to $\vec{V}_0$ in system 6 as

$$\vec{V}_{rel} = \vec{V}_0 + \vec{V}_{rot} + \vec{W} - \vec{V}_b + \vec{V}_{float} \Longrightarrow$$
$$\begin{bmatrix} V_{rel,x} \\ V_{rel,y} \\ V_{rel,z} \end{bmatrix} = \begin{bmatrix} V_{0,x} \\ V_{0,y} \\ V_{0,z} \end{bmatrix} + \begin{bmatrix} 0 \\ -\Omega r \cos(\theta_{cone}) \\ 0 \end{bmatrix} + \begin{bmatrix} W_x \\ W_y \\ W_z \end{bmatrix} - \begin{bmatrix} 0 \\ V_{b,y} \\ V_{b,z} \end{bmatrix} + \begin{bmatrix} V_{\text{float},x} \\ V_{\text{float},y} \\ V_{\text{float},z} \end{bmatrix} \tag{B.8}$$

Note that the velocity of the floater, $\vec{V}_{float}$, is caused by the translational $(\dot{\xi}_1, \dot{\xi}_2, \dot{\xi}_3)$ and rotational $(\dot{\xi}_4, \dot{\xi}_5, \dot{\xi}_6)$ velocity components of the floater. It is also worth noticing that the tower velocity could have been included in the model.

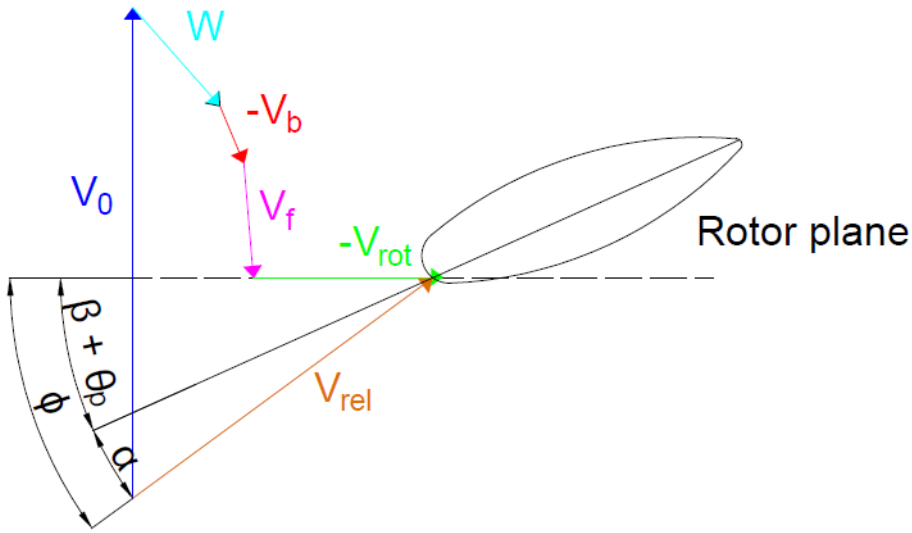

Figure B.1: Velocity triangle seen locally on a blade.

If the induced velocity, $\vec{W}$, the vibrational velocity of the blade, $\vec{V_b}$, and the velocity of the floater, $\vec{V_f}$, are known, the angle of attack α can be computed as:

$$\alpha = \phi - (\beta + \theta_p) = \phi - \theta \tag{B.9}$$

where the flow angle ϕ is:

$$\tan\phi = \frac{V_{\text{rel},z}}{-V_{\text{rel},y}} \tag{B.10}$$

θ is the local pitch of the blade, i.e. the local angle between the chord and the rotor plane. The local pitch is a combination of the pitch angle, θ_p, and the twist of the blade, β, where the pitch angle is the angle between the tip chord and the rotor plane and the twist is measured relative to the tip chord. The flow angle, ϕ, is the angle between the rotor plane and the relative velocity.

Once the angle of attack, α, is known at a specific radial position of the blade, the static lift coefficient ($C_l(\alpha)$) and drag coefficient ($C_d(\alpha)$) can be looked up and interpolated in the correspondent geometry airfoil for the purpose of calculating the lift and drag force per unit length in that particular radial position:

$$l = \frac{1}{2}\rho_{\text{air}} \left|V_{\text{rel}}\right|^2 cC_l(\alpha) \quad d = \frac{1}{2}\rho_{\text{air}} \left|V_{\text{rel}}\right|^2 cC_d(\alpha) \tag{B.11}$$

Where ρ_{air} stands for the air density (1.225 kg/m^3) and c is the chord length at the chosen radial position.

The lift and drag force are projected to compute the normal (p_n) and tangential (p_t) loads to the rotor plane as:

$$p_n = l\cos(\phi) + d\sin(\phi) \quad p_t = l\sin(\phi) - d\cos(\phi) \tag{B.12}$$

By integrating the different loads over the different blades, the aerodynamic thrust, T, and aerodynamic torque, M, can be easily computed as:

$$T = B\int_0^R p_n dr \quad M = B\int_0^R r p_t dr \tag{B.13}$$

The essence of the unsteady BEM algorithm is calculating the induced wake $\vec{W}$ for every time step, and thus the angles of attack. Under some assumptions and based on simple momentum theory the following quasi-static equations of the normal and tangential components can be derived:

$$W_{z,qs} = \frac{-Bl\cos(\phi)}{4\pi\rho_{air} rF\left|\vec{V_0} + f_g\vec{n}(\vec{n}\cdot\vec{W})\right|} \quad W_{y,qs} = \frac{-Bl\sin(\phi)}{4\pi\rho_{air} rF\left|\vec{V_0} + f_g\vec{n}(\vec{n}\cdot\vec{W})\right|} \tag{B.14}$$

Where B corresponds to the number of blades of the wind turbine, $\vec{n}$ is a unitary vector perpendicular to the rotor plane and F is the Prandtl's tip loss factor, which

is a correction factor accounting for the assumption of a rotor with infinite number of blades:

$$F = \frac{2}{\pi} cos^{-1}(e^{-f}), \quad \text{With} \quad f = \frac{B(R-r)}{2r\sin(\phi)} \tag{B.15}$$

Besides f_g is the known Glauert correction factor. For increasing axial induction factors a, the simple momentum theory is not valid anymore, and hence f_g is used to describe an empirical relation between the thrust coefficient C_T and the axial induction factor for those axial induction factors that are above the simple momentum theory region. Despite of the existence of several experimental relationships, in this project the following one is used:

$$f_g = \begin{cases} 1 & \text{for a} \leq \text{a}_\text{c} \\ \frac{a_c}{a}(2 - \frac{a_c}{a}) & \text{for a} > \text{a}_\text{c} \end{cases} \tag{B.16}$$

Note that a_c is normally close to 0.2 and the induction factor is calculated based on the deviation of the projected velocity $\vec{V'}$ from the inflow wind $\vec{V_0}$:

$$a = \frac{|\vec{V_0}| - |\vec{V'}|}{|\vec{V_0}|} \tag{B.17}$$

Where the magnitude of the projected velocity $|\vec{V'}|$ is equal to $|\vec{V_0} + \vec{W_y}|$. Further, notice that the equations must be solved iteratively since the flow angle and thus the angle of attack depend on the induced velocity itself.

Dynamic Wake model

In reality, the induced velocity does not adapt to a change in aerodynamic loads immediately, but takes a time delay to adapt to the new conditions. This can be modelled by means of a dynamic wake model that takes the time delay into account. There exist many engineering models to model this phenomenon by using an exponential decay function with appropriate time constants. In this project, the Øye model (1991) is used. A filter consisting of two first order differential equations is utilized as follows:

$$\vec{W}_{int} + \tau_1 \frac{d\vec{W}_{\text{int}}}{dt} = \vec{W}_{qs} + k\tau_1 \frac{d\vec{W}_{qs}}{dt} \tag{B.18}$$

$$\vec{W} + \tau_2 \frac{d\vec{W}}{dt} = \vec{W}_{int} \tag{B.19}$$

Where $\vec{W_{qs}}$ is the quasi-static induced wind (B.14), $\vec{W_{int}}$ an intermediate induced velocity value and $\vec{W}$ is the final filtered value of the induced wind velocity. Besides k=0.6 and the two time constant τ_1 and τ_2 are determined by:

$$\tau_1 = \frac{1.1}{(1-1.3a)}\frac{R}{\left|\vec{V_0}\right|} \quad \tau_2 = \tau_1\left(0.39 - 0.26\left(\frac{r}{R}\right)^2\right) \tag{B.20}$$

The two first order differential equations are solved by means of an iterative process that is thoroughly described in [68]. The dynamic filter is very important in order to correctly compute the time behaviour of the loads and power when the thrust is changed by, e.g. pitching the blades.

Dynamic stall

The wind seen locally on a blade experiences continuous changes due to wind shear, yaw/tilt misalignment, tower passage and atmospheric turbulence. As a result of this, the angle of attack changes dynamically while the blade is rotating. This dynamic change does not cause an instantaneous change in the aerodynamic loads but takes a delay time instead. This time dependent aerodynamic response will depend on whether the boundary layer is attached or partially separated. Thus, implementing a dynamic stall model is a good idea in order to avoid instabilities.

Stall is a phenomenon, which occurs when the inflow conditions or the angle of attack are rapidly changed, mainly affecting airfoils, wings, towers and rotors when the linear lift region has been exceeded. For trailing-edge stall the degree of stall is described through a separation function f_s, as:

$$C_l = f_s C_{l,inv}(\alpha) + (1 - f_s)C_{l,fs}(\alpha) \tag{B.21}$$

Where $C_{l,inv}$ denotes the lift coefficient for inviscid flow without any separation and $C_{l,fs}$ is the lift coefficient for fully separated flow. The separation function f_s can be described as:

$$f_s(t + \Delta t) = f_s^{st} + (f_s(t) - f_s^{st})\exp(\frac{-\Delta t}{\tau}) \tag{B.22}$$

Where f_s^{st} denotes the value of f_s that reproduces the static airfoil data when applied in B.21 and τ is a time constant approximately equal to Ac/V_{rel}, where c denotes the local chord, and V_{rel} is the relative velocity seen by the blade section. A is a constant that typically takes a value about 4. The dynamic stall model replaces the old static lift coefficient table look-up method with an improved dynamic lift coefficient estimation which allows for a time delay.

Wind shear model

As aforementioned, the wind velocity field seen by a wind turbine varies both spatially and temporally and the boundary layer caused by thermal changes in height, obstacles such as buildings or hills must be included when modelling a wind field as the one shown in Figure B.2.

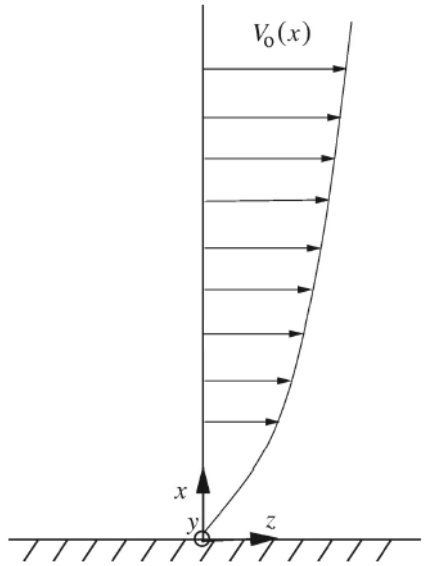

Figure B.2: Example of a wind velocity shear model without turbulence. Figure taken from [68].

The effect of wind shear is an increase of mean wind velocity along the height above the ground following a power law that can be modelled as:

$$V_o(x) = V_o(H)(\frac{x}{H})^v \tag{B.23}$$

Where H is the hub height, x the distance from the surface and v a parameter quantifying the shear, normally between 0.1 and 0.25.

Tower model

The wind is also affected by the presence of the tower. This interaction may be modelled by means of potential flow theory. A polar coordinate system can be introduced to calculate the radial and tangential components of the wind speed around the tower as seen in Figure B.3.

$$V_r = V_0 \left(1 - \left(\frac{a}{r}\right)^2\right) \cos(\theta) \quad V_\theta = -V_0 \left(1 + \left(\frac{a}{r}\right)^2\right) \sin(\theta) \tag{B.24}$$

Where V_0 is the free stream wind velocity, a is the tower radius, r is the radial distance from the center of the tower and θ is the azimuthal position of the radial vector with respect to the horizontal axis. The inclusion of the tower model causes a drop in the

relative velocity felt by a blade every revolution, and hence causing a thrust reduction with a 3P frequency.

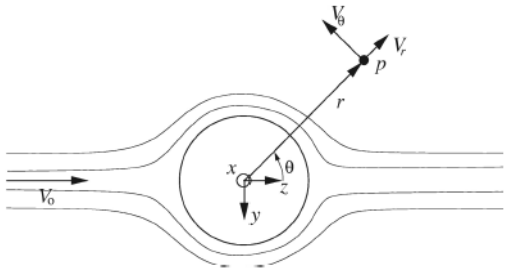

Figure B.3: Tower shadow effect. Figure taken from [68].

Turbulence

The incoming wind flow to a wind turbine rotor is turbulent and varying both in time and space. A realistic wind field must thus be modelled as input to the BEM code. Not only the flow is unsteady but three-dimensional. The instantaneous wind speed in any direction is the result of the sum of its mean value and an alternating component composed of both low and high frequency turbulent flows. This fluctuating component can be obtained from different turbulent models aiming at reproducing this stochastic nature.

Turbulence intensity, TI, is a way of describing how turbulent a wind time-series is. By knowing the standard deviation of the signal σ and the 10-minute average wind speed V_{10min}, the TI is defined as:

$$TI = \frac{\sigma}{V_{10min}} \tag{B.25}$$

The higher the turbulence intensity, the higher the alternating component of the wind will become, and hence the more varying the aerodynamic loads on the blades of the rotor will become. It is thus essential to model a reliable wind turbulence model in order to carry out a good fatigue lifetime design. Other extreme events such as gusts should also be modelled in order to correctly determine the ultimate loads on a wind turbine.

Wind time-series can be built from a known Power Spectral Density (PSD) by means of an inverse discrete Fourier transform (DFT). Several spectrums such as the Kaimal or the Von Karman spectrum are used to model the atmospheric boundary layer. In this project, the Von Karman spectrum has been used:

$$E(k) = \alpha\epsilon^{2/3}L^{5/3}\frac{(Lk)^4}{(1+(Lk)^2)^{17/6}} \tag{B.26}$$

Where $\alpha\epsilon^{2/3}$ is a dimensionless constant often set to 1.7, L is the turbulence length scale and k is the wave number.

Once the spectrum has been computed, the wind time-series is built by means of the inverse DFT,derived in [68], as shown below:

$$V(t) = \bar{V} + \sum_{n=1}^{N/2} \sqrt{\frac{2E(k)}{T}} \cos\left(\omega_n t - \phi_n\right) \tag{B.27}$$

Where $\bar{V}$ is the mean wind speed, T is the total time of the time-series and ϕ_n is the phase angle for a given frequency ω_n.

Even though turbulence is three-dimensional, the wind field should present some spatial and temporal correlation, i.e. the closer two points, the more correlated they should be in time and space.The high frequency content of the time-series is a result of small vortices, which have small spatial influence. Similarly the low frequency part is related to large-scale vortices covering a bigger volume of the flow. A coherence function needs to take into account both the distance, L, between points j and k and the frequency f:

$$coh_{jk} = \exp(-12(fL/V_{10min}) \tag{B.28}$$

Veers (1988) developed a method to generate a 3D wind field. The method builds a symmetric N_pxN_p matrix S of spectras:

$$S_{jk} = \mathrm{coh}_{jk}\sqrt{S_{jj}S_{kk}} \tag{B.29}$$

Where the diagonal terms (S_{jj} and S_{kk}) are the PSD functions of the points, and the off-diagonal terms are the cross-spectras S_{jk}. Once the S-matrix is obtained, a lower triangular H matrix is recursively computed:

$$\mathbf{H} = \begin{bmatrix} H_{11} = \sqrt{S_{11}} & 0 & \cdots & 0 \\ H_{21} = S_{21}/H_{11} & H_{22} = \sqrt{S_{22} - H_{21}^2} & \ddots & 0 \\ \vdots & \ddots & \ddots & \vdots \\ & H_{jk} = \left(S_{jk} - \sum_{i=1}^{k-1} H_{ji}H_{ki}\right)/H_{kk} & \cdots & H_{kh} = \sqrt{S_{kk} - \sum_{i=1}^{k-1} H_{ki}^2} \end{bmatrix} \tag{B.30}$$

For each point k and for each frequency f_m, a random number , ϕ_{km} between 0 and 2π is computed. Then the complex velocity vector of the number of points in space can be calculated as:

$$V_j\left(f_m\right) = \sum_{k=1}^{j} H_{jk}\cos\left(\phi_{kn}\right) + i\sum_{k=1}^{j} H_{jk}\sin\left(\phi_{km}\right) \tag{B.31}$$

The complex velocity vector is expressed as a polar form:

$$\left|V_j\left(f_m\right)\right| = \sqrt{\mathrm{Re}\left(V_j\left(f_m\right)\right)^2 + \mathrm{Im}\left(V_j\left(f_m\right)\right)^2} \quad \Phi_j\left(f_m\right) = \tan^{-1}\left(\frac{\mathrm{Im}(V_j(f_m))}{\mathrm{Re}(V_j(f_m))}\right) \tag{B.32}$$

Lastly the wind time-series can be computed at the points j= 1,...,N_p as:

$$V_j(t) = V + \sum_{m=1}^{N/2} 2\,|V_j\,(f_m)|\cos\left(2\pi f_m t - \Phi_j\,(f_m)\right) \quad \text{with } t = i\Delta t \text{ for } i = 1,\ldots,N \tag{B.33}$$

Using Eq. B.33 together with appropriate PSD and coherence functions, the wind time-series are computed for every velocity component $\vec{V}$(u,v,w) independently. For aeroelastic calculations of wind turbines, it is normal to use a number of points N_p as shown in Figure B.4. The velocities on the blade sweeping through the grid must, in general, be found by spatial interpolation. It should be mentioned that the time history of the wind seen by a point on the blade is different from the time history of a point fixed in space. A time history for a point on the rotating blade is called rotational sampling and in Veers (1988) is shown how this can directly be calculated for a blade with a constant rotational speed.

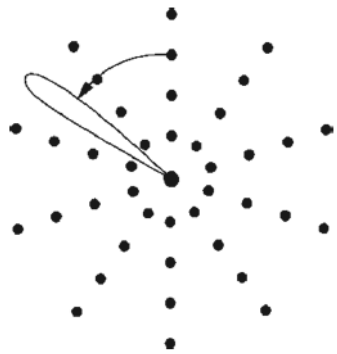

Figure B.4: Grid points distribution. Figure taken from [68].

This section has been based on the references [68, 62, 69].

B.2 Hydrodynamic loading

B.2.1 Wave Kinematics

The Stokes 1^{st}-order wave theory or so-called Airy wave theory gives a linearized description of the propagation of gravity waves on the surface of a homogeneous fluid layer built on potential flow theory, and hence the flow is incompressible, inviscid and irrotational. Furthermore, both the depth and the wave period are assumed to be constant. In regular wave theory, the wave is assumed to be sinusoidal with constant wave amplitude, wavelength, and wave period. Irrotational and incompressible flows can be described by a velocity potential ϕ. Every velocity component is described as a gradient of the velocity potential itself as:

$$\underline{V} = (u, w) = \left(\frac{\partial \phi}{\partial x}, \frac{\partial \phi}{\partial z} \right) \tag{B.34}$$

Where u and w describe the horizontal and vertical particle velocity respectively. The mass conservation for an incompressible flow can be expressed as:

$$\frac{\partial \rho}{\partial t} + \operatorname{div}(\rho \underline{V}) = 0 \Longleftrightarrow \operatorname{div} \underline{V} = 0 \Longleftrightarrow \frac{\partial u}{\partial x} + \frac{\partial w}{\partial z} = 0 \tag{B.35}$$

Both equations combined yield the Laplace equation, which must be satisfied in the entire water body:

$$\nabla^2 \phi = \phi_{xx} + \phi_{zz} = 0 \quad , \quad -h < z < \eta \tag{B.36}$$

Hereby the indices xx and zz refer to the second partial derivative with respect to x and z. The following boundary conditions must be satisfied:

1. *Bottom boundary condition.* It assumes that the flow can not go through the sea bottom, consequently the vertical particle velocity, w, is null at the sea bottom (B.37).
2. *Kinematic Free Surface Boundary Condition.* A particle that is at the surface will remain at the surface (B.38).
3. *Dynamic Free Surface Boundary Condition.* Balance between gravitational potential and the velocity derived from Bernoulli Eq. B.39.

$$\phi_z = w = 0 \quad , \quad z = -h \tag{B.37}$$

$$\eta_t + u\eta_x - w = 0 \quad , \quad z = \eta \tag{B.38}$$

$$\phi_t + g\eta + \frac{1}{2}\left(u^2 + w^2\right) = 0 \quad , \quad z = \eta \tag{B.39}$$

Assuming a given velocity potential on finite depth (B.40), it can be shown that this velocity potential is a solution to the Laplace equation and the bottom boundary condition, where B is a constant. On the other hand, by application of both the dynamic and kinematic free surface condition, the dispersion relation (B.41), which correlates the space and time domain of a wave, is obtained. Then, by connecting the free surface condition to the velocities, the constant B can be obtained (B.42). Finally, if the velocity potential is differentiated with respect to the spatial coordinates, the particle velocities and accelerations are obtained.

$$\phi = B \cosh k(z+h) \sin(\omega t - kx) \tag{B.40}$$

$$\omega^2 = gk \tanh(kh) \tag{B.41}$$

$$B = -\frac{\omega H}{2k} \frac{1}{\sinh kh} \tag{B.42}$$

A summary of the expressions for velocity potential, surface elevation and particle velocity for the linear regular wave theory is shown in Table B.1.

Table B.1: Free surface elevation, velocity potential, wave kinematics and dispersion relation for both regular and irregular waves.Note that ϵ_j stands for a random phase angle uniformly distributed on $[0; 2\pi]$.

Linear Wave Theory	
Regular Waves	**Irregular waves**
$\eta = \frac{H}{2} \cos(\omega t - kx)$	$\eta = \sum_{j=1}^{N} A_j \cos(\omega_j t - k_j x + \epsilon_j)$
$\phi = -\frac{\omega H}{2k} \frac{\cosh k(z+h)}{\sinh kh} \sin(\omega t - kx)$	$\phi = \sum_{j=1}^{N} -A_j \frac{\omega_j}{k_j} \frac{\cosh k_j(z+h)}{\sinh k_j h} \sin(\omega_j t - k_j x + \epsilon_j)$
$u = \frac{\omega H}{2} \frac{\cosh k(z+h)}{\sinh kh} \cos(\omega t - kx)$	$u = \sum_{j=1}^{N} A_j \omega_j \frac{\cosh k_j(z+h)}{\sinh k_j h} \cos(\omega_j t - k_j x + \epsilon_j)$
$w = -\frac{\omega H}{2} \frac{\sinh k(z+h)}{\sinh kh} \sin(\omega t - kx)$	$w = \sum_{j=1}^{N} -A_j \omega_j \frac{\sinh k_j(z+h)}{\sinh k_j h} \sin(\omega_j t - k_j x + \epsilon_j)$
$\omega^2 = gk \tanh(kh)$	$\omega_j^2 = gk_j \tanh k_j h$

B.2.2 Morison Equation

The Morison equation can be used to calculate the hydrodynamic forces on a slender submerged body like a monopile. Assuming a submerged body moving in water with the velocity U_b, the hydrodynamic force per unit height on the body is expressed as followed [70]:

$$F = \underbrace{\frac{1}{2} \rho C_D |U - U_b| (U - U_b)}_{\text{Drag force}} + \underbrace{\underbrace{\rho C_m A \frac{d}{dt}(U - U_b)}_{\text{Hydrodynamic mass force}} + \underbrace{\rho A \frac{dU}{dt}}_{\text{Froude-Krylov force}}}_{\text{Inertia force}} \tag{B.43}$$

hereby ρ denotes the water density, U the water particle velocity, C_D the drag coefficient, A the cross-sectional area of the body and C_m the inertia coefficient. The first term in the Morison equation describes the drag forces exerted on the body, which depends on the relative velocity between the body and the water. The second term describes the hydrodynamic mass force, which can be seen as the force necessary to decelerate the moving liquid around the body or accelerate the water moving with

the body. The last term describes the Froude-Krylov force, which is the force due to the pressure gradient of the outer flow [70]. The inertia and drag coefficients C_m and C_D depend on the shape of the structure, the influence of marine growth and some other factors that can be looked up for specific cases [71]. The hydrodynamic mass force together with the Froude-Krylov force represent the inertia forces, which depend on the acceleration of the water and the body. The term due to the body acceleration is often added to the system mass matrix as an added mass. In this case the Morison equation can be expressed in a more compact form [70]:

$$F = \underbrace{\frac{1}{2}\,\rho\, C_D\, |U - U_b|\, (U - U_b)}_{\text{Drag force}} + \underbrace{\rho\, C_M\, A\, \frac{dU}{dt}}_{\text{Inertia force}} \tag{B.44}$$

with

$$C_M = C_m + 1 \tag{B.45}$$

The ratio between drag and inertia forces can be expressed with the Keulegan-Carpenter number (KC) [70]:

$$KC = \frac{U_m\, T_w}{D} \tag{B.46}$$

with D being the diameter of the cross-section, U_m the maximum horizontal velocity of the water particles and T_w the wave period. For small KC (KC < 20) the loads are inertia dominated and for large KC (KC > 20) the loads are drag dominated [70].

The Morison equation is an empirical formula based on several assumptions: It is assumed that the flow at the center of the body is representative for the flow around the body and that the diffracted wave field due to the body is negligible. These assumptions are only valid for slender bodies. When $D/L > 0.2$, with L being the wave length, the scattered wave field due to diffraction becomes important [70]. The MacCamy-Fuchs diffraction correction accounts for this by adjusting the inertia coefficient C_M depending on the ratio D/L [71]. Alternatively a more advanced method for calculating the wave loads, like linear radiation-diffraction theory, must be applied to obtain the wave loads on more complex structures.

B.2.3 Linear Radiation-Diffraction Theory

Linear radiation-diffraction theory divides the wave load calculation into two separate problems: a radiation and a diffraction problem. The radiation part refers to a body oscillating with a certain frequency ω in otherwise still water, hereby radiating waves. The diffraction part describes a fixed body being exposed to incoming waves with frequency ω. The total solution is then the sum of both individual parts. Diffraction-radiation theory is formulated in the frequency domain [72].

For the radiation part, a freely floating body with 6 DoFs is considered: 3 translational DoFs (surge, sway, heave) and 3 rotational DoFs (roll, pitch, yaw). Each DoF

is assumed to oscillate with a certain frequency ω. Mathematically the body motion can be described by the real part of a complex harmonic function [72]:

$$\vec{\Xi}(t) = Re(\vec{\xi} e^{i\omega t}) \tag{B.47}$$

Where $\vec{\xi} = [\xi_1, ..., \xi_6]^T$ is the vector with the amplitudes of all 6 DoFs and i the imaginary unit. Furthermore, a potential flow is assumed, which implies an irrotational, inviscid and incompressible fluid [56]. Therefore, viscous loads are not included into radiation-diffraction theory and have to be added in another way, e.g. through the drag term in the Morison equation. In potential flow theory, a velocity potential field is defined, whose gradient at a certain point is the velocity at that point:

$$\nabla\Phi(x, y, z, t) = \vec{u}(x, y, z, t) \tag{B.48}$$

where x, y, z are the coordinates in space and t the time. For the formulation of radiation-diffraction theory a harmonic velocity potential field is assumed:

$$\Phi(x, y, z, t) = Re(\phi\, e^{i\omega t}) \tag{B.49}$$

where ω is the frequency of the incident wave field, assuming a linear regular incoming wave. By leaving out the harmonic term $e^{i\,\omega\,t}$, the expression is transferred to the frequency domain. The total velocity potential is now expressed in terms of the individual contributions due to diffraction and radiation [72]:

$$\phi = \underbrace{\phi_0 + \phi_7}_{\text{Diffraction}} + \underbrace{\sum_{j=1}^{6} \xi_j\, \phi_j}_{\text{Radiation}} = \phi_D + \phi_R \tag{B.50}$$

Where ϕ_0 represents the potential due to incident waves of unit amplitude and ϕ_7 the potential due to the scattered wave field around the body caused by diffraction. In terms of radiation, ϕ_j describes the potential due to unit body motion in DoF j and the sum of all 6 DoF is the total potential due to radiation. In the entire domain the Laplace equation needs to be satisfied:

$$\nabla^2\,\phi = \frac{\partial^2\,\phi}{\partial\,x^2} + \frac{\partial^2\,\phi}{\partial\,y^2} + \frac{\partial^2\,\phi}{\partial\,z^2} = 0 \tag{B.51}$$

Furthermore the linearized surface and bottom boundary conditions must be satisfied [27]:

$$\frac{\partial\,\phi}{\partial z} - \frac{\omega^2}{g}\,\phi = 0 \quad , \quad \text{at } z = 0 \tag{B.52}$$

$$\frac{\partial\,\phi}{\partial z} = 0 \quad , \quad \text{at } z = \text{-}h \tag{B.53}$$

where g is the gravitational acceleration and h the water depth. The potential due to wave scattering and radiation is caused by the presence of the body, therefore these potentials must approach zero for large distances away from the body. This is stated by the infinity condition [27]:

$$\phi_j \to \frac{e^{-ikR}}{\sqrt{R}} \quad \text{as} \quad R \to \infty \quad \text{for} \quad j = 1...7 \tag{B.54}$$

where $R = \sqrt{x^2 + y^2}$ is the horizontal distance from the coordinate system origin and k the wave number of the incoming wave field. Finally the boundary conditions on the body surface must be defined. The diffraction potential must satisfy a boundary condition, which results in zero velocity in normal direction on the surface of the body [27]:

$$\frac{\partial \phi_D}{\partial n} = 0 \tag{B.55}$$

$$\frac{\partial \phi_0}{\partial n} = -\frac{\partial \phi_7}{\partial n} \tag{B.56}$$

where $\vec{n}$ is a vector normal to the body surface pointing into the body. The radiation potentials must be formulated, such that the water velocity on the body surface is equal to the body's velocity in normal direction [27]:

$$\frac{\partial \phi_j}{\partial n} = i\,\omega\,\vec{n}_j \quad \text{for} \quad j = 1, 2, 3 \tag{B.57}$$

$$\frac{\partial \phi_j}{\partial n} = i\,\omega\,\left(\vec{r} \times \vec{n}\right)_{j-3} \quad \text{for} \quad j = 4, 5, 6 \tag{B.58}$$

where $\vec{r}$ is the position vector $\vec{r} = (x, y, z)$. According to the linearized Bernoulli equation the water pressure can be expressed as followed [72]:

$$p = -\rho \left(gz + \frac{\partial \phi}{\partial t}\right) \tag{B.59}$$

The forces and moments on the floating body are obtained by integrating the pressure over the surface of the body:

$$\vec{F} = \int_{S_B} p \begin{pmatrix} \vec{n} \\ \vec{r} \times \vec{n} \end{pmatrix} dS \tag{B.60}$$

$\vec{F}$ is a vector containing the forces in x-, y- and z-direction as the first three elements and the corresponding moments as the last three elements. By applying Eq. B.59 for the pressure and Eq. B.50 for the velocity potential in Eq. B.60, the forces are expressed as followed:

$$\vec{F} = -\rho \int_{S_B} \left(gz + \frac{\partial \phi}{\partial t}\right) \begin{pmatrix} \vec{n} \\ \vec{r} \times \vec{n} \end{pmatrix} dS \tag{B.61}$$

$$\vec{F} = -\rho \int_{S_B} \left(g z + i\,\omega(\phi_0 + \phi_7) + i\,\omega \sum_{j=1}^{6} \xi_j\,\phi_j \right) \begin{pmatrix} \vec{n} \\ \vec{r} \times \vec{n} \end{pmatrix} dS \tag{B.62}$$

The force equation consists of individual components proportional to displacement, velocity and acceleration of the body, as well as an excitation term depending on the incident wave [27]:

$$\begin{aligned} \vec{F} = &- \rho \int_{S_B} g z \begin{pmatrix} \vec{n} \\ \vec{r} \times \vec{n} \end{pmatrix} dS - \rho \int_{S_B} i\,\omega(\phi_0 - \phi_7) \begin{pmatrix} \vec{n} \\ \vec{r} \times \vec{n} \end{pmatrix} dS \\ &- \rho \int_{S_B} i\,\omega \sum_{j=1}^{6} \xi_j\,\phi_j \begin{pmatrix} \vec{n} \\ \vec{r} \times \vec{n} \end{pmatrix} dS \end{aligned} \tag{B.63}$$

The first integral expresses forces proportional to the position or displacement of the floating body. The second integral describes excitation forces depending on the incident wave and scattered wave. The last term expresses forces proportional to the velocity and acceleration of the body. These individual force terms can be added to the matrices of the generic equation of motion of a floating body:

$$\vec{F} = -\mathbf{C}\,\vec{\xi} + \mathbf{X}(\omega) + \omega^2\,\mathbf{A}(\omega)\,\vec{\xi} - i\,\omega\,\mathbf{B}(\omega)\,\vec{\xi} = -\omega^2\,\mathbf{M}\,\vec{\xi} \tag{B.64}$$

Rearranging the terms yields the general form of the equation of motion of the floater in the frequency domain:

$$-\omega^2 \Big(\mathbf{M} + \mathbf{A}(\omega) \Big) + i\,\omega\,\mathbf{B}(\omega)\,\vec{\xi} + \mathbf{C}\,\vec{\xi} = \mathbf{X}(\omega) \tag{B.65}$$

Hereby $\mathbf{X}(\omega)$ represents the wave excitation forces for unit wave amplitude. The excitation forces for any free surface elevation $\eta(t)$ are given by $\mathbf{X}(\omega)\,\hat{\eta}(\omega)$, where $\hat{\eta}(\omega)$ is the FFT kernel of the surface elevation [72]. It is important to remember, that the wave forcing does not include viscous effects, because a potential flow was assumed. Viscous forces must therefore be included additionally by e.g. the drag term in the Morison equation. The elements of the mass matrix $\mathbf{M}$ and the restoring matrix $\mathbf{C}$ are independent of the frequency ω. The elements of the added mass matrix $\mathbf{A}$ and the damping matrix $\mathbf{B}$ however depend on ω.

In practise the radiation-diffraction problem is usually solved by a commercial software like WAMIT, in which the floating body is modelled and the force Eq. B.62 is solved for a set of discrete frequencies ω_n. The elements of $\mathbf{A}, \mathbf{B}$ and $\mathbf{X}$ are therefore obtained as a function of ω [72] and are added to the system matrices.

APPENDIX C

Measurement Campaign

C.1 Environmental Conditions

Table C.1: Regular sea states for 2021 TetraSub test campaign. Each regular sea state has two different wave heights. The naming will be as followed: EC X.1 for H_s = 0.033 and EC X.2 for H_s = 0.1.

	H [m]		**T [s]**		**Tdur [min]**	
	Full scale	Model scale	Full scale	Model scale	Full scale	Model scale
EC F	[2 , 6]	[0.033 , 0.1]	6	0.77	20	5
EC G	[2 , 6]	[0.033 , 0.1]	10	1.29	20	5
EC H	[2 , 6]	[0.033 , 0.1]	12	1.55	20	5
EC I	[2 , 6]	[0.033 , 0.1]	16	2.07	20	5
EC J	[2 , 6]	[0.033 , 0.1]	20	2.58	20	5

Table C.2: Regular sea states from 2017 TetraSpar and TLP test campaign.

	H [m]		**T [s]**		**Tdur [min]**	
	Full scale	Model scale	Full scale	Model scale	Full scale	Model scale
EC 3	0.426	0.055	6	0.77	20	3
EC 5	0.535	0.069	10	1.29	20	3
EC 6	0.798	0.103	12	1.55	20	3
EC 11	1.356	0.175	16	2.07	20	3

C.2 Power spectra wave-only

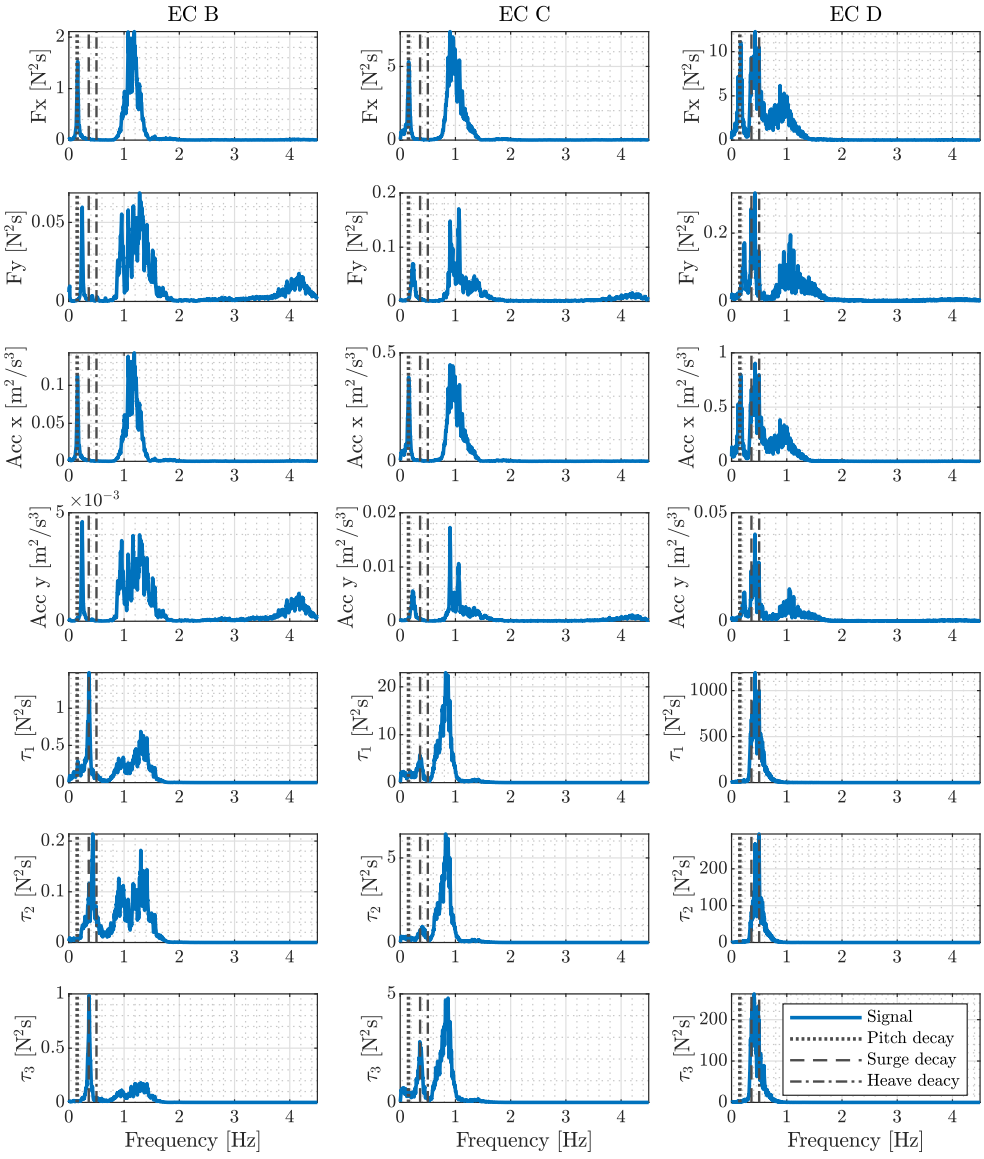

Figure C.1: Power spectra for mooring line tensions, tower-top shear forces and accelerations in fore-aft (x) and side-side (y) direction for wave-only cases.

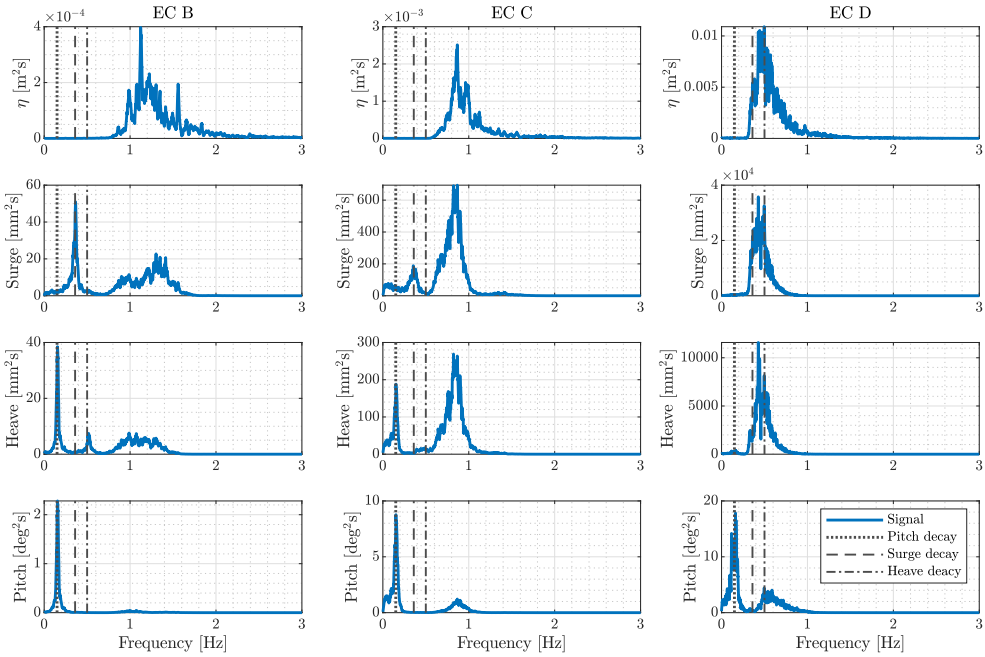

Figure C.2: Power spectra for surface elevation, surge, heave and pitch motion for wave-only cases.

APPENDIX D

Controller Tuning

D.1 Fixed parameters

The fixed parameters are the following ones (see Table D.1):

- **KK1** $[rad]$. Coefficient of linear term in aerodynamic gain scheduling (see Section 2.2.1.3).
- **K** $[Nm/(rad/s)^2]$. Optimal C_p tracking factor below rated wind speed (see Section 2.2.1.1).
- θ_{init} **[deg]**. Initial blade pitch angle (see Figure 2.11).
- θ_{min} **[deg]**. Minimum blade pitch angle.
- ω_{in} **[rad/s]**. Cut-in rotor speed.
- f_ω **[Hz]**. Cut-off frequency for rotor speed filtering.
- f_θ **[Hz]**. Cut-off frequency for blade pitch filtering.

Table D.1: Fixed parameters for the controller.

Parameter	**KK1**	**K**	θ_{ini}	ω_{in}	f_ω	f_θ
Units	**[rad]**	**[Nm/(rad/s)^2]**	**[Deg]**	**[rad/s]**	**[Hz]**	**[Hz]**
Value	0.13160	0.007142	4.53	2.5	1.25	3.5

D.2 Baseline controller tuning

Table D.2: Baseline controller tuning.

Controller	**CL frequency**	**Kp**	**Ki**
[-]	**[Hz]**	**[rad/(rad/s)]**	**[rad/rad]**
A_001	0.06	0.018	0.005
A_003	0.15	0.045	0.030
A_004	0.2	0.060	0.054
A_005	0.25	0.076	0.085
A_007	0.35	0.106	0.167

D.3 Improved baseline controller tuning

Table D.3: Improved baseline controller tuning.

Controller	**CL frequency**	**Kp**	**Ki**	$f_{K_{tt}}$	K_{tt}
[-]	**[Hz]**	**[rad/(rad/s)]**	**[rad/rad]**	**[Hz]**	**[rad/(m/s)]**
D_002	0.35	0.106	0.167	5	0.01
D_008	0.35	0.106	0.167	5	0.06
D_015	0.35	0.106	0.167	5	0.1625

{2.7182818284}ϑφερτυθιοπσδφγηξκλ